UNIVERSITY OF CRETE

STRUCTURE & EVOLUTION OF
MAGNETIC MOLECULAR CLOUDS:
OBSERVATIONAL CONSEQUENCES AND TESTS

Georgia Virginia PANOPOULOU

Submitted in partial fulfillment
of the requirements for the
degree of Doctor of Philosophy

February 28, 2017

Structure and evolution of magnetic molecular clouds:
Observational consequences and tests
Georgia Virginia Panopoulou
Department of Physics
University of Crete, 2017
Thesis supervised by Prof. Konstantinos Tassis

Abstract: Molecular clouds provide the initial stage for the star formation process. A complete understanding of the onset of this process relies on studying the numerous physical mechanisms that influence the structure and evolution of molecular clouds.

Detailed maps of cloud structure have recently been delivered by the Herschel Space Observatory, through observations of thermal dust emission. These measurements show that molecular cloud morphology is predominantly filamentary. The filamentary structures seem to have a 'characteristic' width of 0.1 pc. However, a robust theoretical explanation for this characteristic scale has proved elusive. We highlight discrepancies between this result and other observational evidence. Using an own-developed automated code for measuring filament properties, we revisit the analysis of filament widths on Herschel images. We find biases in the adopted methodology of previous works and show that the available data do not support the existence of a 'characteristic' width for the observed filaments.

Filament orientations appear to be closely related to that of the magnetic field within dense star-forming clouds. The observed connection suggests that the field is dynamically important in such systems. Similar evidence is lacking in the regime of translucent molecular clouds. We investigate the situation in this poorly studied regime, targeting the Polaris Flare molecular cloud. We map the magnetic field orientation in the cloud using the RoboPol optopolarimeter and deliver upgrades to the existing data processing pipeline (improving control of systematics throughout the instrument field of view). We find the field to be ordered across a large fraction of the cloud area, implying that it is strong compared to gas turbulent motions. We compare the orientation of the observed magnetic field to that of filaments in the Herschel map of the cloud and find strong preference for alignment. Our results indicate that the magnetic field has an important impact on the dynamics and therefore the structure and evolution of this cloud.

Acknowledgments

Contents

Chapter 1

Introduction

The formation of stars happens in the densest, coldest parts of molecular clouds, referred to as 'dense cores'. The conditions in such cores determine in some (yet unsettled) way the specific properties of stars, from their initial mass function (IMF) to their multiplicities. Tracing the origin of these properties relies on a careful examination of all the components influencing the structure and evolution of molecular clouds: atoms and molecules in the gas phase, solid dust particles, radiation, cosmic rays, as well as magnetic and gravitational fields.

Observations have established the typical properties of molecular clouds. The minimum visual extinction in dense molecular clouds is $5-10$ mag [Snow and McCall, 2006], thus a significant amount of external ionizing radiation is blocked from entering the bulk of the cloud. As a result, this environment allows for the existence of molecules, such as H_2 and CO (the most abundant trace element). There is a small amount (1% by mass) of dust grains which are heated by the interstellar radiation field (ISRF) and cosmic rays permeating the clouds and are cooled by thermal emission [Whittet, 2002]. The temperature of these grains in cores is around 10 K [for a recent survey see Juvela et al., 2012] and is comparable to that of the gas, which is loosely coupled to the dust by collisions. The collisional coupling of gas with dust grains becomes strong at hydrogen number densities $n_H > 10^4 - 10^5 \, \mathrm{cm}^{-3}$ after which we expect the temperature of the grains to equal that of the gas [Goldsmith, 2001]. In general, number densities range from $n_H \sim 100 \, \mathrm{cm}^{-3}$ in cloud envelopes to $n_H > 10^6 \, \mathrm{cm}^{-3}$ in the densest cores [Myers, 1999]. With sizes of $1-10$ pc, clouds contain $10^2 - 10^5 \, \mathrm{M}_\odot$ of matter [Blitz and Williams, 1999]. If thermal motions were the sole counterpart to the clouds' self-gravity, these clouds would rapidly collapse (free fall time $\sim 10^6$ yr) and convert all or most of their mass into stars. However, this is not observed: typically only $\sim 2-8\%$ of a cloud's mass is transformed into stars [Kennicutt and Evans, 2012]. Moreover, observational evidence shows that typical cloud lifetimes are much longer than the free-fall time [$\sim 10^7$ yr as opposed to $\sim 10^6$ yr, as reviewed by Heyer et al., 2016].

The solution to this apparent puzzle is provided by the effect of the magnetic field and/or turbulent motions. Measurements of the magnetic field strength in molecular clouds have found typical values of a few tens to a few hundreds of μG [Crutcher et al., 2010]. Since matter is partially ionized [with typical ionization fractions of $n_e/n_H \sim 10^{-4} - 10^{-7}$ Caselli et al., 1998, Goicoechea et al., 2009] from the ISRF and cosmic rays, the bulk of the gas is affected indirectly by the Lorentz force (acting on the ions) through collisions. Thus, the magnetic field offers support to the gas by exerting pressure and tension against the pull of gravity. Furthermore, the observed linewidths of molecules such as CO imply that motions inside molecular clouds are supersonic[Liszt et al., 1974], with the exception of the interiors of dense cores where motions approach thermalization [Goodman et al., 1998]. These motions are typically attributed to externally-driven turbulence, which can provide support against gravity [Elmegreen and Scalo, 2004][1].

The true picture, however, is far from the simplified overview given above. The multitude of components, along with their interactions, form a complex system (whose complexity increases after

---

[1]However, recent work indicates that the highly supersonic motions inferred may be a result of opacity broadening [Hacar et al., 2016a]

the formation of stars due to the resulting energetic feedback). Increasingly advanced observations are unveiling more about the true nature of these intricate systems and raising new and exciting questions. At the same time, numerical simulations are necessary to reproduce and explain these observed properties and predict yet unseen effects. In the following sections we introduce the most recent observational results on the structural characteristics of matter and magnetic field as well as both old and new relevant theoretical works. We concentrate on the results concerning clouds at scales between the size of an individual pre-stellar core and that of a single cloud $(0.1 - 10 \, \text{pc})$. Also, motivated by a search for the initial conditions of star formation, we choose to consider clouds (or parts within them) that are far from regions where significant stellar feedback has occurred.

1.1   The morphology of matter in molecular clouds

Our quest to understand the morphology of molecular clouds is subject to two main restrictions: (i) we can only observe structure as projected on the plane of the sky, and (ii) the primary component of molecular clouds, H_2, is invisible (there are no available transitions at the typical temperature of clouds). As a result, the structure of H_2 clouds is usually inferred from the column density of observed trace elements (e.g. thermal continuum dust emission, line emission from rotational transitions of molecules such as CO) in combination with line-of-sight kinematic information from the line emission of various molecules.

The clearest, most detailed view of thermal dust emission in clouds has been provided by the Herschel Space Observatory [Pilbratt et al., 2010, André et al., 2010]. Herschel dust emission maps cover all nearby star forming regions from scales of $\sim 10 \, \text{pc}$ down to (previously unresolved) $0.01 \, \text{pc}$. These observations show that cloud morphology is predominantly filamentary. The term 'filament' is attributed to elongated overdensity structures with aspect ratios (length-to-width ratios) of $\sim 5 - 10$. The existence of such structures in molecular clouds was known early on from stellar extinction maps [Barnard, 1907]. However it was the significant coverage and sufficient dynamical range of Herschel that enabled statistical samples of such structures to be studied. Such studies revealed that filaments show the following characteristics:

i. Filament column density profiles are well fit by Plummer functions of the form $\propto [1 + (r/R_{flat})^2]^{(1-p)/2}$, where R_{flat} is the extent of the flat inner part of the profile (in logarithmic units) and $1.5 < p < 2$ [e.g. Arzoumanian et al., 2011]. As a result, the inferred density profile falls off as $\rho(r) \propto r^{-2}$ at large distances, r, from the peak of the filament profile.

ii. Filaments show a universal characteristic width of 0.1 pc [Arzoumanian et al., 2011]. The column densities of the observed filaments in different clouds from the Herschel Gould Belt Survey imply a broad distribution of Jeans lengths (spanning one order of magnitude, up to 1 pc). However, the observed distribution of mean filament widths is much narrower than the Jeans length distribution, with a mean of 0.1 pc and a standard deviation of 0.03 pc. Filaments therefore seem to have approximately the same width regardless of their density.

iii. The majority of dense cores lie on filaments [Men'shchikov et al., 2010]. In the Aquila Rift, 60 − 75 % of starless cores are found within 0.1 pc of a filament ridge, while the number increases to 70 − 90% for candidate pre-stellar cores[2] [Könyves et al., 2015].

The spacing of cores on filaments has been investigated by a number of works, with no definitive consensus. Spacings comparable to the Jeans length are often measured [Kainulainen et al., 2016b], but also spacings of the order of several times the filament width have been found[Busquet et al., 2013, Kainulainen et al., 2016a]. A number of works highlight the existence of overdensities at the edges of filaments [e.g. Kainulainen et al., 2016a]. A study of a sample of Herschel filaments from various clouds found a power law distribution of densities along the filament ridge [Roy et al., 2015].

---

[2]Pre-stellar cores are structures likely to form stars based on the Bonnor-Ebert criterion for collapse of a pressurized self-gravitating sphere [Bonnor, 1956, Ebert, 1955].

Filaments sometimes form distinct patterns such as hub systems (where filaments converge to point-like regions) or sets of parallel low density filaments (referred to as striations). Such phenomenological groupings are useful in the early stages of structure characterization, but will inevitably become obsolete as our physical understanding of these systems progresses.

1.2 Molecular cloud kinematics

Though instrumental for forming an interpretation of cloud structure, Herschel observations lack information on gas kinematics. To gain insight on this aspect of cloud structure, we review results from line emission surveys that have made follow-up observations of Herschel filaments. Unlike the Herschel results, at this stage the kinematic signatures of filaments are far from showing 'universal' characteristics.

Measurements of the velocity dispersion of spectral lines probe the nature of the internal motions in filaments. Looking at dense gas tracers (N_2H^+, $C^{18}O$) Arzoumanian et al. [2013] found trans-sonic[3] linewidths ($\sim 0.3\,km/s$) for filaments with central column densities $N(H_2) < 10^{22}\,cm^{-2}$. As the column density increases beyond this value, a correlation between the linewidth and the column density is found. These measurements, however, were made at a single position for each filament. In order for this trend to be significant, the linewidth at many positions along each filament should be non-varying − the structure should be 'velocity-coherent'. Such a situation is indeed observed: approximately constant linewidths are found in a filament of IC5146 [Arzoumanian et al., 2013] and in the extreme example of the Musca cloud [Hacar et al., 2016b]. Musca spans 6.5 pc on the plane of the sky and has sonic linewidths throughout its extent [Hacar et al., 2016b]. It also exhibits a measurable, but small, velocity gradient of 0.3 km/s/pc along its axis.

In contrast to these examples, other filaments exhibit complex kinematics, with multiple velocity components along the line of sight [Hacar et al., 2013, Fehér et al., 2016]. The B211/213 filament in Taurus, which as a whole shows large velocity dispersions and multiple components [Panopoulou et al., 2014], seems to be comprised of velocity-coherent substructures seen in $C^{18}O$ [Hacar et al., 2013]. In the Serpens Main and South molecular clouds Herschel filaments are found to contain smaller sub-filaments which are 2−3 times narrower than the Herschel typical width [Lee et al., 2014, Fernández-López et al., 2014]. This substructure could be arising either from the chemical properties of N_2H^+ or from the increase in resolution of a factor of ~ 2 compared to Herschel. Filaments in these clouds show a variety of velocity gradients along and/or perpendicular to their major axis. The observed velocity gradients along filaments vary from undetectable to $\sim 5\,km/s/pc$, with most lying at $\sim 1\,km/s/pc$. Much steeper gradients perpendicular to the main axis are observed ($\sim 10km/s/pc$). High-mass star forming regions [such as infrared dark clouds, Beuther et al., 2013] show velocity gradients of $\sim 25\,km/s/pc$ perpendicular to the filament axis. In Taurus B213 Palmeirim et al. [2013] find a perpendicular gradient of 0.5 - 1 km/s/pc.

Aside from such monotonic variations (of velocity as a function of position), oscillatory velocity patterns along filaments have been observed [Hacar and Tafalla, 2011]. Oscillations are also found across the major axes of striations in the envelope of the Taurus molecular cloud [Heyer et al., 2016]. These striations exhibit anisotropic velocities [Heyer et al., 2008] that are most likely connected to the presence of the magnetic field in the region. This is one example in which the magnetic field dynamically affects the structure and evolution of clouds. In the following section we present observational results regarding the connection of the magnetic field to molecular cloud structure.

1.3 The magnetic field in molecular clouds

The omnipresence of the magnetic field is shown primarily by the polarization of radiation emanating from the ISM. The field's existence was discovered through the polarization of starlight passing through diffuse nebulae [Hiltner, 1949, Hall, 1949]. Both starlight and dust emission polarization are produced as a result of the alignment of aspherical dust particles with the magnetic field in clouds [for a recent

---

[3]The sound speed is $c_s = 0.2\,km/s$ for gas at 10 K.

review see Andersson et al., 2015]. As a consequence, polarization measurements reveal the orientation of the field on the plane of the sky.

The most recent advance in mapping the magnetic field orientation was made by the Planck satellite [Planck Collaboration et al., 2015]. Planck produced an all-sky map of polarized thermal dust emission at arcminute resolution. Using Planck measurements, [Planck Collaboration et al., 2016b] compared the orientation of the magnetic field to that of cloud structures. They found that low column density structures ($N(H) \sim 10^{21}\,cm^{-2}$) are preferentially aligned with the plane-of-sky magnetic field. At the same time, higher column density structures ($N(H) \sim 10^{22}\,cm^{-2}$) tend to be perpendicular to the magnetic field on the plane of the sky. This result seems to persist at higher resolution, using starlight polarization measurements [Soler et al., 2016]. Striations are always found to lie parallel to the field orientation [Goldsmith et al., 2008, Palmeirim et al., 2013, Malinen et al., 2016].

Comparisons of field and structure orientation are likely affected by projection effects. In the case of the long filaments discussed earlier, these effects are likely minimal. For dense cores, with aspect ratios of ~ 2 typically, such effects can be significant. A way to alleviate this problem is by studying statistical samples of cores. In such a study, Tassis et al. [2009] found that cores are consistent with having their major axis perpendicular to the field orientation.

Apart from its correlation with cloud structure, the morphology of the field itself is also instructive. Both Planck and earlier measurements show smoothly varying, ordered fields at cloud scales [Planck Collaboration et al., 2016a,b, Alves et al., 2008, Chapman et al., 2011, Franco, 2015]. The degree of order in the field can be quantified by the ratio of the turbulent-to-ordered field strengths B_t/B_o and is a measure of the importance of the field with respect to turbulent motions [Hildebrand et al., 2009]. All measurements of this ratio to date find $B_t/B_o \leq 1$ from the diffuse ISM down to the scale of dense cores [e.g. Planck Collaboration et al., 2016c,a, Houde et al., 2016]. As a consequence, turbulent velocities are comparable to the Alfvén velocity (the speed at which magnetic disturbances propagate), i.e. sub/trans-alfvénic. At the smallest scales, within dense cores, the magnetic field shows a characteristic hourglass morphology with the core being elongated perpendicular to the mean field [Girart et al., 2006, Qiu et al., 2014]. In summary, observations provide a clear and quantitative view of the effect of the magnetic field on cloud structure and dynamics.

1.4 Interpretations and theoretical results

Having summarized the key observational findings regarding the state of matter, motions and the magnetic field in molecular clouds, we now present theoretical efforts that aim at a physical interpretation of these results.

Several theoretical interpretations for filamentary structure have been proposed. The common denominator in most is the assumption that filaments are approximately cylindrical. This assumption is mainly motivated by the abundance of elongated structure observed in clouds. The argument is statistical: if filaments were two-dimensional projections of some other geometry (e.g. sheets) they would not appear as omnipresent. So far only two works have attempted to test the assumption of cylindrical structure. Li and Goldsmith [2012] used HC_3N transitions to determine the volume density of molecular gas in the B213 filament in Taurus. They inferred a line-of-sight dimension of 0.25 pc, comparable to the short plane-of-sky dimension (width) of the filament (0.16 pc). Lee et al. [2014] assumed isotropic 3D turbulence and inferred a depth of 0.15 pc from the velocity dispersion and centroid velocity variation of N_2H^+ data. However, since both studies used a high density tracer, their results are consistent with a clumpy sheet-like medium. This lack of firm observational support of cylindrical structure is a major shortcoming of current theoretical models of filamentary structure, and should be kept in mind throughout the following discussion.

The classic interpretation for filaments is that of a gaseous cylinder in static equilibrium [Chandrasekhar and Fermi, 1953, Stodólkiewicz, 1963, Ostriker, 1964]. In the non-magnetized case, Ostriker [1964] showed that infinitely long isolated isothermal cylinders are unstable to radial contraction if their mass per unit length exceeds the critical value of $M_{crit} = 2c_s^2/G$. This criterion is modified slightly with the existence of a toroidal magnetic field confining the cylinder [Stodólkiewicz, 1963]. A subcritical infinite cylinder is prone to a sausage-type instability, which is, however, prevented under the existence

of a uniform poloidal field (parallel to its major axis) [Nagasawa, 1987]. Fiege and Pudritz [2000] included the effect of non-thermal motions, external pressure and helical magnetic fields. They found that poloidal fields increase the critical line mass, while toroidal fields tend to decrease it. Temperature gradients within the filament can only add a support of $20-30\%$ [Recchi et al., 2013]. When magnetic fields perpendicular to the main axis are assumed, cylinders evolve to flattened triaxial configurations [Tomisaka, 2014, Auddy et al., 2016]. All static equilibria (except in the case of a toroidal magnetic field) have radial profiles much steeper than the observed r^{-2}.

A number of works have investigated dynamically evolving (infinite) cylinders. Inutsuka and Miyama [1992] showed that rapidly contracting supercritical filaments condense to a spindle, while slowly collapsing critical filaments develop fragments separated by 8 times the cylinder scale height (4 times the diameter). This, however, was not observed in the simulations of Clarke et al. [2016] when they imposed a single wavelength perturbation on an initially subcritical cylinder. Kawachi and Hanawa [1998] showed that the collapse of an infinite cylinder with a polytropic equation of state proceeds in two phases: first, the radius decreases with density and then the very thin cylinder grows in mass by accretion (inside-out collapse). This final phase shows radial profiles like the observed r^{-2}.

Although instructive for the evolution of individual filaments, the treatment of individual cylinders (all the above works) cannot explain the formation of such structures. Such insights can be found through numerical simulations of entire clouds. In such works filaments appear as a result of a variety of situations: they are seen as long-lived flow features [Gómez and Vázquez-Semadeni, 2014], transient structures formed at the stagnation points of shocks [Federrath, 2016], or formed by shear and supported by magnetic forces [Hennebelle, 2013], or even by magnetic-field channelled gravitational contraction and fragmentation [Nakamura and Li, 2008].

Primarily based on the Herschel results, an observationally-driven view of star formation has been put forward [André et al., 2014]. In this view, filaments are an essential step in the process leading to the formation of pre-stellar cores. It is proposed that clouds first develop a network of filaments (modelled as isothermal cylinders), which in turn form cores via gravitational fragmentation. Studies found that thermally supercritical filaments contain most pre-stellar cores and higher velocity dispersions [Arzoumanian et al., 2013]. It is proposed that such filaments, found to be gravitationally bound, are partially supported against radial collapse due to enhanced turbulence in their interiors and fragment to form cores via gravitational instability. The enhanced turbulence is proposed to arise from accretion across the major axis, and observations of such gradients are seen as support of this picture. Thermally subcritical filaments do not harbour star formation and are viewed as transient features.

This picture is challenged by a number of observational and theoretical results. First, simulations of converging flows [Chen and Ostriker, 2015] and gravitational fragmentation of sheets permeated by a strong magnetic field [Van Loo et al., 2014] find that cores form simultaneously with filaments. Second, studies in the Chamaeleon [Gahm et al., 2002] and Taurus complexes [Panopoulou et al., 2014] find that it is highly unlikely for the cores to remain confined within their 'parent' filaments. Third, the observed orientation of the magnetic field with respect to the filaments is not taken into account in the proposed view. At the very least, the field will impose anisotropic turbulent motions [Goldreich and Sridhar, 1995] in the interior of the filaments leading to yet unknown consequences on the modelled properties.

The significance of the magnetic field in the various scales involved in star formation has been investigated observationally in numerous works [e.g. Li et al., 2011]. The bulk of observational data points towards the existence of a dynamically important magnetic field (section 1.3). Such a strong magnetic field has major implications on the entire process of star formation [for a review see Mouschovias and Ciolek, 1999]. Strong magnetic fields have been shown to induce the formation of molecular clouds [Parker, 1966] and solve the angular momentum problem [Mouschovias and Paleologou, 1979]. This magnetically-controlled star formation theory also resolves the tension between the magnetic flux of prestellar cores and that of stars, through the subtle process of ambipolar diffusion [Paleologou and Mouschovias, 1983]. Through this process, the theory captures the essence of star formation from the fragmentation of (magnetically-supported) clouds [Mouschovias, 1976] to the initial mass function [Kunz and Mouschovias, 2009]. In this magnetically-controlled scenario, self-gravity is expected to cause collapse mainly along field lines, thereby producing structures that are flattened and elongated

perpendicular to the magnetic field orientation. Diffuse structures with negligible self-gravity will lie along field lines [see for example the formation of striations explained by Tritsis and Tassis, 2016]. These trends have been shown in numerical simulations with strong magnetization (where turbulence is subdominant to the magnetic field— sub-alfvénic) [e.g. Falceta-Gonçalves et al., 2008, Soler et al., 2013]. In these cases the field is ordered at large (cloud) scales. Another major prediction of the theory is the characteristic hourglass shape of pre-stellar core field morphologies. All the above predictions are in good agreement with the observational results so far.

1.5   Outline

In this work we present an observational study of molecular cloud properties, motivated by the search for the initial conditions of star formation.

We begin our effort by attempting to understand an apparent discrepancy between the observed 'characteristic' width of Herschel filaments and the spatial power spectra of the same data (chapter 2). We revisit the study of filament widths and find strong biases in the methodology adopted in previous studies. We also highlight independent observational evidence that does not support the existence of such a morphological characteristic in molecular clouds.

We proceed by investigating the connection of cloud structure and magnetic field in a poorly studied column density regime − intermediate column density gas related to cloud formation. We use optical polarization to map the magnetic field in the Polaris Flare, a translucent molecular cloud (chapter 3). The map is made with the RoboPol optopolarimeter, a novel instrument which is used for the first time for polarization measurements throughout its field of view. For this reason, software for control of systematics is implemented and tested as part of this project. The resulting map shows a large-scale ordered magnetic field on the plane of the sky. We compare the orientation of the field to dust filaments on the Herschel image of the cloud and estimate the strength of the plane-of-sky field and its importance relative to turbulence (chapter 4). Finally, we summarize the conclusions of this work in chapter 5.

Chapter 2

Insights on filament morphology

One of the key results from the Herschel survey of dust emission in nearby clouds was that filaments seem to have a 'characteristic' width of 0.1 pc. This result posed an unexpected constraint on theoretical views of molecular clouds and proved elusive to reproduce in numerical simulations [e.g. Smith et al., 2014, Ntormousi et al., 2016]. A number of independent observational results were in tension with the typical width of filaments: the absence of this characteristic scale on the power spectra of Herschel images [Miville-Deschênes et al., 2010], the existence of substructure seen in line emission within Herschel filaments Hacar et al. [2013] and the wide range of widths within individual filaments Juvela et al. [2012]. In the work presented below, we attempted to explain the observed inconsistencies. By carefully performing and testing the previously adopted methodology for measuring filament widths, we showed that the 'characteristic' width is most likely an artifact of the analysis.

A closer look at the 'characteristic' width of molecular cloud filaments

G. V. Panopoulou,[1,2]★ I. Psaradaki,[1] R. Skalidis,[1] K. Tassis[1,2]★ and J. J. Andrews[2]

[1]*Department of Physics and ITCP†, University of Crete, 71003 Heraklion, Greece*
[2]*Foundation for Research and Technology – Hellas, IESL, Voutes, 71110 Heraklion, Greece*

ABSTRACT

Filaments in *Herschel* molecular cloud images are found to exhibit a 'characteristic width'. This finding is in tension with spatial power spectra of the data, which show no indication of this characteristic scale. We demonstrate that this discrepancy is a result of the methodology adopted for measuring filament widths. First, we perform the previously used analysis technique on artificial scale-free data, and obtain a peaked width distribution of filament-like structures. Next, we repeat the analysis on three *Herschel* maps and reproduce the narrow distribution of widths found in previous studies – when considering the average width of each filament. However, the distribution of widths measured at all points along a filament spine is broader than the distribution of mean filament widths, indicating that the narrow spread (interpreted as a 'characteristic' width) results from averaging. Furthermore, the width is found to vary significantly from one end of a filament to the other. Therefore, the previously identified peak at 0.1 pc cannot be understood as representing the typical width of filaments. We find an alternative explanation by modelling the observed width distribution as a truncated power-law distribution, sampled with uncertainties. The position of the peak is connected to the lower truncation scale and is likely set by the choice of parameters used in measuring filament widths. We conclude that a 'characteristic' width of filaments is not supported by the available data.

Key words: methods: statistical – stars: formation – ISM: clouds – ISM: individual objects: Polaris Flare – ISM: individual objects: Aquila Rift – ISM: individual objects: IC 5146.

1 INTRODUCTION

Studies of the structure of molecular clouds can provide clues on how gas accumulates to form stars. Gas in molecular clouds is found to be ordered in filamentary structures, a result highlighted especially by *Herschel* observations of dust emission in nearby clouds (André et al. 2010). Dense, self-gravitating filaments are often found to be co-spatial with young stars and dense pre-stellar cores (e.g. Hartmann 2002; André et al. 2010; Polychroni et al. 2013; Könyves et al. 2015), and hence may be important for understanding star formation.

One of the most striking results from analyses of *Herschel* data is that filaments in the Gould Belt clouds are found to exhibit a narrow distribution of average cross-sectional widths[1] (Arzoumanian et al. 2011). This sharply peaked distribution (with a mean at ∼0.1 pc and with ∼70 per cent of values within 0.06–0.14 pc;

Arzoumanian et al. 2011; Koch & Rosolowsky 2015) contains filaments spanning more than two orders of magnitude in column density.

This finding seems to contradict the expectation that filaments should contract (due to gravity) and hence increase in density while decreasing in radius. Though the existence of this characteristic scale is still poorly understood, it has been suggested that it must be connected to some physical mechanism, perhaps one involved in filament formation (Arzoumanian et al. 2011; André et al. 2014). Qualitative arguments have connected this characteristic scale to the transition from supersonic to trans-sonic turbulence (Arzoumanian et al. 2011) and to the ambipolar diffusion length scale (for both gravitationally unbound and bound structures; Hennebelle 2013; Hennebelle & André 2013). Simple analytical models propose that the independence of filament width from column density may be a result of the balance between accretion on to the (self-gravitating) filaments and dissipation of the turbulence within them (Heitsch 2013; Hennebelle & André 2013). Fischera & Martin (2012) offered pressure confinement of isothermal cylinders as a possible model for self-gravitating filaments. Most recently, Auddy, Basu & Kudoh (2016) proposed a model in which filaments are magnetic ribbons, produced by large-scale, trans-Alfvénic turbulent flows in a strong magnetic field. Their model is able to reproduce average widths that vary within a factor of 2 across two

[1] Throughout this paper the term 'width' refers to the full width at half-maximum (FWHM) of a Gaussian fit to the innermost part of a filament radial profile, the same definition used by Arzoumanian et al. (2011).

orders of magnitude in column density. However, simulations that either include self-gravity and neglect magnetic fields or vice versa have yet to reproduce the observed distribution and independence on column density (Smith, Glover & Klessen 2014; Ntormousi et al. 2016). Federrath (2016) simulated isothermal, self-gravitating, magnetized clouds with super-Alfvénic-driven turbulence. His finding is that filament widths are peaked at 0.1 pc and appear constant for one order of magnitude in column density when turbulence is operating. The proposed explanation is that the characteristic width is set by the dissipation of turbulence in shocks. His model, however, fails to reproduce the correlation between filament and magnetic field orientations found in molecular clouds with *Planck* (Planck Collaboration XXXV 2016).

One particularly puzzling observation regarding the apparent characteristic width of filaments is the absence of its imprint on the spatial power spectra of *Herschel* cloud images (Miville-Deschênes et al. 2016). The spatial power spectrum of the 250 μm map of the translucent non-star-forming Polaris Flare is well fit by a power law from ∼2 to ∼0.02 pc (Miville-Deschênes et al. 2010). At the same time, the distribution of filament widths in this cloud is found to have a prominent peak at 0.05–0.07 pc (Arzoumanian et al. 2011; Panopoulou, Psaradaki & Tassis 2016). A similar situation is found in the Chamaeleon molecular cloud complex, where filament widths are peaked around 0.12 pc with a spread of 0.04 pc (Alves de Oliveira et al. 2014). However, these authors find no indication of a typical filament width in the Δ-variance spectra (Stutzki et al. 1998) of the clouds, even though the signature of cores and clumps is easily identified as a change in the slope of the Δ-variance spectrum at the corresponding size scales.

Motivated by this apparent discrepancy, in this work we retrace the steps in the analyses of filament width distributions. In Section 2, we briefly describe the analysis used for constructing the distribution of filament widths. We first perform this analysis on an artificial filamentary image with no characteristic scale and find the distribution of widths to have a broad peak (Section 3.1). We then repeat the analysis on *Herschel* data of three clouds (the Polaris Flare, Aquila and IC 5146, Section 3.2), showing that the narrow spread of the distribution of widths found in previous studies is likely a consequence of averaging along filaments. The constancy of filament widths may therefore not be inferred from this spread. Furthermore, we investigate the position of the peak of the distribution of widths and find that it is likely a result of the choice of range within which the filament width has been measured (Section 3.3). Finally, we summarize our results in Section 4.

2 METHODS

In order to reproduce the distributions of filament widths for the three clouds presented in Arzoumanian et al. (2011, the Polaris Flare, Aquila, and IC 5146) , we follow an analysis similar to their study. We use primarily the *Herschel* Spectral and Photometric Imaging Receiver (SPIRE) maps of these clouds at 250 μm, unless explicitly stated otherwise in the text.

First, we employ the Discrete Persistent Structures Extractor (DISPERSE; Sousbie 2011) to identify the filamentary structures in each image. DISPERSE analyses the topology of a given map and extracts its skeleton, which corresponds to the ridges of elongated structures. We select the parameters of DISPERSE so that the resulting skeletons are visually similar to those shown in the previous studies of the three clouds (Arzoumanian et al. 2011, IC 5146, fig. 3; André et al. 2014, Polaris Flare, fig. 1; Könyves et al. 2015, Aquila, fig. 3). The values of the parameters used are given in Appendix A.

Next, we provide the skeleton of DISPERSE and the corresponding *Herschel* image of each cloud as input to the Filament Trait-Evaluated Reconstruction (FILTER) code[2] (Panopoulou et al. 2014). The objective of FILTER is twofold. First, it post-processes the skeleton of DISPERSE to only include continuous, non-spurious, structures (e.g. peaked well above the noise level). This is done by taking cross-sections at every pixel along the filament ridge and assessing each intensity profile. Profiles that are not peaked around the filament ridge and above the noise level are rejected. Secondly, FILTER measures the width of each intensity profile along a filament. The width is defined as the FWHM of a Gaussian fit (with offset) to the innermost part of the profile (as in Arzoumanian et al. 2011). In order to find this value automatically for every profile, Gaussians are fit iteratively to smaller and smaller distances from the filament ridge. The initial range used for fitting is a free parameter of the algorithm. As has been shown by Smith et al. (2014), the distance up to which a Gaussian is fit is crucial in the determination of the width, as at larger distances the fit tends to miss the innermost part of the profile. In each section, we shall state explicitly which starting value for the fitting range has been used. At the end of the iteration, the most frequent FWHM is assigned as the width of the profile, after deconvolution from the beam size.[3] The deconvolved width is found (as in Könyves et al. 2015) by $\mathrm{FWHM_d} = \sqrt{\mathrm{FWHM}^2 - \mathrm{HPBW}^2}$, where HPBW is the half-power beam width of the map (18 arcsec for 250 μm, which corresponds to 0.013, 0.023 and 0.04 pc at the assumed distances to the Polaris Flare, 150 pc, Aquila, 260 pc and IC 5146, 460 pc, respectively). Finally, only sufficiently elongated structures (with at least a 3:1 length to mean width ratio) are included in the final sample of filaments that we consider for further analysis. The post-processed skeletons of the three *Herschel* images used in this work are shown in Appendix A.

FILTER provides two different ways of constructing width distributions:

(i) A distribution of the FWHM measured at all points along the spines of filaments can be created. Information on the structure to which each measurement belongs is discarded in this way (e.g. Panopoulou et al. 2016). We refer to this kind of distribution as the distribution of all profile widths.

(ii) A distribution of the mean FWHM of filaments can be constructed. This second type of distribution has been found to show a 'characteristic width' in previous studies (e.g. Arzoumanian et al. 2011). We refer to this type of distribution as the distribution of filament-averaged widths (or of mean filament widths).

With FILTER, the mean width of each filament is found by taking the average value of the FWHM measured at each point (pixel) along the filament ridge. In other studies, the mean width has been found by fitting a Gaussian to the mean filament profile (e.g. Arzoumanian et al. 2011; Smith et al. 2014; Benedettini et al. 2015; Koch & Rosolowsky 2015). In the work of Koch & Rosolowsky (2015), a non-parametric width determination is also used when Gaussian fitting is not possible. In the following analysis, we find the mean width of a filament by averaging the FWHM of all its profiles, as this process is automated, objective and easily reproducible. We note that the method used to calculate the average width of a filament

---

[2] The code is available at https://bitbucket.org/ginpan/filter.
[3] The most frequent FWHM has been found through tests (on data and artificial images) during code development to be a robust estimator of the width.
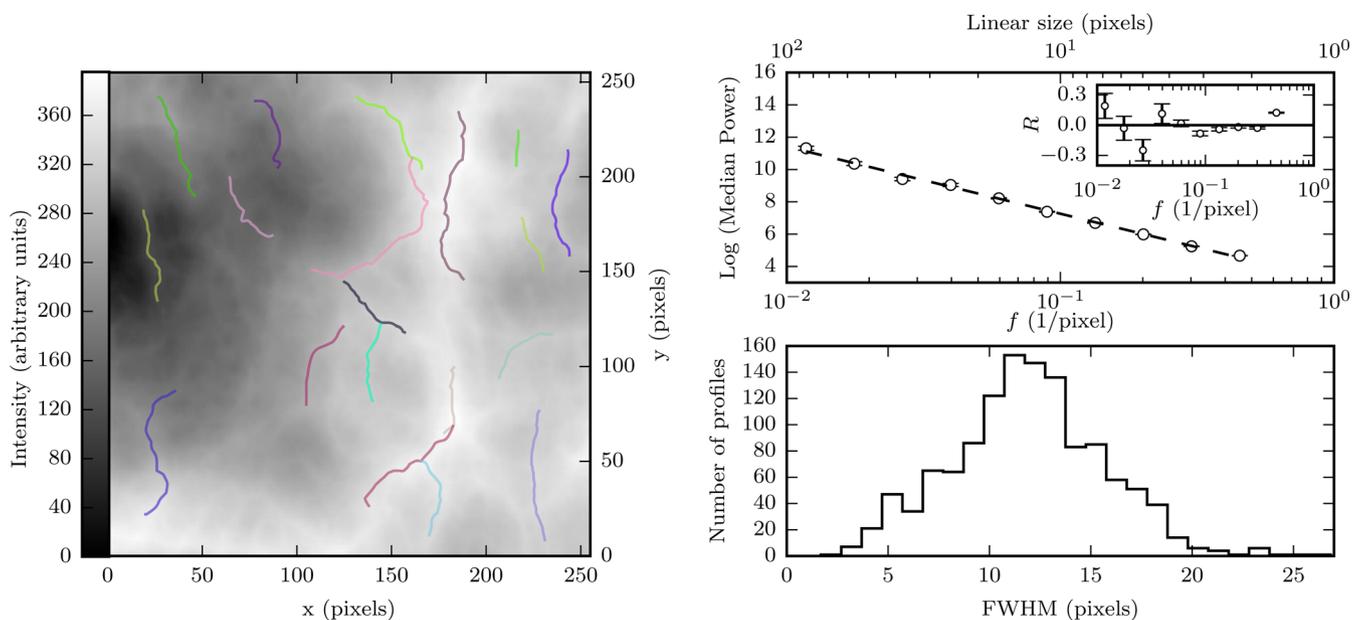
Figure 1. Left: image generated using Ridged Multifractal Noise (256 pixels on each side), with the skeleton of filaments having an aspect ratio of at least 3:1 overplotted. Top right: spatial (azimuthally averaged) power spectrum of image on left (open circles) and linear fit in log–log space (dashed line). Corner inset: residual of the fit, $R = \log(\text{median power}) - \log(\text{fit})$. Bottom right: distribution of the widths measured at each point along the ridges of the filaments in the artificial image on the left.

should not affect the statistical properties of the distribution of mean filament widths (mean and spread), as long as a large number of filaments is used. Indeed, the difference between our approach of measuring mean filament widths and that of other studies does not affect the properties of the distributions of mean filament widths, as both the mean and spread are in good agreement with those of (Section 3.2; Arzoumanian et al. 2011).

3 RESULTS

3.1 Can a peaked size distribution arise from scale-free data?

The scale-free spatial power spectrum of the *Herschel* Polaris Flare image (at 250 μm) is in tension with the existence of a 'characteristic' width of the filaments in the same image (Miville-Deschênes et al. 2010; Arzoumanian et al. 2011). It may be argued that in some circumstances, the imprint of a characteristic scale on the spatial power spectrum is 'hidden'. We use simple artificial images to explore if such a situation may arise (see Appendix B). We demonstrate that if structures with a characteristic scale are introduced, an imprint of this scale is apparent in the spatial power spectrum – as long as the structures are easily discernible from background noise, as is the case for filaments in the Polaris Flare.

In this section, we explore the opposite situation: whether a preferred scale can arise from analysing an image with a scale-free spatial power spectrum. To this end, we create a scale-free image and perform the analysis described in Section 2.

To construct the image, we use the Ridged Multifractal model from the suite of noise-synthesis models implemented in the PYTHON library pynoise (http://pynoise.readthedocs.io). Noise synthesis models (Musgrave, Kolb & Mace 1989) are used for creating natural-looking complex and heterogenous patterns (landscapes, clouds). They are based on the widely used, scale-free, fractional-

Brownian-motion (fBm; e.g. Stutzki et al. 1998) but use band-limited Perlin noise (Perlin 1985) functions for the basis function instead of sine waves as in pure fBm.

The resulting image (256 pixels on each side) is filamentary, as can be seen in Fig. 1 (left). We adjusted the parameters of the model to obtain an image whose spatial (azimuthally averaged) power spectrum has the form of a power law (Fig. 1 – top right). The one-dimensional spatial power spectrum is constructed as in Pingel et al. (2013), by taking the median power in concentric annuli around the zero-frequency pixel in the two-dimensional power spectrum. The annuli are chosen so that a uniform sampling of scales in logarithmic space is obtained. The sample size ranges from 29 (for the smallest annulus) to ~23 000 values. The errors on the median value (comparable to the size of the points in the figure) are calculated by bootstrap resampling. For every annulus, we resample the distribution of intensities and calculate the median of the resampled distribution 100 times. The error on the median is the standard deviation of these 100 median values.

We performed the analysis described in Section 2 on the artificial image. The resulting skeletons of filament-like structures (having at least a 3:1 aspect ratio) are overplotted in the left-hand panel of Fig. 1. The distribution of widths measured at each point along these elongated structures (first method) is shown in the bottom-right panel of Fig. 1. The initial fitting range used is ±10 pixels from the ridge (see discussion in Section 2 regarding the fitting range). The distribution is clearly peaked around 12 pixels, and has a spread of 3.8 pixels.

The existence of a peak in the distribution of widths of the structures extracted by DISPERSE in this image is inconsistent with its scale-free (power-law) spatial power spectrum. Since the construction of the power spectrum is straightforward, we conclude that the existence of the preferred scale (peak of the width distribution) is most likely an artefact of the analysis of apparent filament widths.

3.2 Why is the distribution of widths narrow?

We now turn to the *Herschel* data of the Polaris Flare, Aquila and IC 5146. When combining width measurements of filaments in these clouds, Arzoumanian et al. (2011) find a distribution of mean filament widths with a spread of only 0.03 pc. It is this small spread that seems to imply that filaments have a 'characteristic width'. In this section, we attempt to understand why the distribution of widths is found to have such a narrow spread.

We follow the analysis of Section 2 on the *Herschel* SPIRE-250 μm map of each cloud. We construct the distribution of widths measured at every cross-section (profile) of the filaments in the map. Studies finding a 'characteristic width' have used the width of the mean profile of individual filaments to create the distribution of (mean filament) widths (e.g. by fitting a Gaussian to the mean filament profile, Arzoumanian et al. 2011). For comparison, we also construct the distribution of mean filament widths (as explained in Section 2).

In Fig. 2, we show the normalized distribution of filament-averaged widths (dotted) and that of all profile widths (solid), for each of the clouds mentioned above. The number of filaments used to create these distributions as well as the mean and spread of the distributions are shown in Table 1. The initial fitting range used for all distributions was ±0.1 pc from the filament ridge. We find that the mean and spread of the distribution of mean filament widths for the filaments in IC 5146, and for those in all three clouds combined are in agreement with those found by Arzoumanian et al. (2011, the reported mean and spread were 0.1 and 0.03 pc, respectively).

When comparing the distribution of all filament profiles to that of mean widths, we find that *the shapes of the two kinds of distribution are clearly different.* The filament-averaged width distribution is much more concentrated around its mean value ($\sigma_{\mathrm{all}} \approx$ [2–3] $\times \sigma_{\mathrm{mean}}$, from Table 1), and lacks the tails seen in the width distribution of all profiles. The same effect is seen when filaments from all clouds are combined in a single distribution (the bottom panel of Fig. 2).

The differences between the two kinds of distributions can be easily understood considering the central limit theorem (CLT). The average value of a sample of profile widths (filament) is expected to follow a Gaussian distribution, provided there is a sufficient number of filaments and that widths are not strongly correlated within a filament. This distribution of averages is centred around the mean of the parent distribution (that containing the widths of all filament profiles). It is therefore not surprising that the spread in the distribution of filament-averaged widths is small. The information conveyed by the narrowness of this distribution is simply that the mean width of filaments is known with very good accuracy; note that the widths of individual filaments are constant, as has often been interpreted.

We now wish to understand the factors that determine the spread of the distribution of mean filament widths (i.e. we wish to find the parameters P that enter in $\sigma_{\mathrm{mean}} = f(P)$). From the original form of the CLT (which assumes measurements are completely uncorrelated), we expect that

$$\sigma_{\mathrm{mean}} = \sigma_{\mathrm{all}}/\sqrt{N}, \tag{1}$$

if all filaments have the same number of profiles N (which is proportional to the filament length). However, the lengths of filaments follow a distribution of values $g(N)$, and therefore we expect $\sigma_{\mathrm{mean}} = f(\sigma_{\mathrm{all}}, g(N))$.

In order to test whether these two parameters are sufficient to explain the observed σ_{mean} in the Polaris Flare, we attempt to
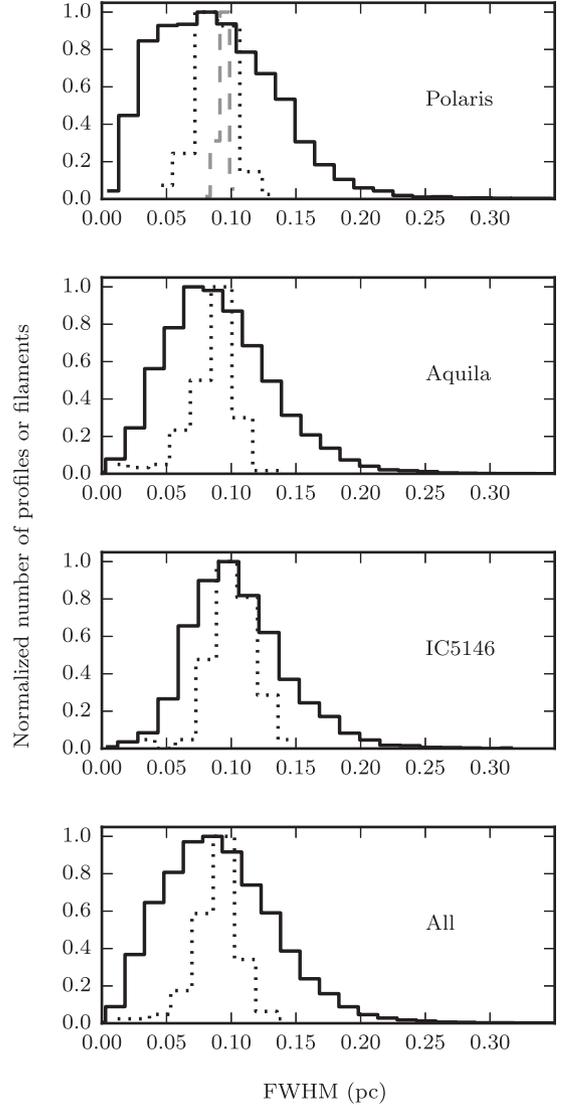
Figure 2. Comparison of filament-averaged (dotted) and non-averaged (solid black) width distributions for the three different clouds (top 3 plots), and for all filaments in the three clouds combined (bottom). All FWHM have been deconvolved from the beam size. The grey dashed line (top panel) shows the distribution of mean filament widths resulting from the Monte Carlo simulation described in the text (Section 3.2).

Table 1. Properties of width distributions shown in Fig. 2. Includes the number of filaments in each distribution, N_{fil}, the number of profiles of all filaments, N_{pr}, the mean and standard deviation of the distribution of filament-averaged widths ($\langle W_{\mathrm{mean}} \rangle$ and σ_{mean}), and those of the distribution of all profile widths ($\langle W_{\mathrm{all}} \rangle$, σ_{all}).

Cloud	N_{fil}	N_{pr}	$\langle W_{\mathrm{mean}} \rangle$ (pc)	$\langle W_{\mathrm{all}} \rangle$ (pc)	σ_{mean} (pc)	σ_{all} (pc)
Polaris	100	24 969	0.095	0.097	0.014	0.05
Aquila	79	14 315	0.095	0.094	0.02	0.04
IC 5146	58	5277	0.11	0.11	0.02	0.04
All	237	44 561	0.09	0.09	0.02	0.04

reproduce the distribution of mean filament widths from that of all profile widths as follows. We perform a Monte Carlo simulation where samples of widths are drawn randomly from the observed distribution of all profile widths. These samples are randomly assigned to 100 groups (or fake 'filaments'), corresponding to the 100 filaments found in the Polaris Flare. The size of each group (corresponding to the length of the 'filament') is drawn from the observed distribution of filament lengths. We then calculate the average width of each group and construct the distribution of group-averaged widths. This process produces a distribution with $\sigma_{\rm mean}^{\rm rand} = 0.004$ pc, much narrower than what is observed (see grey dashed distribution at the top panel of Fig. 2).

The information that is lacking is that widths within the telescope beam size are strongly correlated. We provide evidence for this by constructing the autocorrelation function (ACF) of widths along the ridge of filaments (see Appendix C). By performing a simulation similar to that described above, including this final piece of information, we are able to reproduce the observed spread of the distribution of mean widths ($\sigma_{\rm mean} = 0.011$ pc, see Appendix C). Therefore, the parameters that most significantly affect $\sigma_{\rm mean}$ can be summarized as $\sigma_{\rm mean} = f(\sigma_{\rm all}, g(N), beam)$. In other words, there is no other information to be extracted from the spread of the filament-averaged width distribution.

Since the structure of individual filaments cannot be inferred uniquely from their average properties, we must examine how much does the width throughout an entire filament vary. This question can be answered by considering the standard deviation of all widths measured at different positions along the spine of a filament. Individual filaments are known to exhibit a range of FWHM along their spines (0.1–1, 0.07–0.2, 0.1–2.5 pc; Juvela et al. 2012; Malinen et al. 2012; André et al. 2016). In the Polaris Flare, the standard deviation of profile widths in a given filament is on average $\langle \sigma_{\rm fil} \rangle = 0.04$ pc. This value is similar to the spread of the parent width distribution ($\sigma_{\rm all} = 0.05$ pc, Table 1). Therefore, the width varies significantly throughout the entire extent (length) of an individual filament. This finding is also supported by the two-dimensional distribution of filament widths across the Polaris Flare map, presented in Panopoulou et al. (2016) – their fig. 7. Filament widths do not exhibit large-scale regularities, but rather fluctuate in a seemingly random manner throughout the cloud.

3.3 Why is the peak of the distribution of filament widths at 0.1 pc?

The findings of Section 3.2 along with the scale-free power spectrum of the Polaris Flare, render the existence of a 'characteristic' width of filaments highly unlikely. Consequently, the previously reported peak of the filament-averaged width distribution at 0.1 pc cannot be explained by such a view.

In order to understand the origin and position of this peak, we examine in detail the width distribution of all filament profiles in the Polaris Flare. Fig. 3 shows the distribution of log(width) with equally sized bins in logarithmic space. It is strongly peaked and the mean and median values (vertical solid and dotted lines, respectively) differ by only 5×10^{-3} pc. Interestingly, the part of the distribution at scales larger than the mean resembles a straight line (in logarithmic space). A linear fit (in log–log space) to the distribution is shown with a grey solid line in Fig. 3.

This resemblance of part of the distribution to a power law is not surprising if we consider the evidence for scale-free, or self-similar, structures in the ISM within a range of scales (e.g. Stutzki et al. 1998; Elmegreen & Scalo 2004; Tassis 2007; Elia et al. 2014;
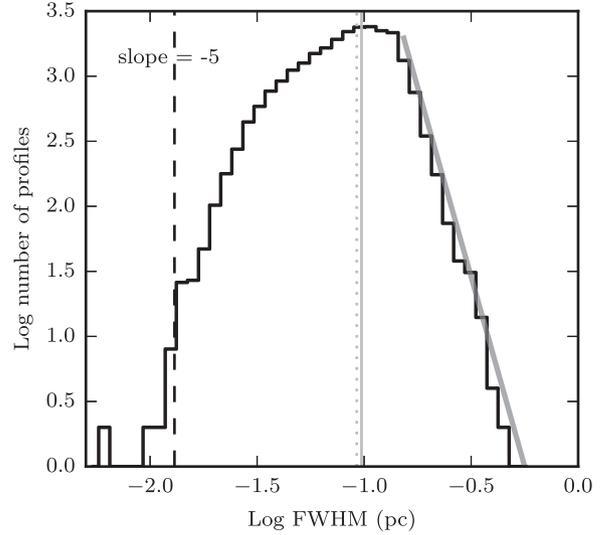
Figure 3. Distribution of the logarithm of all profile widths of filaments in the Polaris Flare. At scales larger than 0.15 pc, the distribution resembles a power law (the grey solid line is a linear fit in log–log space to the logarithmically spaced bins). The mean and median of the distribution are shown by the vertical solid and dotted lines, respectively. The *Herschel*-SPIRE beam size (at 250 μm) at the distance of the Polaris Flare (150 pc) is shown with the dashed vertical line.

Miville-Deschênes et al. 2016). Elmegreen & Falgarone (1996) find size and mass distributions in clouds consistent with those arising from a fractal. In the case of the Polaris Flare, the scale-free nature of the cloud is evidenced by its power-law spatial power spectrum (Miville-Deschênes et al. 2010). We note that because the Polaris Flare is gravitationally unbound and is not forming stars (Heithausen 2002; Ward-Thompson et al. 2010; Wagle et al. 2015), self-similarity is not expected to break down at the typical scale of pre-stellar cores (0.1 pc, e.g. Goodman et al. 1998). Therefore, a power-law distribution of filament widths (in accordance to other length scales) within some range of scales is not unreasonable.

If a power-law size (width) distribution is intrinsic to the cloud, we expect that this power law will be truncated at large scales at a fraction of the size of the *Herschel* map and at small scales (at least) by the resolution. In the process of imaging the cloud dust emission and measuring sizes on the map, errors are introduced. Errors have the effect of smoothing the distribution near the lower truncation limit (Koen & Kondlo 2009). If these errors are assumed Gaussian, then the shape of the (truncated) power-law distribution can be analytically modelled (Koen & Kondlo 2009) and is similar to that of the distribution in Fig. 3: it possesses a peak near the lower truncation limit followed by a power-law tail. The analytical form of the distribution of measured widths (W) is

$$f(W) = \int_{W_{\rm min}}^{W_{\rm max}} \frac{\gamma w^{-(\gamma+1)}}{\sqrt{2\pi}\sigma(W_{\rm min}^{-\gamma} - W_{\rm max}^{-\gamma})} \exp\left[-\frac{1}{2}\left(\frac{W-w}{\sigma}\right)^2\right] dw,$$

(2)

where w is the width before introducing measurement errors, σ is the measurement uncertainty, $\gamma + 1$ is the power-law slope, and $W_{\rm min}$, $W_{\rm max}$ are the sizes at which the power law is truncated due to (at least) the resolution and (at most) the map size. For what follows, we will consider only non-negative values of γ. The average value can be obtained by (numerical) integration of the formula:

$$\langle W \rangle = \int_{\rm HPBW}^{\rm map\,size} f(W) W \, dW,$$

(3)
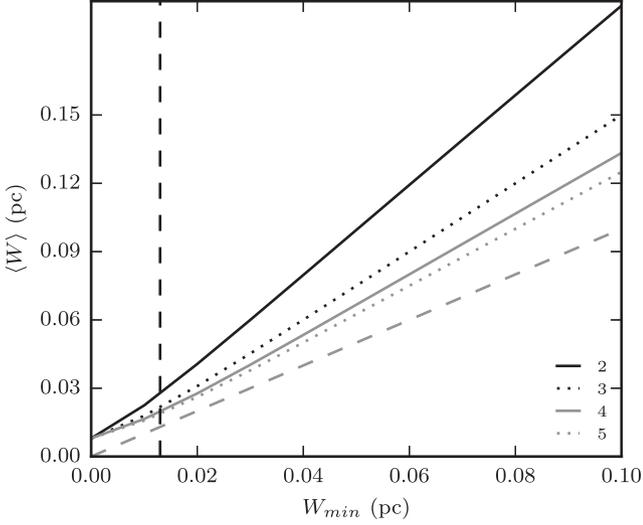
Figure 4. Dependence of the mean measured width of profiles on W_{min} for different values of γ (ranging from 2 to 5 and marked with labelled lines). Values of $W_{max} = 5$ pc and $\sigma = 0.02$ pc were used, since there is little dependence of $\langle W \rangle$ on these parameters (see the text). A $1-1$ correlation is shown with the dashed grey line. The dashed vertical line shows the *Herschel*-SPIRE beam size (at 250 μm) in parsecs at the distance to the Polaris Flare (150 pc).

where the integration is performed within the bounds set by the observations (resolution limit and map size).

Therefore, if one could determine the parameters σ, γ, W_{min} and W_{max}, a prediction for the mean of the distribution of all profile widths could be obtained. In Section 3.2, we found that the mean of the distribution of all profile widths is coincident with the position of the peak of the filament-averaged distribution (as a result of the CLT). Consequently, measuring the mean of the former kind of distribution determines the peak of the latter. We note that the mean and peak of the distribution of filament-averaged widths are the same, as it is (approximately) Gaussian.

In Fig. 4, we explore the dependence of $\langle W \rangle$ on the parameters W_{min} and γ. $\langle W \rangle$ is plotted against W_{min} for $W_{max} = 5$ pc, $\sigma = 0.02$ pc, and different values of γ (ranging from 2 to 5, around a value of 4 implied by the slope of Fig. 3, and marked with solid and dotted lines). We find that there is no dependence of $\langle W \rangle$ on W_{max}. For γ in the range 2–5, constant W_{min} and σ, and W_{max} in the range 1–50 pc, $\langle W \rangle$ varies by less than 0.01 pc. Similarly, for constant W_{min} and W_{max}, and σ in the range 0.01–0.1 pc, $\langle W \rangle$ varies by less than 0.02 pc for any given γ within 2–5. On the contrary, $\langle W \rangle$ is very sensitive to the parameter W_{min}. Therefore, the lower scale at which a power law width distribution is truncated essentially sets the position of the peak in the distribution of filament-averaged widths.

We would like to identify the best-fitting parameters for the distribution of filament widths in the Polaris Flare, using a power law with measurement uncertainties. Koen & Kondlo (2009) provide the log-likelihood function for this model:

$$\mathcal{L} = -\frac{N}{2} \log 2\pi - N \log \sigma + N \log \gamma - N \log(W_{min}^{-\gamma} - W_{max}^{-\gamma})$$

$$+ \sum_{j=1}^{N} \log \int_{W_{min}}^{W_{max}} x^{-(\gamma+1)} \exp\left[-\frac{1}{2}\left(\frac{W_j - x}{\sigma}\right)^2\right] dx, \quad (4)$$

where W_j are the N different filament width measurements and σ is the Gaussian standard deviation on measurements of W_j (and is independent from W_j). Since, for the distributions of filament widths,
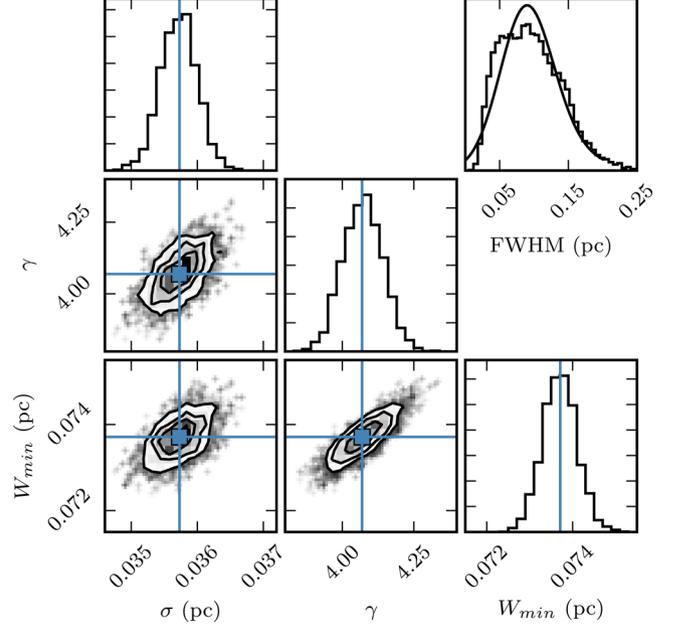
Figure 5. The posterior distribution of parameters from our MCMC model of the data of Fig. 3. Blue lines show the values returned by the MLE. On diagonal: one-dimensional histograms of model parameters: σ, γ and W_{min}. Lower diagonal: joint PDFs of the posterior distribution of the model parameters. Top right: comparison between normalized distribution of Fig. 3 (stepped histogram) with our model (equation 2), using a randomly selected set of parameter values from the posterior distribution of model parameters (smooth line).

the effect of W_{max} is insignificant, we set it to 10 pc (approximate size of the *Herschel* map) and solve for the best-fitting values of W_{min}, γ, and the measurement uncertainty, σ. We use the routine `minimize` within the `scipy.optimize` package, to find the values that maximize the log-likelihood. The resulting values for the parameters are $\sigma = 0.036$ pc, $\gamma = 4.07$ and $W_{min} = 0.074$ pc. We note that the slope found by fitting a line to the distribution in Fig. 3 (slope = 5) is in good agreement with the value found by maximizing the log-likelihood ($\gamma + 1 = 5.07$). By substituting γ and W_{min} in equation (3), we obtain $\langle W \rangle = 0.098$ pc, which is approximately equal to the mean of the observed distribution of widths.

Additionally, we would like to determine the range of parameter values implied by the filament width data. Instead of using a maximum likelihood estimate (MLE), we use the Markov Chain Monte Carlo (MCMC) algorithm EMCEE (Foreman-Mackey et al. 2013). EMCEE employs an affine-invariant ensemble sampler to probe the model parameter space. Our model uses 32 walkers to maximize the log-likelihood function in equation (4). We apply flat priors on W_{min} and γ, in the ranges: W_{min}: [0–0.5] pc, γ: [0.01–10]. We use the Jeffreys prior ($1/\sigma$) on σ to make it scale invariant. The range used for σ is [0–3] pc. We note that σ encapsulates the uncertainty introduced by two different processes: the imaging of the cloud (resolution) and the measurement of the width (analysis in Section 2). We therefore choose to leave σ as a free parameter (and do not set it equal to the image resolution) to account for both sources of error. 200 steps are sufficient for the 'burn-in' stage. We throw these data away, and run our model for 2000 additional steps to produce the posterior distribution.

The posterior distributions of model parameters (Fig. 5 – on diagonal) are strongly peaked, with standard deviations of 3×10^{-4} pc

Table 2. Values of the parameters returned by the MLE for distributions with different initial fitting ranges. The final column shows the values derived from the parameters using equation (3).

Fitting range (pc)	σ (pc)	γ	W_{min} (pc)	$\langle W \rangle$ (pc)
0.04	0.012	4.65	0.037	0.05
0.06	0.019	3.97	0.049	0.07
0.08	0.027	4.13	0.064	0.08
0.10	0.036	4.07	0.074	0.10
0.12	0.043	4.25	0.087	0.11
0.14	0.051	4.16	0.094	0.12
0.20	0.065	3.24	0.110	0.16
0.25	0.079	3.03	0.125	0.19

for σ, 0.07 for γ and 4×10^{-4} pc for W_{min}. Joint PDFs of the posterior distributions of model parameters are shown in the panels lower than the diagonal. As expected for uniform priors (and since our prior on σ is weak), the region of high-probability parameter space agrees with the results from the MLE (blue lines). The top-right panel in Fig. 5 compares the distribution of filament widths from Fig. 3 (histogram) to the functional form of equation (2) with values for the parameters drawn randomly from the posterior distribution of model parameters (smooth line). For the range of parameters used, the shape of the smooth curve varies very little (the variation is similar to the width of the plotted line). The model captures well the basic shape of the distribution and of the model parameter space.

For values of the parameters within 5σ of the mean of their corresponding distributions, we obtain from equation (3): $\langle W \rangle = 0.09$–0.1 pc. We conclude that the model used here accurately reproduces the position of the peak of the distribution of widths of Fig. 3 (within 0.01 pc). From the value of σ, we obtain a handle on the error introduced by the width calculation algorithm. Since the resolution is only 0.013 pc, the algorithm is the main source of measurement error.

The question that remains to be answered is what determines W_{min}, the value below which the power-law distribution is truncated. One obvious culprit could be the resolution limit. However, if W_{min} was equal to the telescope beam size (0.013 pc, shown by the vertical dashed line in Fig. 4), the mean of the distribution would fall below 0.03 pc, as seen from Fig. 4. Another possibility would be that the combined effect of the telescope resolution and the errors of the width-measurement algorithm are setting the lower limit. This corresponds to the parameter σ which is almost three times the beam size (for the distribution of widths in Fig. 3). W_{min}, however, is found to be almost six times the beam size, making both options unlikely.

A more likely possibility is that W_{min} is related to the range over which the Gaussian fit is performed to measure the width of a profile. In order to avoid fitting the wings of filament profiles, studies of filament widths have chosen to fit a Gaussian within a range of ∼0.1–0.4 pc from the filament spine (Arzoumanian et al. 2011; Juvela et al. 2012; Smith et al. 2014; Koch & Rosolowsky 2015; André et al. 2016; Federrath 2016). However, Smith et al. (2014) have shown that the selection of fitting range drastically affects the mean filament width.

We investigate this effect further for the filaments in the Polaris Flare, by creating distributions of widths with different initial fitting ranges, and repeating the MLE analysis for each one. The resulting values of the parameters are listed in Table 2. As can be seen in Fig. 6, the peak of the distribution of widths shifts towards lower values for smaller fitting ranges (vertical line segments on the top
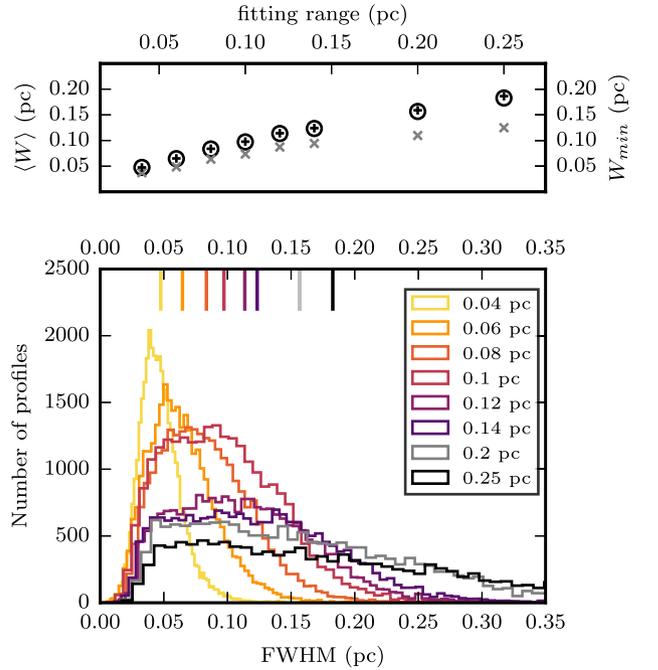
Figure 6. Top: the mean of the observed distributions (open circles) and that calculated from equation (3) (crosses) with the MLE values of the parameters, versus the fitting range (left vertical axis). Values of W_{min} returned by the MLE for each distribution as a function of fitting range are shown as grey crosses (right vertical axis). Bottom: distributions of beam-deconvolved profile widths in the Polaris Flare for different values of initial fitting range (distance from the axis of a filament). The vertical lines at the top show the mean value of each distribution.

of the main panel). From the top panel of Fig. 6 (left vertical axis), we find that the mean of the observed distributions (open circles) is in very good agreement with the mean calculated with equation (3) using the values of Table 2 (black crosses). Both quantities increase monotonically with the fitting range. This is because W_{min} also has such a dependence on the fitting range (Fig. 6 top panel, right vertical axis). Since the fitting range used in previous studies does not vary much, it is not surprising that the peak of the filament-averaged width distribution is found at similar values for different clouds.

Compared to the simulations of Smith et al. (2014), the mean width of filaments in the Polaris Flare increases slightly more abruptly as a function of fitting range. For a factor of ∼3 increase in fitting range, these authors find the mean width to increase by a factor of 1.5, whereas we find a factor of ∼2. However, any such comparison must consider the range that we use as an upper limit, because we fit Gaussians iteratively beginning from the quoted fitting range. Also, there is an indication in Fig. 6 that at larger ranges the slope tends to flatten out. Considering these factors, we find the scaling of mean width with fitting range to be strikingly similar between the simulated and observed filaments, perhaps hinting at common structural properties.

The dependence of the mean width on the fitting range suggests that selecting a scale over which to observe/measure a structure determines how important the innermost part of the structure will appear.[4] In the case of a scale-free structure, this can be understood,

---

[4] Observational evidence for substructure in *Herschel* filaments (through finer resolution imaging) already exists (see e.g. Fernández-López et al. 2014; Hacar et al. 2013; Henshaw et al. 2016, 2017).

as a fractal surface changes in character when examined at different scales: it appears smoother/flatter when observed from further away, but upon closer inspection substructure appears. Alternatively, for a structure with a well-defined peak, a Gaussian fit with offset will always return a narrower FWHM for a smaller fitting range.

4 SUMMARY

In this work, we have explored the analysis of filament widths in an attempt to find a way to reconcile the proposed 'characteristic' width of filaments with the absence of its imprint in spatial power spectra. Our findings can be summarized in the following points:

(i) The selected methodology for measuring widths can produce a peaked distribution even if the original data do not contain a preferred scale.

(ii) The process of averaging over filament profiles results in a distribution that is necessarily narrow, as a result of the CLT.

(iii) Widths vary significantly as a function of position on the spine of a filament.

(iv) The position of the previously identified peak (0.1 pc) in *Herschel* data could be determined by the choice of distance from the filament spine within which the width is measured.

The above suggests that filaments are unlikely to have a constant width, a result that explains the lack of a characteristic scale in the spatial power spectrum of the Polaris Flare. Finally, we note that our results are specific for the widths of filaments and do not contradict the (well-established) existence of other typical length scales in clouds (Mouschovias 1991).

REFERENCES

Alves de Oliveira C., 2014, A&A, 568, A98
André P. et al., 2010, A&A, 518, L102
André P., Di Francesco J., Ward-Thompson D., Inutsuka S.-I., Pudritz R. E., Pineda J. E., 2014, Protostars and Planets VI, University of Arizona Press, Tucson, AZ, p. 27
André P. et al., 2016, A&A, 592, A54
Arzoumanian D. et al., 2011, A&A, 529, L6
Astropy Collaboration, 2013, A&A, 558, A33
Auddy S., Basu S., Kudoh T., 2016, ApJ, 831, 46
Benedettini M. et al., 2015, MNRAS, 453, 2036
Brockwell P. J., Davis R. A., 2002, in Casella G., Fienberg S., Olkin I., eds, Introduction to Time Series and Forecasting. Springer-Verlag, New York, p. 19
Elia D. et al., 2014, ApJ, 788, 14
Elmegreen B. G., Falgarone E., 1996, ApJ, 471, 816
Elmegreen B. G., Scalo J., 2004, ARA&A, 42, 211
Federrath C., 2016, MNRAS, 457, 375
Fernández-López M. et al., 2014, ApJ, 790, L19
Fischera J., Martin P. G., 2012, A&A, 547, A86
Foreman-Mackey D., 2016, J. Open Source Softw., 1, 2
Foreman-Mackey D., Hogg D. W., Lang D., Goodman J., 2013, PASP, 125, 306
Goodman A. A., Barranco J. A., Wilner D. J., Heyer M. H., 1998, ApJ, 504, 223
Hacar A., Tafalla M., Kauffmann J., Kovács A., 2013, A&A, 554, A55
Hartmann L., 2002, ApJ, 578, 914
Heithausen A., 2002, A&A, 393, 41
Heitsch F., 2013, ApJ, 769, 115
Hennebelle P., 2013, A&A, 556, A153
Hennebelle P., André P., 2013, A&A, 560, A68
Henshaw J. D. et al., 2016, MNRAS, 463, 146
Henshaw J. D. et al., 2017, MNRAS, 464, L31
Juvela M. et al., 2012, A&A, 541, A12
Koch E. W., Rosolowsky E. W., 2015, MNRAS, 452, 3435
Koen C., Kondlo L., 2009, MNRAS, 397, 495
Könyves V. et al., 2015, A&A, 584, 91
Malinen J., Juvela M., Rawlings M. G., Ward-Thompson D., Palmeirim P., André P., 2012, A&A, 544, A50
Miville-Deschênes M.-A. et al., 2010, A&A, 518, L104
Miville-Deschênes M.-A., Duc P.-A., Marleau F., Cuillandre J.-C., Didelon P., Gwyn S., Karabal E., 2016, A&A, 593, 4
Mouschovias T. Ch., 1991, ApJ, 373, 169
Musgrave K., Kolb C. E., Mace R. S., 1989, Comput. Graph., 23, 41
Ntormousi E., Hennebelle P., André P., Masson J., 2016, A&A, 589, 24
Panopoulou G. V., Tassis K., Goldsmith P. F., Heyer M., 2014, MNRAS, 444, 2507
Panopoulou G. V., Psaradaki I., Tassis K., 2016, MNRAS, 462, 1517
Perlin K., 1985, Comput. Graph., 19, 287
Pingel N. M. et al., 2013, ApJ, 779, 36
Planck Collaboration XXXV, 2016, A&A, 586, A138
Polychroni D. et al., 2013, ApJ, 777, L33
Smith R. J., Glover S. C. O., Klessen R. S., 2014, MNRAS, 445, 2900
Sousbie T., 2011, MNRAS, 414, 350
Stutzki J., Bensch F., Heithausen A., Ossenkopf V., Zielinsky M., 1998, A&A, 336, 697
Tassis K., 2007, MNRAS, 382, 1317
Wagle G. A., Troland T. H., Ferland G. J., Abel N. P., 2015, ApJ, 809, 17
Ward-Thompson D. et al., 2010, A&A, 518, L92

APPENDIX A: DISPERSE SKELETONS OF *HERSCHEL* IMAGES

As explained in Section 2, the first step in the analysis of filament widths is the identification of the filaments in the image. This is done here by using DISPERSE (Sousbie 2011) to acquire the skeleton of the image and then using FILTER (Panopoulou et al. 2014) to post-process the skeleton and discard spurious structures.
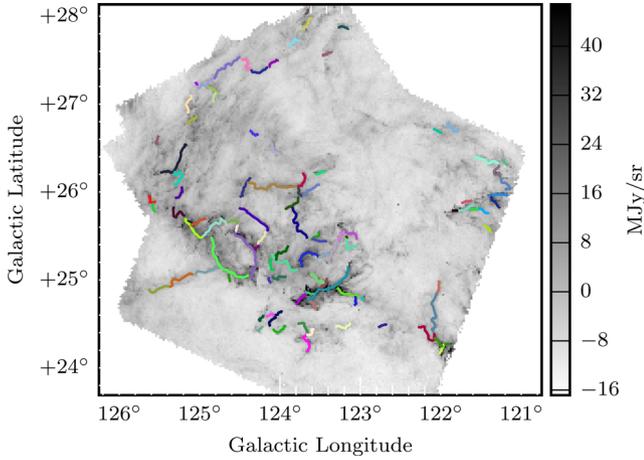
Figure A1. Skeleton of the Polaris Flare 250 μm *Herschel* image constructed with DISPERSE and post-processed with FILTER. Coloured lines trace the spines of filaments used in our analysis.
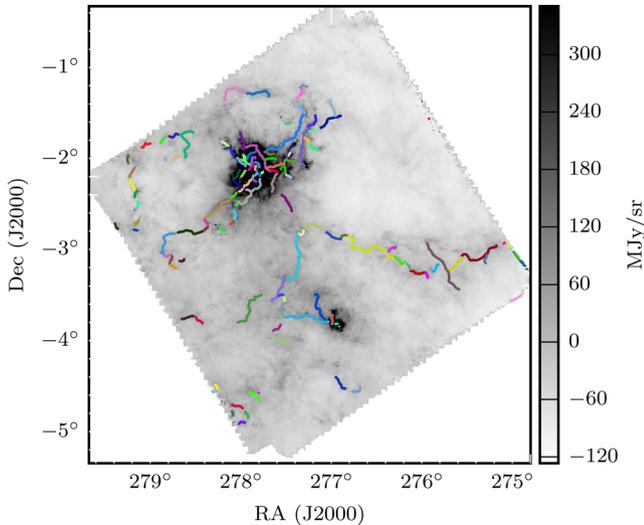
Figure A2. Same as Fig. A1 but for the image of Aquila.

Figure A3. Same as Fig. A1 but for the image of IC 5146. The grey lines divide the image into three sub-maps on which DISPERSE was run separately.

Table A1. Parameters of DISPERSE used for the skeletons of Figs A1–A3.

Cloud	Persistence (MJy sr^{-1})	Robustness (MJy sr^{-1})	Smooth	Assemble (deg)
Polaris Flare	15	16	50	60
Aquila	80	82	50	50
IC 5146 1	400	410	60	90
IC 5146 2	50	51	100	60
IC 5146 3	40	55	100	40

The (post-processed) skeletons of the three clouds (Polaris Flare, Aquila and IC 5146) used in our analysis are shown in Figs A1–A3 (coloured lines) overplotted on the 250 μm *Herschel* images. Each line represents a single structure (filament). The parameters of DISPERSE for these skeletons are shown in Table A1. The skeletons obtained are very similar to those of Arzoumanian et al. (2011), André et al. (2014) and Könyves et al. (2015).

For the Polaris Flare and Aquila, DISPERSE was run directly on the entire (unfiltered) *Herschel* image. The skeleton for IC 5146 was produced by running DISPERSE on three sub-maps (divided by grey lines in Fig. A3) and combining the resulting skeletons. This enabled us to isolate regions of similar intensity, as in the whole map the differences in brightness caused either faint structures not to be identified or spurious structures to be identified in the brightest parts. In Table A1, indices 1, 2 and 3 refer to the left, middle and bottom regions of the map, respectively.

We have performed a parameter study for the skeletons of the image of Aquila to test for effects on the distribution of filament profile widths. The ranges of parameters used (for parameter definitions see Sousbie 2011) were persistence 60–80 MJy sr^{-1}, robustness 82–102 MJy sr^{-1}, smoothing 50–200 and assembling of arcs 50–90 deg. All resulting distributions of profile widths were identical.

APPENDIX B: CAN A CHARACTERISTIC SCALE BE 'HIDDEN' FROM THE POWER SPECTRUM?

In this section, we use simple artificial images to investigate the effect of a characteristic scale on the azimuthally averaged spatial power spectrum of an image.

Our tests consist in creating elongated structures with radial profiles following the form of a Plummer profile in column density (a form that fits well the column density profiles of observed filaments; Arzoumanian et al. 2011). The intensity of the profile of an artificial filament is I_0 on its spine, has an inner flat portion (in logarithmic space) of size R_{flat}, and drops with distance (r) from the axis of the filament as

$$I(r) = \frac{I_0}{[1 + (r/R_{\mathrm{flat}})^2]^{\frac{p-1}{2}}}. \tag{B1}$$

For the exponent, p, we choose a value of $p = 2$, as observed for filaments in *Herschel* data (Arzoumanian et al. 2011).

The artificial filaments have very simplistic characteristics: they are straight, have a constant peak intensity along their spine and a constant R_{flat}. This should make the identification of the signature of any characteristic scale (width, length), in the spatial power spectrum, unambiguous. In this section, we use R_{flat} as a proxy of the width of the artificial filaments as for profiles with $p = 2$, FWHM $\approx 3\,R_{\mathrm{flat}}$ (Arzoumanian et al. 2011).

The filament images are co-added with (the same) two-dimensional isotropic pink noise. We generate the noise by creating the coefficients of its two-dimensional Fourier transform. Each
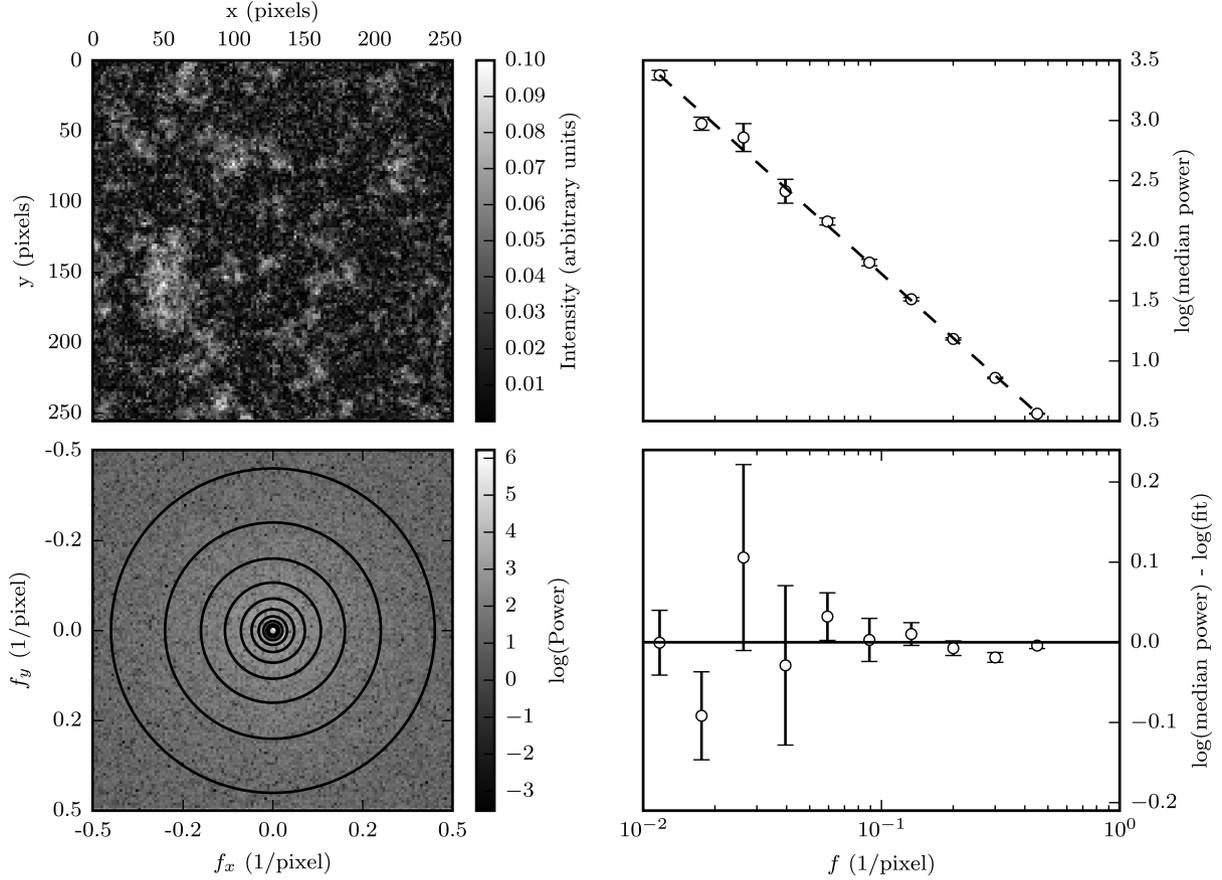
Figure B1. Top left: two-dimensional pink noise that is used in subsequent images of artificial filaments. Bottom left: two-dimensional spatial power spectrum of the image with annuli drawn to indicate the regions within which the azimuthally averaged power spectrum (top right) is calculated. Top right: azimuthally averaged spatial power spectrum with errors and linear fit performed in log–log space (dashed line). Bottom right: difference between the (logarithms of the) spatial power spectrum and the fit.

coefficient C_k has a magnitude of $1/\sqrt{k_x^2 + k_y^2}$ and a random phase (C_0 is set to 0). We obtain the final pink noise image by applying the inverse Fourier transform (Fig. B1, top left). Its two-dimensional power spectrum is shown in the bottom-left panel. The azimuthally averaged power spectrum (constructed by taking the median power within the annuli drawn on the two-dimensional power spectrum, as in Pingel et al. 2013) has the form of a power law (Fig. B1, top right). The deviation from a perfect power law can be quantified by the residuals of the power spectrum from a linear fit in log–log space (dashed line in top right panel). From the bottom-right panel of Fig. B1 we see that the level of the residuals, log(median power)–log(fit), is less than 0.2. As in Section 3.1, the error of the median of each annulus is quantified by bootstrap resampling the distribution of intensities within the annulus.

Fig. B2 (left) shows a single filament that has $R_{\mathrm{flat}} = 8$ pixels and is 80 pixels long. The spatial power spectrum of the image (top right) has been fit by a line. The power spectrum deviates significantly from this line at the spatial frequencies corresponding to R_{flat} (dashed vertical line) and the filament's length (dotted vertical line) as can be seen in the bottom-left panel of the figure.

In Fig. B3, we investigate the effect of changing the width (R_{flat}) of this single filament. As R_{flat} changes from 8 (top) to 12 (middle) and finally to 16 (bottom) pixels, the signature of this scale on the power spectrum moves to the corresponding spatial frequencies (indicated by vertical dashed lines).

Having identified the signature of a characteristic scale on the power spectrum, we now investigate the circumstances under which it may be possible to 'hide' such a signature in a way that it does not appear in the power spectrum. We first create a map with 10 filaments of the same length (40 pixels) but with random orientations and positions. Each filament has a different peak intensity and R_{flat} (constant along its spine). The R_{flat} are drawn from the narrow distribution of mean filament widths found in Fig. 2 (bottom panel). The values drawn from this distribution were multiplied by 100 to obtain R_{flat}, meaning that a value of 0.1 pc is mapped to 10 pixels (a scale that is well sampled in the power spectra of the artificial images). The image is shown in Fig. B4, with each of the vertical dashed lines denoting the spatial frequency that corresponds to $1/R_{\mathrm{flat}}$ for the 10 filaments. Even when multiple filaments are present, with random orientations and spacings between them, the signatures of their characteristic scales are clearly visible as deviations from the fit to the power spectrum. These deviations are significantly larger than those seen in the power spectrum of the pink noise.

We investigate the statistical significance of this result by creating 150 realizations of such images. We find that in only ∼10 per cent of the images, the maximum residual of the fit is less than 0.2 in amplitude (in the range of frequencies corresponding to the values of R_{flat}). However, upon visual inspection, these images can be divided into three categories: (i) the residuals exhibit a systematic offset from the fit, but at a level less than 0.2, (ii) only a single
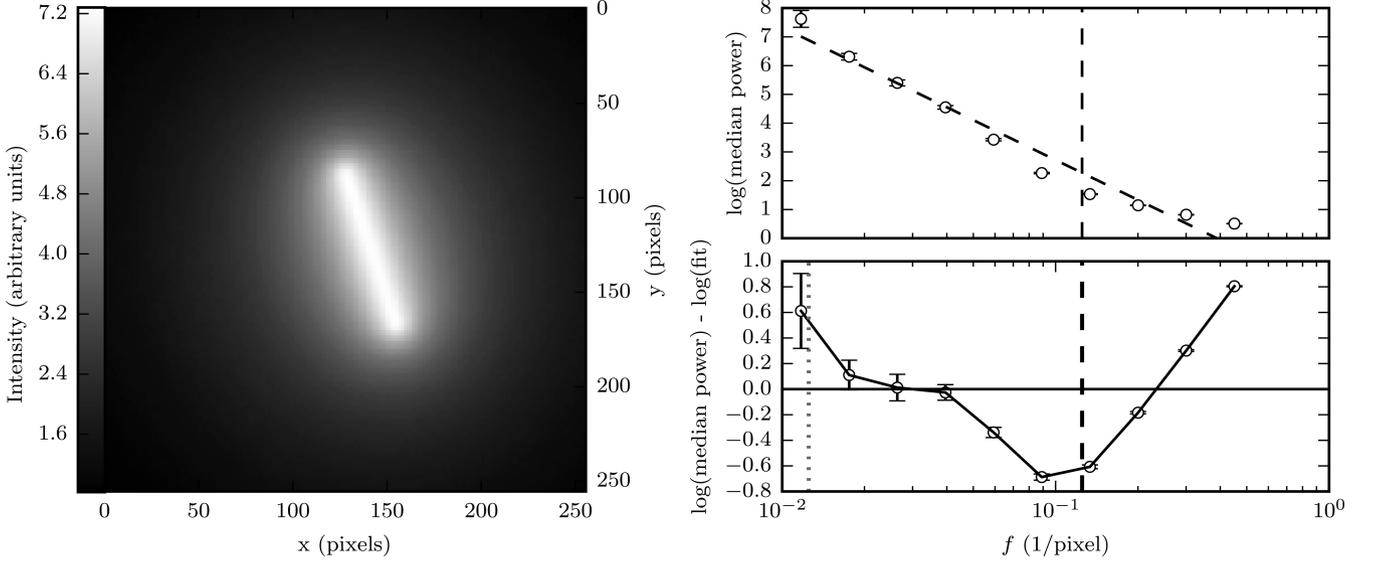
Figure B2. Left: artificial image of a single filament with $R_{flat} = 8$ pixels and length $= 80$ pixels. Top right: spatial power spectrum of the image with a linear fit in log–log space (dashed line). Bottom right: difference between the (logarithms of the) power spectrum and fit. The dashed vertical line shows the spatial scale corresponding to the width R_{flat}, while the dotted line shows the scale corresponding to the length. Low intensity pink noise (Fig B1) has been added to the image of the filament.
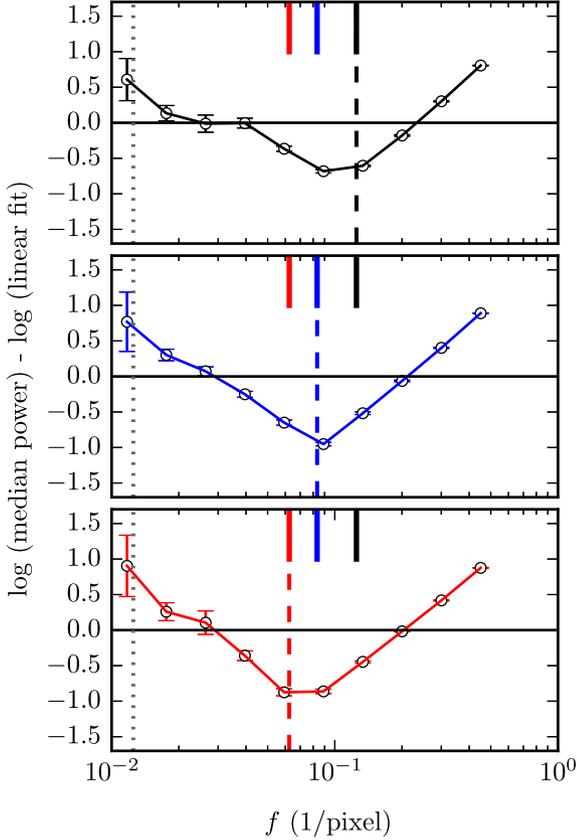
Figure B3. Difference between the spatial power spectrum and a linear fit in log–log space (log(median power)–log(fit)) for an artificial image with a single filament of constant R_{flat}. From top to bottom: $R_{flat} = 8, 12, 16$ pixels. The length is 80 pixels for all three images (dotted vertical line). In each plot, the dashed vertical line shows the spatial frequency that corresponds to R_{flat}. The small vertical lines on the top of each panel show the values of R_{flat}^{-1} of all three images, for comparison between panels.

point in the power spectrum samples the range of scales used or (iii) most filaments overlap at a certain part of the image, so their individual filamentary structure is not visible. In the first case, the systematic offset of neighbouring data points is distinct from the random fluctuation of the residuals in the pink noise image. Thus, a signature of the width is still identifiable in the spatial power spectrum. In the second case, an offset is observed at data points outside but neighbouring to the range considered. In the last case, the imprint of the larger 'cluster' dominates the power spectrum and these images cannot be considered as being comprised of filaments.

Finally, we introduce pink noise with very large amplitude (maximum intensity ~ 30 per cent that of the largest filament spine intensity) in Fig. B5. The filaments in this image are the same as in Fig. B4. Now, the signature of the width (a change of the spectral slope at the corresponding spatial frequency range) is not visible in the residuals of the power spectrum from the fit. However, the filaments are barely distinguishable from the background noise, which is in stark contrast to observations of clouds.

We conclude that the existence of a characteristic scale should appear in the spatial power spectrum of an image (e.g. as a change in the spectral slope), provided that the structure is easily discernible from the background. In the case of the spatial power spectrum of the Polaris Flare (Miville-Deschênes et al. 2010), no such change exists in the power spectrum at or near the spatial scale corresponding to the 'characteristic' width (of the very prominent filaments) at 0.1 pc.

APPENDIX C: ARMA MODELLING OF FILAMENT WIDTHS

In Section 3.2, we saw that the distributions of all profile widths and of filament lengths are necessary but not sufficient pieces of information to explain the spread of the distribution of mean filament widths (σ_{mean}). The goal of this section is to model the variation of widths along the ridge of a filament. Using this information, we will be able to explain quantitatively how one obtains a distribution with σ_{mean} when averaging the widths from the parent distribution of all profile widths.
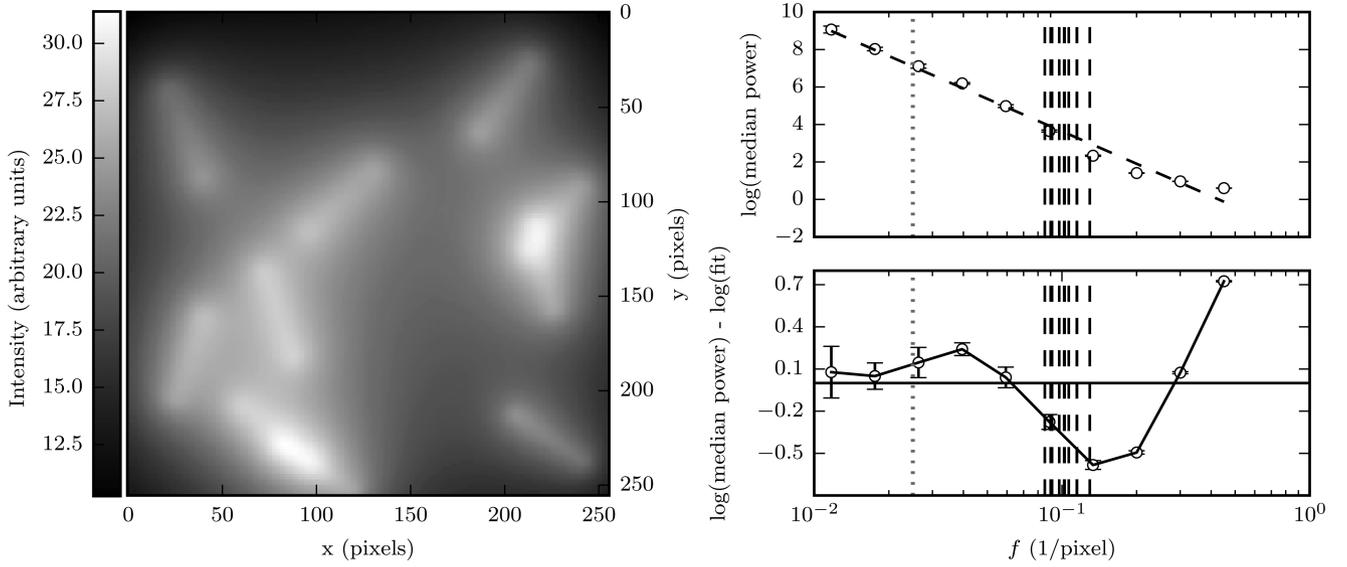
Figure B4. Same as Fig. B2 but for 10 filaments at random orientations, with a length of 40 pixels and different R_{flat}, drawn from the distribution of mean filament widths in Fig. 2 (with values multiplied by 100 so that 0.1 pc is mapped to 10 pixels). The spatial frequency corresponding to the R_{flat} of each of the filaments is shown with a dashed vertical line.
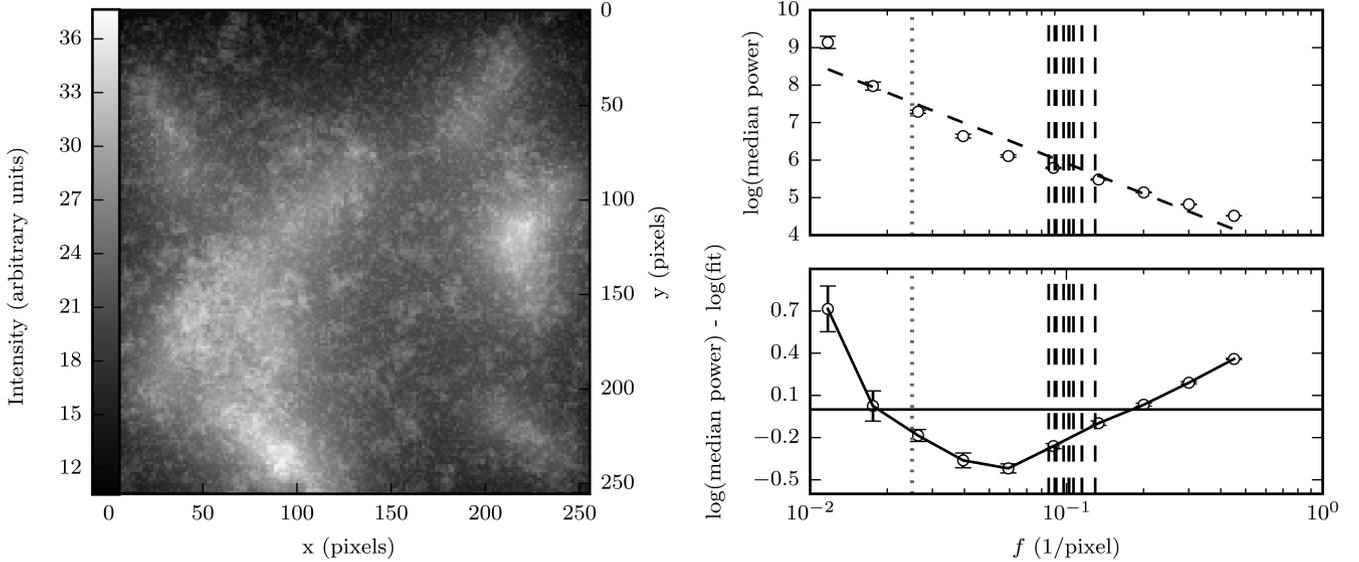
Figure B5. Same as Fig. B4 but with pink noise with maximum intensity ~ 30 per cent that of the highest filament peak.

We choose to model the variation of profile widths along a filament using an Auto-Regressive-Moving-Average (ARMA) process (for a complete description of ARMA modelling, we refer the reader to Brockwell & Davis 2002). Each filament is regarded as a series of N widths, w_i, measured at all positions (pixels), $i = 1$–N, along the filament crest. The difference between the width at point i along the filament crest and the mean width can be written as the regression:

$$\delta w_i = \alpha_0 \delta w_{i-1} + \alpha_1 \delta w_{i-2} + \alpha_2 \delta w_{i-3} + \cdots + \epsilon_i + c_1 \epsilon_{i-1} + \cdots, \tag{C1}$$

where δw_{i-1} is the difference of the width of the point previous to i from the mean width, δw_{i-2} is measured two points away, and so on. Depending on the order p of the auto-regressive (AR) part of the equation (coefficients α), δw_i can have a dependence on the width measured p points away from position i. ϵ_i is the residual, what is not taken into account by the AR terms. It is assumed random and

normally distributed. The terms containing the residuals at different positions are the moving-average terms (MA) and their number q is the order of the MA part of the model.

We wish to model the variation of widths along a filament, based on the data in the Polaris Flare. In order to find an appropriate model, we must first decide on the order of the model to be fit. The order of the ARMA model (p, q) can be determined by examination of the ACF and partial autocorrelation function (PACF) of the widths of filaments in the Polaris Flare for p and q, respectively (Brockwell & Davis 2002).

The ACF is defined as (following Brockwell & Davis 2002)

$$\text{ACF}(l) = \frac{1}{N\sigma_{fil}^2} \sum_{i=1}^{N-l} (w_{i+l} - \langle w \rangle)(w_i - \langle w \rangle),\ 0 < l < N, \tag{C2}$$

where N is the number of profiles in a filament, l is the distance (lag) measured along the filament ridge, w_i is the width of the ith profile
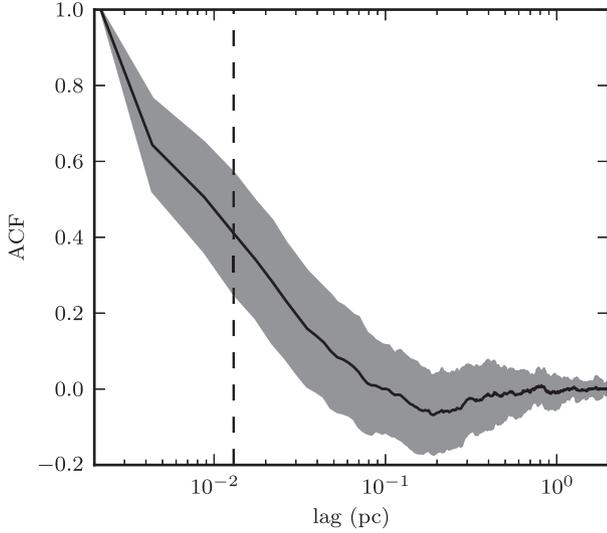
Figure C1. ACF of all filaments in the Polaris Flare versus distance. The black line shows the ACF averaged over all filaments for a given lag (distance). The ± 1 standard deviation of the ACF of all filaments at a given lag is shown with a grey band. The vertical line shows the HPBW (beam size) of 0.013 pc. The plot has been truncated at a distance of 2 pc for clarity.

along the ridge and $\langle w \rangle$ is the average width of the filament. Finally, $\sigma_{\rm fil}$ is the standard deviation of profile widths in the filament. The PACF at a given lag is the autocorrelation at this lag after removal of an AR model of order lag minus 1. This means that the PACF will be zero at this lag if the AR model effectively removes all correlation.

Fig. C1 shows the ACF of widths of all filaments in the Polaris Flare versus distance along the filament ridge.[5] The ACF drops abruptly and stays around zero for distances larger than approximately twice the beam size (HPBW = 0.013 pc, dashed vertical line). For most filaments, widths are strongly correlated only within the beam size. This corresponds to a lag of 3 pixels, and therefore this is the order of the AR process ($p = 3$). The ACF of filaments in IC 5146 and Aquila also follow this trend (for IC 5146 HPBW = 0.04 pc, and for Aquila HPBW = 0.023 pc). In Fig. C2, we plot the PACF of all filaments in the Polaris Flare versus the lag in pc. The PACF (averaged over all filaments for every given lag) drops after a lag of 0.004 pc (1 pixel).

Therefore, the (mean-subtracted) widths along filaments in the Polaris Flare can be modelled with $p = 3$ AR terms and $q = 1$ MA term:

$$\delta w_i = \alpha_0 \delta w_{i-1} + \alpha_1 \delta w_{i-2} + \alpha_2 \delta w_{i-3} + \epsilon_i + c_1 \epsilon_{i-1}. \tag{C3}$$

We fit equation (C3) to the series of widths of each filament in the Polaris Flare. We wish to obtain a single model that on average reproduces well the variation of widths along any filament in the cloud. This model is equation (C3) where the value of each coefficient is equal to the median of values returned by fitting the equation to each filament. The median values of the coefficients from the fits to individual filaments are $\alpha_1 = 0.8, \alpha_2 = 0.2, \alpha_3 = 0.05$ and $c_1 = -0.23$.

As seen in Section 3.2, the observed $\sigma_{\rm mean}$ cannot be explained by only taking into account the distributions of all profile widths and filament lengths. We will now estimate what part of $\sigma_{\rm mean}$ can be attributed to the combined contribution of the correlation between the widths of neighbouring profiles, and the distribution of filament
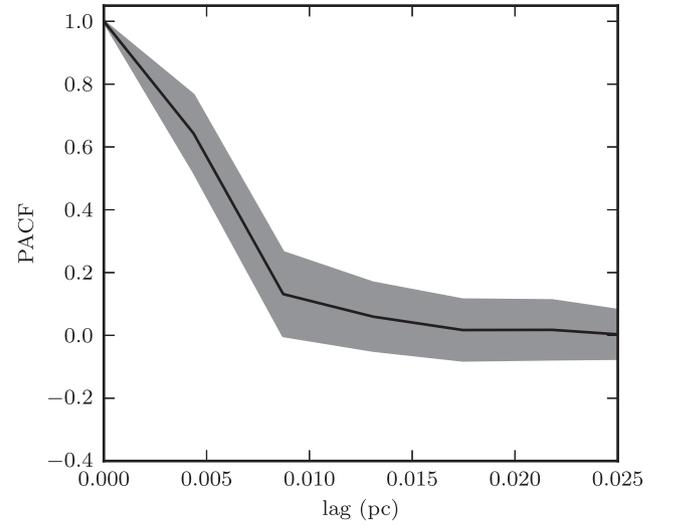
Figure C2. As in Fig. C1 but now showing the PACF of all filaments versus distance. The horizontal axis has been truncated at a distance of 0.025 pc.

lengths. We note that the information on the distribution of all profile widths is included in the ARMA model, as the coefficients were found by fitting to real data.

To this end, we create 100 groups (filaments) of (mean-subtracted) widths in the following way. A number of profiles for each filament are drawn from the distribution of filament lengths in the Polaris Flare. Each filament is assigned a starting value drawn from a normal distribution with mean 0 and standard deviation equal to that of the distribution of ϵ_i from the fits to individual filaments. This starting value corresponds to the mean-subtracted width of the first filament profile. Consecutive (mean-subtracted) profile widths are found iteratively using equation (C3). We then calculate the average width of each filament. The distribution of average filament widths has a spread of 0.011 pc, similar to the observed $\sigma_{\rm mean}$ of 0.014 pc in the cloud. This process is repeated 100 times to quantify whether the difference (0.014 pc versus 0.011 pc) is significant. We find that the observed $\sigma_{\rm mean}$ is within the spread of the results of the simulation.

We have found that $\sigma_{\rm mean}$ can be predicted based on three pieces of information: the distribution of all profile widths, the distribution of filament lengths and the correlation of widths within a beam size. From the CLT, we understand the effect of these three as follows: a broader distribution of all profile widths will increase the uncertainty on the mean ($\sigma_{\rm mean}$), as seen in equation (1). From the same equation, it follows that a population of filaments with on average larger lengths will have a smaller $\sigma_{\rm mean}$. Finally, we have seen that neglecting the effect of the beam (random draws of the width from the parent distribution) produces a narrow $\sigma_{\rm mean}$. The effect of the beam is to introduce a larger uncertainty on the mean, by effectively reducing the number of independent measurements in a single filament.

---

[5] For ARMA modelling and for construction of the ACF, we made use of the python module `statsmodels` (http://statsmodels.sourceforge.net/).

This paper has been typeset from a TEX/LATEX file prepared by the author.

Chapter 3

The magnetic field morphology in a translucent cloud

Apart from the dense molecular clouds ($N(H_2) > 10^{21} - 10^{22} cm^{-2}$) in which stars form, molecular gas also exists in less dense, or translucent clouds ($N(H_2) \sim 10^{20} cm^{-2}$). These translucent clouds, most easily detected at high galactic latitude (where line-of-sight confusion is minimal compared to sightlines along the galactic disk), were largely unmapped territory in terms of the magnetic field, prior to the Planck all-sky mission. However, due to their low resolution (0.5 sq.deg), the Planck data can not offer a complete picture of the field morphology at scales comparable to cloud structures (e.g. filaments). At such scales, the magnetic field structure can be probed by starlight polarization, exploiting the fact that the extinction is low enough for many stars to be observable. We explored this poorly studied column density regime using optical polarimetry in the following work. We used the RoboPol polarimeter at the Skinakas observatory to map the magnetic field of the Polaris Flare translucent cloud. Since this was the first use of the instrument for polarization measurements throughout the field of view, we developed a set of tools to control wide-field systematics. We incorporated these developments in the existing data processing pipeline after thorough testing. The resulting optical polarization map was presented in this work and was made public. During subsequent work, we discovered an error in an astrometric conversion adopted in a previous study, which affected a small subset of the measurements as presented in the original paper. The correction to the formula and polarization measurements (angles) were presented in an erratum.

Optical polarization map of the Polaris Flare with RoboPol

G. Panopoulou,[1,2]★ K. Tassis,[1,2] D. Blinov,[1,3] V. Pavlidou,[1,2] O. G. King,[4]
E. Paleologou,[1] A. Ramaprakash,[5] E. Angelakis,[6] M. Baloković,[4] H. K. Das,[5]
R. Feiler,[7] T. Hovatta,[4,8] P. Khodade,[5] S. Kiehlmann,[6] A. Kus,[7] N. Kylafis,[1,2]
I. Liodakis,[1] A. Mahabal,[4] D. Modi,[5] I. Myserlis,[6] I. Papadakis,[1,2]
I. Papamastorakis,[1,2] B. Pazderska,[7] E. Pazderski,[7] T. J. Pearson,[4]
C. Rajarshi,[5] A. C. S. Readhead,[4] P. Reig[1,2] and J. A. Zensus[6]

[1]*Department of Physics and ICTP†, University of Crete, GR-71003 Heraklion, Greece*
[2]*Foundation for Research and Technology - Hellas, IESL, Voutes, GR-7110 Heraklion, Greece*
[3]*Astronomical Institute, St Petersburg State University, Universitetsky pr. 28, Petrodvoretz, 198504 St Petersburg, Russia*
[4]*Cahill Center for Astronomy and Astrophysics, California Institute of Technology, 1200 E California Blvd, MC 249-17, Pasadena, CA 91125, USA*
[5]*Inter-University Centre for Astronomy and Astrophysics, Post Bag 4, Ganeshkhind, Pune 411 007, India*
[6]*Max-Planck-Institut für Radioastronomie, Auf dem Hügel 69, D-53121 Bonn, Germany*
[7]*Toruń Centre for Astronomy, Nicolaus Copernicus University, Faculty of Physics, Astronomy and Informatics, Grudziadzka 5, PL-87-100 Toruń, Poland*
[8]*Metsähovi Radio Observatory, Aalto University, Metsähovintie 114, FI-02540 Kylmälä, Finland*

ABSTRACT

The stages before the formation of stars in molecular clouds are poorly understood. Insights can be gained by studying the properties of quiescent clouds, such as their magnetic field structure. The plane-of-the-sky orientation of the field can be traced by polarized starlight. We present the first extended, wide-field ($\sim$10 deg^2) map of the Polaris Flare cloud in dust-absorption induced optical polarization of background stars, using the Robotic Polarimeter (RoboPol) polarimeter at the Skinakas Observatory. This is the first application of the wide-field imaging capabilities of RoboPol. The data were taken in the *R* band and analysed with the automated reduction pipeline of the instrument. We present in detail optimizations in the reduction pipeline specific to wide-field observations. Our analysis resulted in reliable measurements of 641 stars with median fractional linear polarization 1.3 per cent. The projected magnetic field shows a large-scale ordered pattern. At high longitudes it appears to align with faint striations seen in the *Herschel*-Spectral and Photometric Imaging Receiver (SPIRE) map of dust emission (250 μm), while in the central 4–5 deg^2 it shows an eddy-like feature. The overall polarization pattern we obtain is in good agreement with large-scale measurements by *Planck* of the dust emission polarization in the same area of the sky.

Key words: magnetic fields – polarization – stars: formation – ISM: clouds – ISM: individual objects: Polaris Flare.

1 INTRODUCTION

Molecular clouds in their vast complexity hold the key to understanding the early stages of the star formation process. Magnetic fields and turbulence are the two main mechanisms that dictate the structural, dynamical and evolutionary properties of these clouds,

through their competition against gravity. Their role in the onset of star formation can be studied best in quiescent non-star-forming regions, where stellar feedback is not present. One such region is the Polaris Flare, a translucent high-latitude molecular cloud first observed by Heiles (1984). Estimates of the cloud's distance vary from 130–240 pc (Heithausen et al. 1993) to 380 ± 40 pc (Schlafly et al. 2014). It is believed to be in the early stages of its formation, since it does not exhibit any signs of active star formation (Ward-Thompson et al. 2010). CO observations have provided invaluable information on the turbulence signatures in the densest parts of the cloud (Falgarone et al. 1998; Hily-Blant & Falgarone 2009). The

Herschel space telescope mapped over 15 deg^2 of the cloud in dust emission as part of the *Herschel* Gould Belt Survey (André et al. 2010; Miville-Deschênes et al. 2010).

The structure of the magnetic field of a cloud, as projected on the plane of the sky, can be probed by observing polarized radiation. The polarization of starlight transmitted through a cloud is believed to be caused by dichroic extinction due to aspherical dust grains that are partially aligned with the magnetic field. This alignment causes the polarization direction of the light of background stars to trace the magnetic field direction of the cloud as projected on the plane of the sky. The same alignment process causes the thermal emission of these dust grains to be polarized in the direction perpendicular to the magnetic field.

Information on the plane-of-the-sky magnetic field of the Polaris Flare was recently provided for the first time through polarized dust emission (Planck collaboration XIX 2015; Planck collaboration XX 2015). These data, however, are limited by the instrumental resolution and confusion along the line of sight. A mapping of the region in polarized starlight, which is complementary to the dust emission but suffers from different limitations, is necessary to resolve these issues.

We obtained optical polarization measurements of stars projected on 10 deg^2 of the Polaris Flare region with Robotic Polarimeter (RoboPol). The RoboPol instrument is a four-channel optical polarimeter with no moving parts, other than a filter wheel (Ramaprakash et al., in preparation). It can measure both linear fractional Stokes parameters $q = Q/I$ and $u = U/I$ simultaneously, thus avoiding errors caused by the imperfect alignment of rotating optical elements and sky changes between measurements (polarization, seeing conditions).

Each star in the field of view creates four images (spots) on the CCD displaced symmetrically in the horizontal and vertical directions. A mask supported by four legs is positioned at the centre of the field of view. This allows targets that are centred on the mask to be measured with four times lower sky noise than the rest of the field. A typical image seen with RoboPol is shown in Fig. 1. The instrument has a 13 arcmin × 13 arcmin field of view, enabling
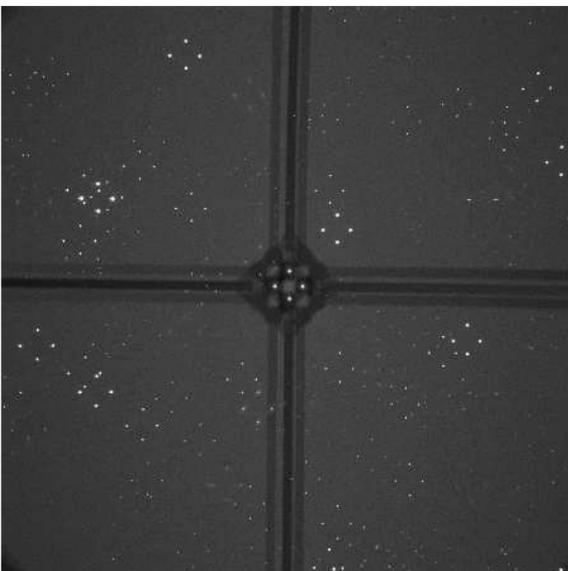
Figure 1. A field observed by RoboPol. Each star in the field creates a quadruplet of images (spots) on the CCD. The central dark region is the mask used for lowering sky noise for the target at the centre of the field of view and the cross-like figure is created by the mask-supporting legs.

the rapid polarimetric mapping of large areas of the sky. RoboPol is equipped with standard Johnson–Cousins *R*- and *I*-band filters and is mounted on the 1.3-m, *f*/7.7 Ritchey–Crétien telescope at Skinakas Observatory in Crete, Greece. It has been operating since 2013 May.

RoboPol has been monitoring the optical linear polarization of a large sample of gamma-ray bright blazars for the past two years (Pavlidou et al. 2014). In addition, the instrument is being used for long-term monitoring of Be X-ray binaries (Reig et al. 2014). Observations of optical afterglows of gamma-ray bursts have also been conducted with RoboPol (King et al. 2014). More complete descriptions of the instrument and data reduction pipeline are given in Ramaprakash et al. (in preparation) and King et al. (2014), respectively.

The data presented here are the first obtained from an analysis of the instrument's entire field of view. We present the observational details in Section 2. In Section 3, we describe the methods used for analysing sources in the entire field of view. We present and discuss the results of our observations in Section 4 and summarize our findings in Section 5.

2 OBSERVATIONS

Polarimetric observations were taken during 25 nights from 2013 August to November, totalling around 60 h of telescope time. The observations covered an area of 10 deg^2: $l = [122\overset{\circ}{.}6, 126\overset{\circ}{.}0]$, $b = [24\overset{\circ}{.}7, 27\overset{\circ}{.}9]$. The area was initially divided into 275 non-overlapping fields spaced 13.2 arcmin apart (slightly larger than the size of the RoboPol field of view). Of them, 227 were observed by the end of the period. The number of observations of each field ranges between 2 and 6, with 93 per cent of all fields having been observed at least three times. 95 per cent of the exposures were 180 s long, while the remaining were 120 s long. All observations were taken in the *R* band.

3 ANALYSIS

Previous studies with RoboPol concentrated on sources either exclusively within the mask, or with the addition of some selected sources in the field of view around the central target. Although the data reduction pipeline presented by King et al. (2014) was designed for the entire RoboPol field of view, its implementation in this particular project showed the need for some adjustments and additions. Sources outside the mask present a number of challenges. Some are common in most polarimetric studies in the optical, while others are due to the particular design of the instrument. A measurement may be adversely affected by one of the following sources of systematic error:

  (i) large-scale optical aberrations,
  (ii) proximity to the mask and its legs,
  (iii) proximity to the CCD edge,
  (iv) proximity to other sources,
  (v) selection of apertures for photometry,
  (vi) dust on optical elements.

An additional systematic error has already been identified and discussed by King et al. (2014). A rotation in the polarization reference frame of the telescope with respect to that of the sky causes all angles to be larger by $2\overset{\circ}{.}31 \pm 0\overset{\circ}{.}34$. All polarization angle measurements presented in this paper have been corrected for this.

This section outlines the analysis of observations and the methodology adopted to control these systematic effects.

3.1 Significance of measurements and debiasing

The measurement of the fractional linear polarization (p) at the low-polarization regime which is relevant for interstellar polarization, being always positive, is biased towards values larger than the true (intrinsic) polarization (Simmons & Stewart 1985). Thus, p measurements should be debiased to find their most probable intrinsic value. In the analysis, we consider only sources with signal-to-noise ratios ($p/\sigma_p \geq 2.5$) so that errors are approximately normally distributed. The maximum-likelihood estimator of the true value of p found by Vaillancourt (2006) for measurements with $p/\sigma_p \geq 3$ significance is

$$p_d = \sqrt{p^2 - \sigma_p^2}. \tag{1}$$

We extend this formula to $p/\sigma_p \geq 2.5$ and use it to debias all measurements of p.

3.2 Large-scale optical aberrations

Large-scale aberrations caused by the optical system are corrected by the instrument model, as presented by King et al. (2014). The model is created by placing an unpolarized standard star at many positions across the field of view and finding the best-fitting parameters that cancel the global, instrumentally induced polarization and vignetting.

The instrument model has been found to perform equally well, regardless of telescope pointing position (which may result in different telescope stresses) and after multiple removals and re-installations of the instrument on the telescope. The set of models that were created for these tests have been combined into one with improved performance with respect to that presented by King et al. (2014). Below we estimate the systematic uncertainty that remains after the model correction.

3.2.1 Systematic uncertainty from model residuals

Fig. 2 shows the uncorrected (left) and corrected (right) q (top) and u (bottom) values across the CCD derived by using this combined model. The data are binned in 100 cells of 39 arcsec width and the mean value is plotted in each one. On average, 2.4 star measurements contribute to each cell. The residuals appear to be homogeneous across the CCD.

The distributions of residual q and u of the combined model are shown in Fig. 3. Vertical lines show the standard deviation of each distribution ($\sigma_{q,\text{res}} = 0.0034$, $\sigma_{u,\text{res}} = 0.0031$). Statistical errors of measurements of unpolarized standards are an order of magnitude lower than these standard deviations, thus their contribution to this scatter can be ignored. Therefore, we take the systematic uncertainties in q and u to be $\sigma_{q,\text{sys}} = \sigma_{q,\text{res}}$, $\sigma_{u,\text{sys}} = \sigma_{u,\text{res}}$.

From now on, in order to estimate total uncertainties in q and u, we add statistical and systematic uncertainties in quadrature,

$$\sigma_q^2 = \sigma_{q,\text{sys}}^2 + \sigma_{q,\text{stat}}^2 \tag{2}$$

$$\sigma_u^2 = \sigma_{u,\text{sys}}^2 + \sigma_{u,\text{stat}}^2. \tag{3}$$

The total uncertainty in q and u can be propagated to find the total uncertainty in fractional linear polarization (p) and electric vector position angles (EVPA or χ) using the following equations:

$$p = \sqrt{q^2 + u^2}, \quad \sigma_p = \sqrt{\frac{q^2\sigma_q^2 + u^2\sigma_u^2}{q^2 + u^2}} \tag{4}$$
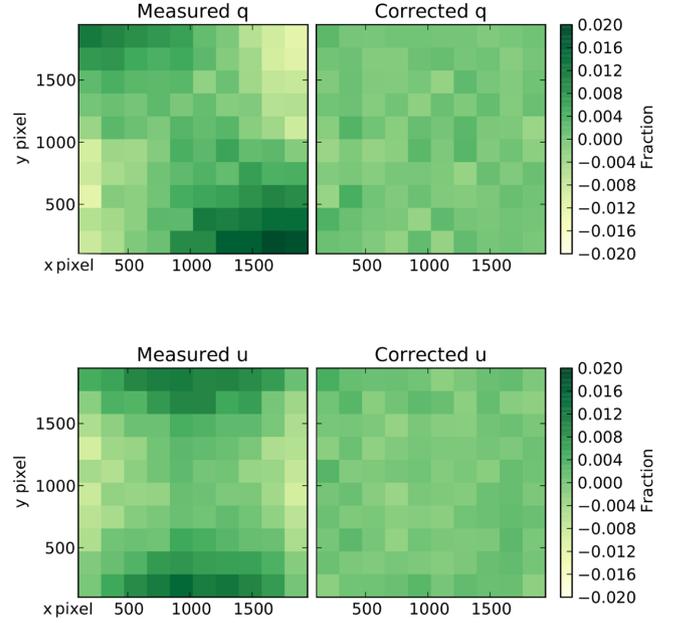
Figure 2. Relative Stokes parameters across the CCD. Left: measured q (top) and u (bottom). Right: residual q (top) and u (bottom) after subtracting the fitted model. Each square panel shows values on the CCD binned in 100 cells. Each cell is coloured according to its average value.
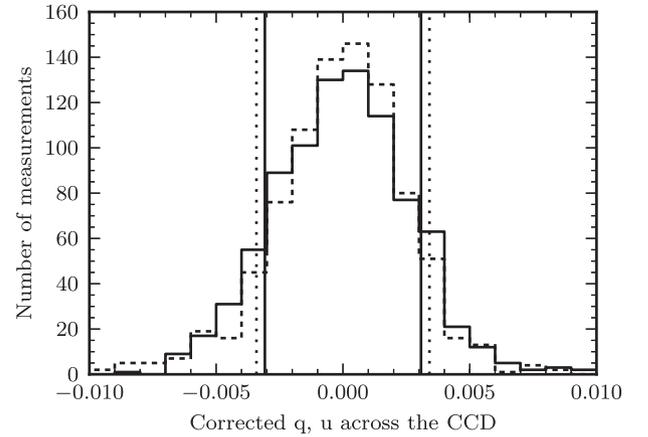
Figure 3. Distributions of the residuals of q and u across the CCD, after the subtraction of the model fit (q: dotted, u: solid). The vertical lines show the standard deviation of each distribution.

$$\chi = \frac{1}{2}\tan^{-1}\frac{u}{q}, \quad \sigma_\chi = \frac{1}{2}\sqrt{\frac{u^2\sigma_q^2 + q^2\sigma_u^2}{(q^2 + u^2)^2}}. \tag{5}$$

Assuming low polarization the expression for $\sigma_{\chi,\text{sys}}$ can be written as

$$\sigma_\chi \simeq \frac{1}{2}\frac{\sigma_p}{p}. \tag{6}$$

3.2.2 Performance: standard stars

To assess the accuracy of the instrument model, measurements of stars with known polarization values were taken and were then compared to the literature. During the two observing seasons, a

Table 1. Polarization standard stars shown in Fig. 4.

	BD+59.389	VICyg12	HD151406	HD212311
P (per cent)	6.430 ± 0.022	7.893 ± 0.037	0.085 ± 0.041	0.034 ± 0.021
	6.43 ± 0.13	7.18 ± 0.04		0.02 ± 0.021
				0.045
$\chi(°)$	98.14 ± 0.10	116.23 ± 0.14	-2	50.99
	96.0 ± 0.6	117 ± 1		36.2 ± 51.3
				10.4
Band	R	R	No filter	V
Reference	1, 5	1, 3	2	1, 4, 5

Notes. 1 – Schmidt, Elston & Lupie (1992), 2 – Berdyugin, Piirola & Teerikorpi (2014),
3 – Bailey & Hough (1982), 4 – Heiles 2000, 5 – Eswaraiah et al. (2011).
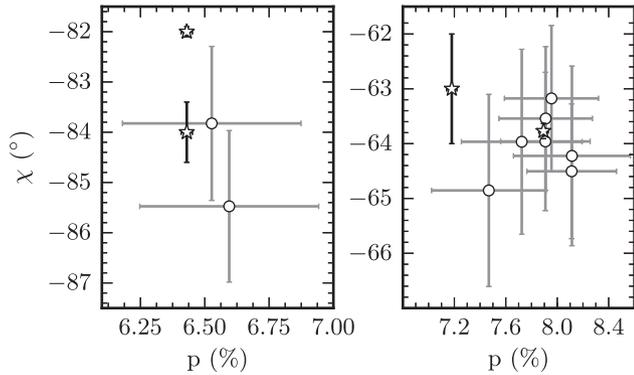
Figure 4. EVPA versus fractional linear polarization of standard stars. Left: BD+59.389, right: VI Cyg12. Literature values are shown by stars (see references in Table 1) and circles are measurements outside the mask. Error bars include the statistical and systematic uncertainties added in quadrature.

Figure 5. Probability distribution of the intrinsic value of p of unpolarized standards, given the measurement in the literature (red) and our own (black). Left: HD151406, right: HD212311. There are two black lines (measurements) of HD212311.

number of standard stars (different from the ones used for the model calculation) were observed throughout the field of view. Catalogue measurements as well as the band in which they were taken are shown in Table 1. Measurements of the unpolarized stars in the R band could not be found, so those in other bands are quoted.

Fig. 4 presents RoboPol measurements of polarized standards (denoted by circles) and their literature values (stars) on the EVPA–polarization fraction plane. All p measurements are consistent with the literature within the errors (which include both the statistical and systematic uncertainties discussed above). Measurements of p have not been debiased.

In the case of unpolarized stars, biasing of p measurements is very pronounced and the interpretation of the measurement uncertainty is not straightforward. To facilitate comparison of our measurements with literature values, we plot, in Fig. 5, the probability distribution (likelihood) of the intrinsic (true) value of p, given the literature measurement (red) and our own (black). This likelihood function (see Vaillancourt 2006, equation 8) takes into account that the measured values of p follow a Rice, rather than a normal, distribution. In calculating the likelihood function, we have used a total uncertainty obtained by adding statistical and systematic uncertainties in quadrature, as in equations (2) and (3). In both cases, our measurements are consistent within uncertainties with the literature measurements. There are two measurements (black lines) of the standard HD212311. For unpolarized standards the EVPA does not carry meaningful information, as can be seen by substituting $\sigma_p/p > 1$ into equation (5): $\sigma_\chi \geq 30°$.

3.3 Proximity to the mask, legs and CCD edge

The mask and its supporting legs cast shadows on specific regions of the CCD rendering them unusable. Therefore, sources that happen to fall in the shadow of the mask legs or within 155 pixels (radially) of the mask centre are not considered in the analysis.

Sources falling very close to any of the CCD edges are very likely to suffer partial photon losses. Also, light reaching these areas is subject to large optical distortions. Since the typical separation between a pair of the four images is 100 pixels, we reject any spot within 100 pixels of the edges from the analysis.

3.4 Proximity to other sources

Sometimes images from different stars happen to fall within a few pixels of each other on the CCD. Since the typical diameter of a spot is 8 pixels (3.2 arcsec), photons from both spots are blended, as shown in Fig. 6. The relative Stokes parameters are computed using the following equations:

$$q = \frac{N_1 - N_0}{N_1 + N_0}, \quad \sigma_q = \sqrt{\frac{4(N_1^2 \sigma_0^2 + N_0^2 \sigma_1^2)}{(N_0 + N_1)^4}} \tag{7}$$

$$u = \frac{N_3 - N_2}{N_3 + N_2}, \quad \sigma_u = \sqrt{\frac{4(N_3^2 \sigma_2^2 + N_2^2 \sigma_3^2)}{(N_2 + N_3)^4}}, \tag{8}$$

where N_i is the number of photons in the ith spot and σ_i is the uncertainty that results from the photon noise. Therefore, overlapping of spots causes an artificially large difference in intensity of one pair
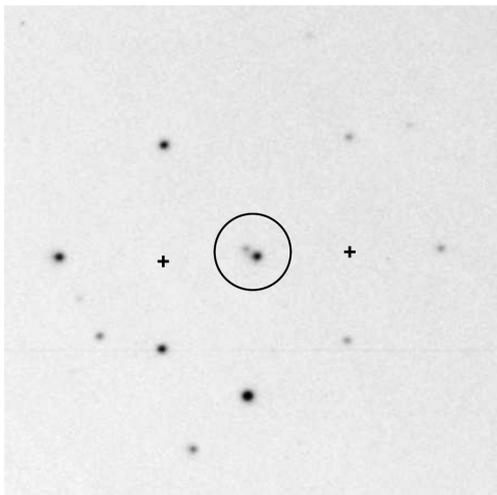
Figure 6. An example of sources that are affecting each other's measurements due to their proximity (circled spots). The positions of these stars (centres of quadruplets) are shown with crosses.

Figure 8. Distributions of ratios of the FWHM between vertical (black) and horizontal (red) spots for a number of fields. Vertical lines mark the area that contains acceptable ratios.

of spots belonging to each affected star. The two the point spread functions (PSFs) cannot be de-blended, since the pipeline performs aperture photometry. Typically, this contamination results in erroneously large degrees of polarization (but not necessarily, this can vary based on the relative brightness of the sources involved) and, most notably, regular EVPAs ($0°$, $±45°$, $±90°$). This follows from the definition of the EVPA, equation (5). If one of the vertical images of the star is artificially brightened, for example $N_1 \ll N_0$, then $|u| \ll |q| \Rightarrow \chi \to 0°$, $±90°$. Whereas if one of the horizontal images is affected by a nearby source, e.g. $N_2 \ll N_3$, then $|q| \ll |u| \Rightarrow \chi \to ±45°$. Fig 7 (left) shows the EVPA versus fractional linear polarization of all sources with at least two measurements found in the Polaris Flare field (5172 in total). Measurements of $p > 20$ per cent are clustered around regular EVPAs – the clear signature of nearby star contamination.

We remove such sources from the analysis in the following way. If any of the four spots of a star suffers from confusion with another spot then we flag it as nearby contaminated. This flag applies if a source exists within three times FWHM (full width at half-maximum) of a star spot. In cases where the spots of two stars

happen to fall exactly on each other and are identified as a single source we check if any spot is assigned to more than one star. The effect of removing contaminated sources from the final catalogue can be seen in Fig. 7 (right). All but two measurements with $p > 20$ per cent were caused by proximity to other sources.

Stars that are affected by reflections, and even other close-by stars in the case that the previous check fails, can be removed by checking the ratio of the FWHM between two pairs of spots. The distribution of these ratios for all stars found in all observed frames is shown in Fig. 8. We discard measurements lying outside the range 0.87–1.15 (vertical lines).

3.5 Aperture optimization

The RoboPol pipeline performs aperture photometry to measure the intensity (photon counts – N) of each spot. It then uses these values to calculate the Stokes parameters as shown in equations (7) and (8). Photometry measurements are greatly affected by the choice of aperture size (e.g. Howell 1989). If the aperture is too large the value obtained suffers from background contamination and the signal-to-noise ratio is decreased. On the other hand, if the

Figure 7. Fractional linear polarization versus EVPA for stars in the Polaris Flare field. Left: measurements at regular angles ($0°$, $±45°$, $±90°$) are caused by nearby contamination as seen in Fig. 6. Right: measurements that survive after the removal of stars that suffered this contamination. Most remaining measurements of $p > 5$ per cent are caused by other systematics.

aperture is too small only a fraction of the total flux is measured. This is not a problem if the same fraction of photons are counted, since polarimetric measurements depend on the relative brightness of two spots. If, however, the PSFs of two spots belonging to a source are different, then the fraction of the total flux measured is not the same and this introduces artificial polarization.

A number of circumstances may affect the PSF of the four spots of a source. Bad seeing or weather conditions (wind) sometimes cause sources to appear elongated instead of round. Also, the optical system of the instrument may distort the shape of the PSF and mainly the wings of the profile. Typically, bright stars (whose wings are more prominent) are affected more severely than faint ones. Therefore, it is essential that photometry be performed with an aperture optimized for each source. Also, the complexity of the optical system introduces some asymmetries in the PSFs of the vertical and horizontal images of a star. Consequently, photometry must also be optimized for *each* of the four images of a star.

We created a simple aperture optimization algorithm as an addition to the original pipeline, presented in King et al. (2014). Photon counts are measured within a circular aperture centred on each spot, while the background level is estimated within an outer concentric annulus that is separated from the inner aperture by a gap. The diameter of the background annulus is a constant multiple of the aperture size. The constant is different for faint and bright sources as the latter have more extended wings, so that the annulus does not contain any light from the source while retaining the smallest possible distance from the source for the background estimation.

By measuring the background-subtracted photon flux within increasing apertures we create a growth curve for each spot. Each of the four growth curves of the source are fitted with a fourth-degree polynomial, $P(x)$ (no errors are accounted for in the fit). The size of the aperture at which the normalized photon flux saturates is the optimum. To locate it in practice we look for the aperture size at which the rate of photon flux increase has reached some small value λ. In other words, the optimal aperture is the root of the equation:

$$\frac{\mathrm{d}P}{\mathrm{d}x} = \lambda P(x). \tag{9}$$

An example growth curve of one of the images of a star is shown in Fig. 9 (circles) along with its polynomial fit (solid line). The dashed vertical line shows the optimal aperture found by solving equation (9). This aperture is used to measure the photon counts and noise (N, σ) of this spot. The optimization is used for all data, including those collected for the instrument model calculation.

3.5.1 The choice of the value for λ

To calibrate equation (9) and determine the best value of λ, we created growth curves of polarization standard stars that were routinely observed in the field and measured their fractional linear polarizations and angles using all the different aperture sizes. Fig. 10 shows the fractional linear polarization (top) and EVPA (middle) measured for VI Cyg12 with different apertures. As the aperture increases, these quantities saturate at some value consistent with those found in the literature (grey bands). As aperture size continues to increase, the signal-to-noise ratio worsens and also nearby sources may affect the measurement. The point on the horizontal axis after which saturation occurs is the optimal aperture for this star. The parameter λ was selected so that it reflects this transition. The bottom panel of Fig. 10 shows the four growth curves of VI Cyg12 and the corresponding polynomial fits. The vertical line shows the aperture that was chosen as optimal.
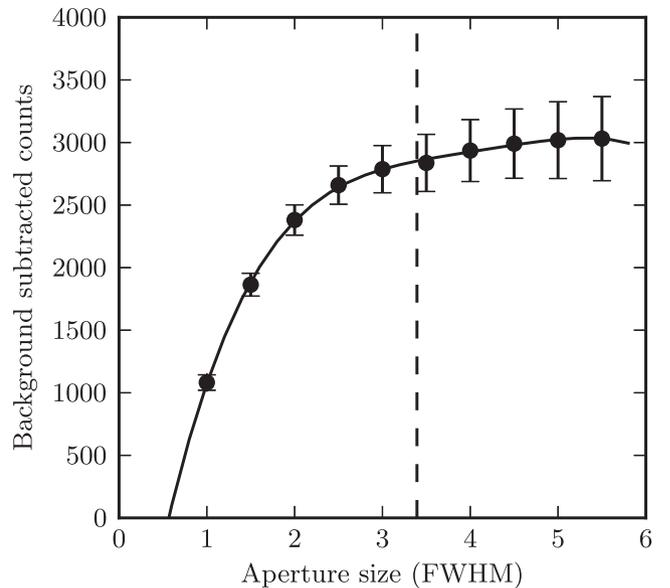
Figure 9. Growth curve of one of the images of a star (circles show the number of background-subtracted counts for each aperture size). A fourth-degree polynomial is fit to the points. The optimal aperture is shown with the dashed line.
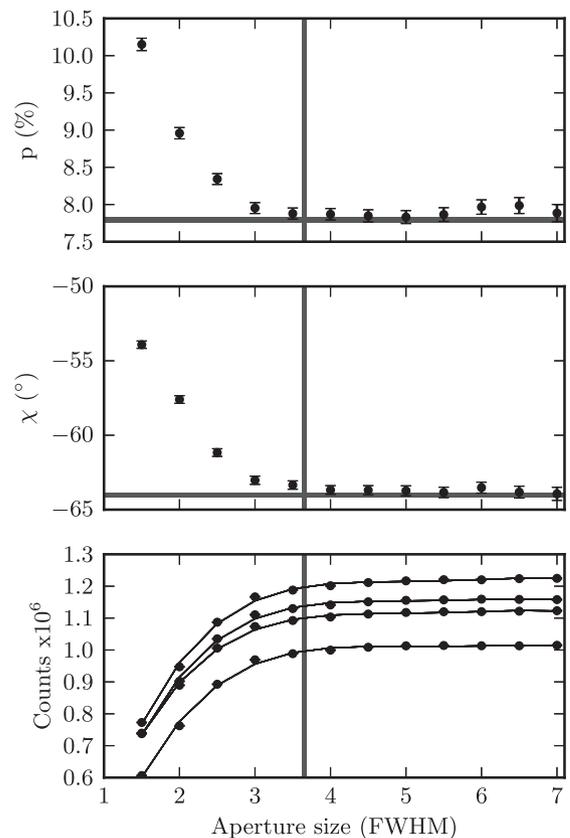
Figure 10. Top: fractional linear polarization of the standard star VI Cyg12 measured with different aperture sizes (multiples of FWHM). The horizontal grey band shows the literature value $\pm 1\sigma$. The position of the vertical grey band shows the mean of the four optimal apertures while its width represents their scatter. Middle: EVPA measured with different aperture sizes. Bottom: background-subtracted number of counts with different aperture sizes (growth curve). The growth curves for all four of images of the star are shown, along with a fourth-degree polynomial fit.
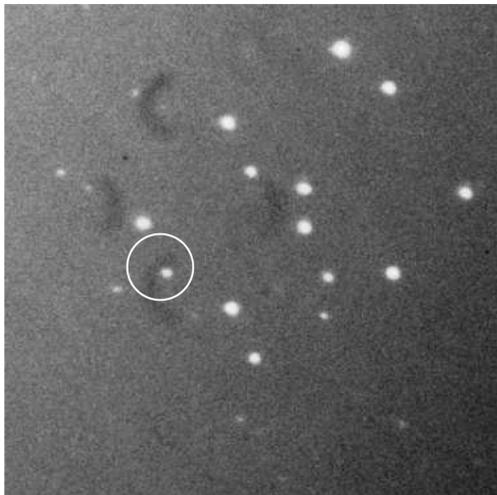
Figure 11. Crescent dust patterns on the CCD. One of the four images of a star falls on a dust pattern (in the white circle).

Because the standards observed with RoboPol are bright (typically 9–11 mag) we needed to extend this sample to stars of lower brightness. We selected six stars that were already observed in the field and observed them in the mask. We used the values found in the mask to define the optimal aperture for these sources when observed in the field. Finally, we optimized the parameter λ so that it yields an accurate optimal aperture for most of the stars (both these six as well as the standards): λ = 0.02.

3.6 Detection of dust specks using flat-field images

The design of RoboPol does not allow us to correct science images for irregularities in transmission and uneven sensitivity throughout the field in conventional ways (e.g. by dividing pixel-by-pixel by a flat-field image). Because both sets of orthogonally polarized beams are projected on the same CCD, when recording an extended image (such as a flat) each point on the CCD is exposed to four rays tracing four different optical paths through the instrument. In contrast, the photon counts we would like to correct (i.e. each of the four images corresponding to a point source) arrive on the CCD through a single optical path since each beam corresponds to a different orientation of the plane of polarization. Light from the sky against which they are projected still arrives through four paths for each pixel, but at different ratios, since the polarization of the sky differs between the moments of science and flat-field image acquisition. This makes ordinary flat fielding impossible.

The global non-uniformity of the field (caused by vignetting) is corrected by the instrument model as described in Section 3.2.2. Small-scale non-uniformities cannot be corrected for, but they can be identified on flat-field images. Stars that happen to be affected by these small-scale variations must be excluded from the analysis. An example is shown in Fig. 11 where the crescent pattern produced by a dust speck is clearly visible in the exposure and coincides with one of the four spots of a star (circled in white).

We process flat-field images obtained in the evening and/or the morning of each night in the following way: we create a master flat by normalizing separate shots and taking the median. After that we fit a third-degree polynomial to the master flat and subtract its value from each pixel, thus removing the large-scale vignetting in the flat image.
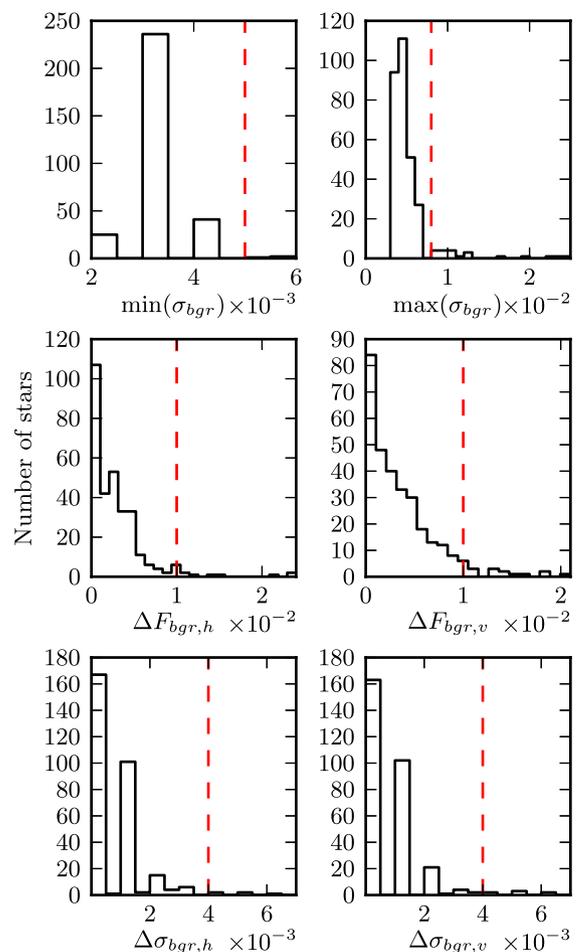
Figure 12. Distributions of the values extracted from the flat-fields and used for identifying dust specks. Values on the horizontal axis are measured in normalized counts.

At the position of each spot in the science image, we calculate the mode value (F_{bgr}) and standard deviation of counts (σ_{bgr}) of pixels on the flat-field image that fall within an aperture with diameter equal to the background annulus. In principle, by comparing these quantities on all four spots of a star we can determine whether any of them has fallen on a dust speck, since this would cause significant variations in F_{bgr} and σ_{bgr}.

To establish a set of reliable criteria that can identify most, if not all, dust-contaminated stars we analysed data of the Be X-ray binary CepX4 (e.g. Ulmer et al. 1973), which is one of the most crowded fields observed with RoboPol (Reig et al. 2014). We constructed a number of different quantities with the information from the flat-field image. Those that proved most useful in revealing the effect of dust contamination were the following:

(i) difference between the σ_{bgr} of a star's vertical (horizontal) spots ($\Delta\sigma_{bgr,\,v}$, $\Delta\sigma_{bgr,\,h}$),
(ii) difference between the background value of a star's vertical (horizontal) spots ($\Delta F_{bgr,\,v}$, $\Delta F_{bgr,\,h}$),
(iii) maximum σ_{bgr} (among four spots),
(iv) minimum σ_{bgr} (among four spots).

The distributions of all six quantities are shown in Fig. 12. These quantities are measured in units of normalized counts in the processed master flat image. The outliers of these distributions are stars that coincide with the most prominent dust specks. According to
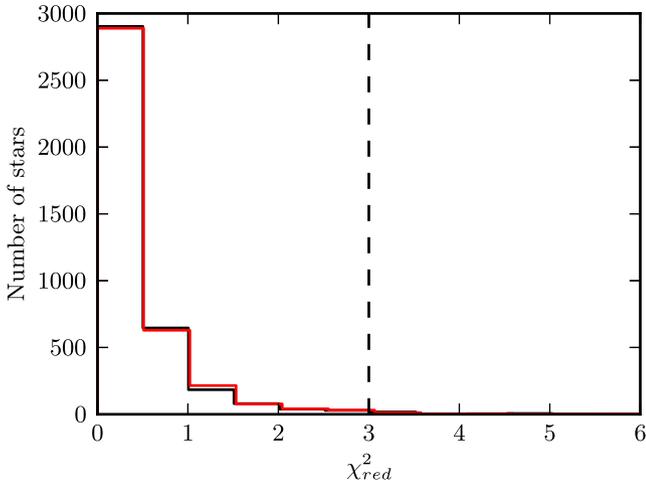
Figure 13. Distributions of $\mathcal{X}_{\mathrm{red}}^2$ of q (black) and u (red) of stars with $\bar{p}/\bar{\sigma}_p \geq 2.5$. The vertical line shows the selected threshold.

these distributions we selected the thresholds depicted by vertical lines in Fig. 12.

Using these criteria we manage to eliminate only stars that are affected by the most obvious dust shadows. A more sophisticated analysis is needed to identify more subtle anomalies on the CCD.

3.7 Statistical assessment

The standard observing strategy in the RoboPol project is to obtain multiple exposures of the same field. We are thus able to use the stability of the measurements (in a statistical sense) to further reject stars with unreliable polarization measurements. One reason for turning to a statistical treatment of the data is that even after the first stage of rigorous cuts described in this section, some systematic errors are still present. These include faint dust specks, reflections from bright stars, and in general, sources with properties around the various thresholds that were used.

First, we choose to work with stars that have reliable measurements of the weighted mean of p ($\bar{p}/\bar{\sigma}_p \geq 2.5$). The weighted mean is calculated by substituting into equation (4) the weighted mean q and u values of a star.

One way to quantify the statistical significance of the differences between the n measurements of a star is by computing the reduced $\mathcal{X}^2$ ($\mathcal{X}_{\mathrm{red}}^2$) of all of its q and u measurements:

$$\mathcal{X}_{\mathrm{red},q}^2 = \frac{1}{n-1} \sum_{j=1}^{n} \frac{(q_j - \bar{q})^2}{(\sigma_{q,j})^2} \qquad (10)$$

and similarly for $\mathcal{X}_{\mathrm{red},u}^2$. By placing a threshold in the value $\mathcal{X}_{\mathrm{red}}^2$ we can eliminate stars that deviate from the expected normal behaviour. The threshold was selected so as to remove the tail of the distribution of all $\mathcal{X}_{\mathrm{red}}^2$ values of stars in the Polaris Flare region. The distributions of these values for q and u measurements are shown in Fig. 13 as well as the selected threshold (vertical line).

Stars that still remain after these cuts and show signs of some type of contamination visible by eye on the raw science images were removed by hand. These include types of contamination already presented in this section as well as projected double stars, for which the analysis does not account.
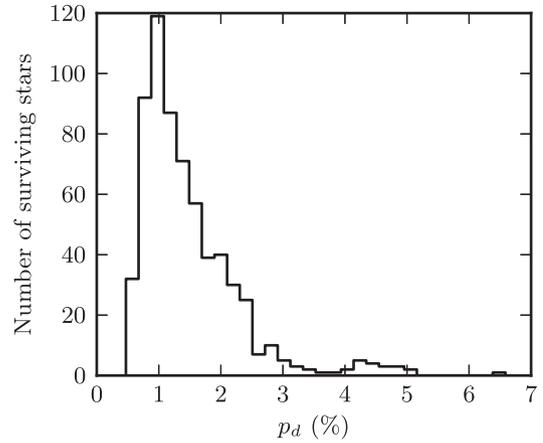
Figure 14. Distribution of debiased fractional linear polarizations of all 641 sources resulting from the analysis.
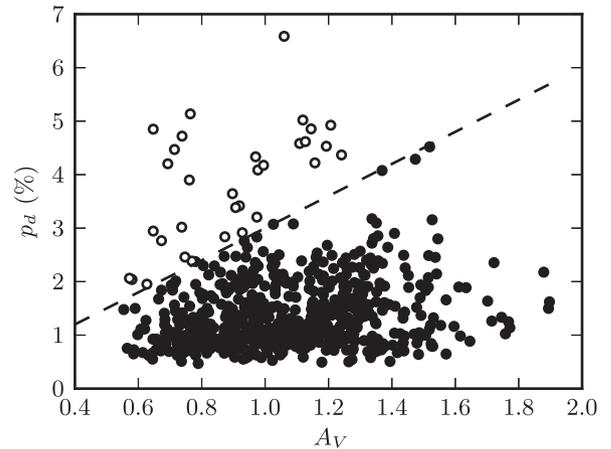
Figure 15. Debiased polarization percentage versus visual extinction, A_V for all our reliably measured stars. The dashed line shows the maximum observable p at all A_V ($p = 0.03A_V$). Stars above the black line are marked with open circles.

4 RESULTS AND DISCUSSION

The analysis provides us with 641 stars with reliable p and χ measurements. The distribution of debiased fractional linear polarizations of all these sources is shown in Fig. 14. The median of the distribution is at 1.3 per cent. Fig. 15 shows the debiased polarization percentage against visual extinction (A_V) taken from the NASA/IPAC Extragalactic Database (NED) which uses the Schlafly & Finkbeiner (2011) extinction map. The dashed line shows the empirically determined upper limit in polarization at a given A_V: $p/A_V = 0.03$ (Serkowski, Mathewson & Ford 1975). We mark sources above this limit with open circles and use this line as a threshold. Sources above the line are considered separately as their polarizations may have an intrinsic contribution.

In order to construct the polarization map of the region we transform all EVPAs (measured with respect to the North–South Selestial Pole direction) into galactic angles according to Stephens et al. (2011). In Fig. 16, we plot the polarization segments of all stars below the p_d–A_V line of Fig. 15 at each star position on the *Herschel*-Spectral and Photometric Imaging Receiver (SPIRE)
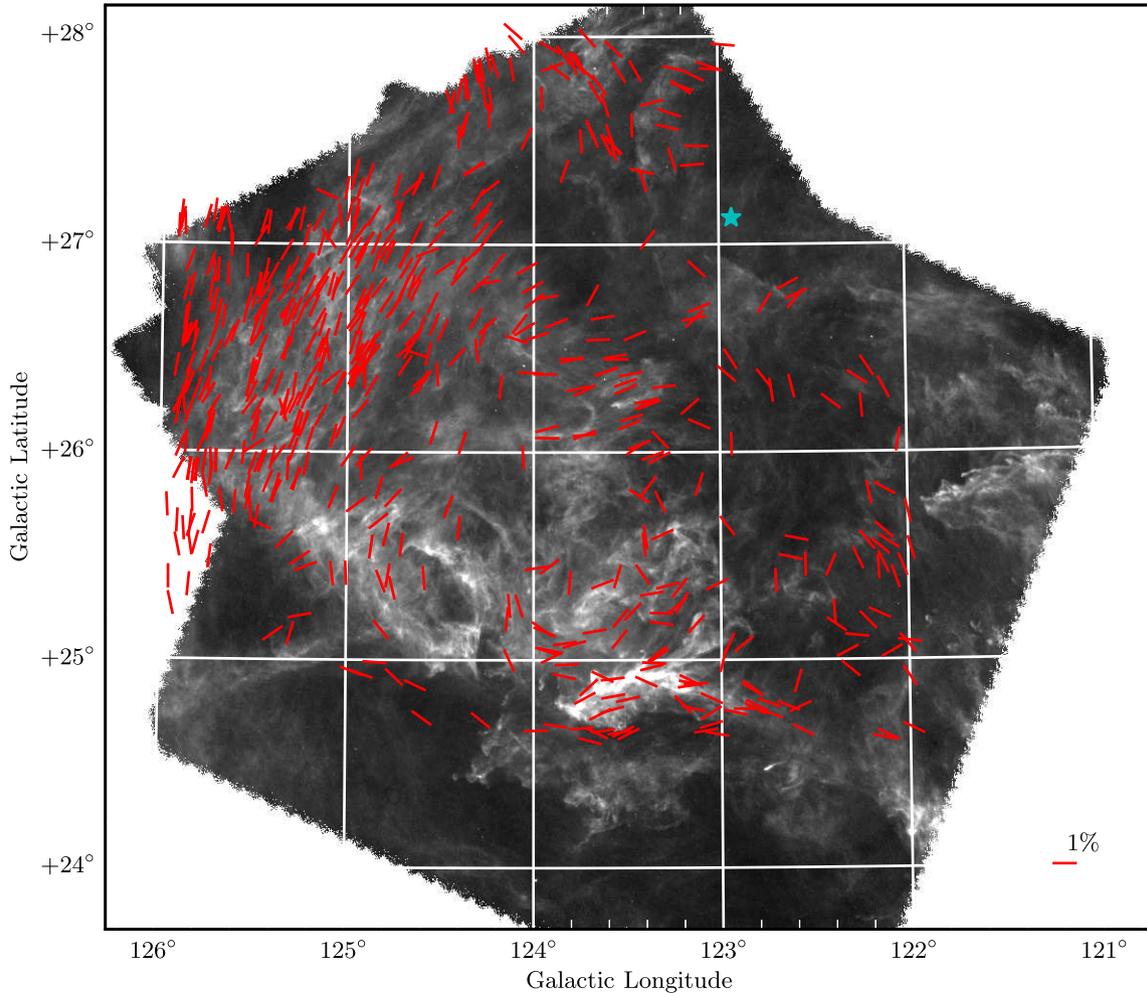
Figure 16. Polarization segments over plotted on top of the 250-µm dust emission image of the Polaris Flare from the online archive of the *Herschel* Gould Belt Survey. The length of each segment is proportional to the debiased fractional linear polarization (p_d) of the star. The horizontal segment at the bottom-right corner is for scale. The blue star marks the position of the North Celestial Pole.

Table 2. Reliable polarization measurements in the Polaris Flare region shown in Fig. 16 (full table is available online).

RA	Dec	$l(°)$	$b(°)$	p_d (per cent)	σ_p (per cent)	$\chi(°)$	$\sigma_\chi(°)$	$\theta_{gal}(°)$
0.318 31	89.146 55	122.725 30	26.295 10	1.5	0.6	− 3	6	9
1.141 58	88.296 58	122.548 90	25.459 90	0.9	0.4	− 10	9	1
1.685 99	88.427 59	122.594 22	25.585 33	0.7	0.3	68	10	78
1.756 19	89.211 22	122.762 49	26.354 22	0.7	0.3	27	10	37
3.270 12	88.341 73	122.626 01	25.492 91	0.9	0.3	68	9	77

250 µm image[1] of the Polaris Flare (André et al. 2010). The length of each segment is proportional to the debiased *p* of the star, calculated using equation (1). These measurements are presented in the online table accompanying this paper (Table 2).

The most striking feature of the polarization map is the extended ordered pattern at large longitudes. In this region the plane-of-the-sky magnetic field appears to be oriented in approximately the same direction as that of the faint striations seen in dust emission. The projected magnetic field in the top part of the map seems to

turn to meet the orientation of the ordered region towards smaller latitudes. Segments at the largest longitudes are mostly parallel to lines of constant longitude, following the projected curvature of a vertical cloud structure that is partly cut-off by the map edges. A border appears to exist, spanning the diagonal of region (124°, 125°), (26°, 27°). Segments below this virtual line form a loop, or eddy-like feature centred at (124°, 25°.5) that covers latitudes down to 24°.5 and longitudes down to 123°. In the south, segments that are projected on the dense filamentary region, also known as the MCLD 123.5+24.9 cloud, appear to be parallel to the axis of the filament and its surrounding less dense gas.

Contrary to this picture, the most prominent feature of the much denser Taurus Molecular Cloud (the B211/B213 filament)

---

[1] The *Herschel* image was available at the *Herschel* Gould Belt Survey online archive (André et al. 2010).

appears perpendicular to the plane-of-the-sky magnetic field. However, a comparison between the two most prominent features of these clouds could be misleading, as they exhibit quite different characteristics. First, the B211 region is known to contain dense cores and YSOs (e.g. Kenyon, Gomez & Whitney 2008), while in MCLD 123.5+24.9 Ward-Thompson et al. (2010) found that all cores were starless and marginally gravitationally bound. Using the same *Herschel* data, Wagle et al. (2015) found that the same cores studied by Ward-Thompson et al. (2010) are most likely gravitationally unbound. So the two regions show a qualitatively different star-forming activity. Secondly, the column density of MCLD 123.5+24.9 is comparable to that of the faint striations found in Taurus, $N(H_2) \sim 10^{21}$ cm^{-2}, an order of magnitude less than B211/B213, which has $N(H_2) > 10^{22}$ cm^{-2} (for column densities, see André et al. 2010; Palmeirim et al. 2013, respectively).

A pattern similar to that found in the striations region of the map has been observed in the Taurus Molecular Cloud. Chapman et al. (2010) have shown that in a diffuse region far away from the main body of the cloud (around 4^{h}50^m, 27°), striations appear aligned with optical and near-infrared polarization segments. The pattern is also present in the densest part of the cloud, around the B211/B213 filamentary region. Palmeirim et al. (2013) found that faint striations on both sides of the B211 filament were parallel to the plane-of-the-sky magnetic field and perpendicular to the filament. They thus speculated that material could be accreting along field lines and on to the filament. In spite of these similarities, the striations seen in the Polaris Flare do not appear connected to a much denser filamentary structure and have an order of magnitude lower column density; $N(H_2) \sim 10^{20}$ cm^{-2} (André et al. 2010); than those in Taurus; $N(H_2) \sim 10^{21}$ cm^{-2} (Goldsmith et al. 2008; Palmeirim et al. 2013).

A detailed, quantitative comparison of the magnetic field as revealed by the map to the dust emission features in the *Herschel* data will be presented in a follow-up paper. Such a study will allow for a thorough investigation of the implications of our findings on the filamentary model of star formation (André et al. 2014).

The general structure of the plane-of-the-sky magnetic field in this cloud agrees qualitatively with that inferred from the polarized emission seen by the *Planck* satellite (Planck collaboration XX 2015). Even though the resolution of the presented map does not allow for a detailed comparison, the orientation of the ordered east part is in fair agreement with that seen in our map. Also, the central-southwest part in the *Planck* map does show a discontinuity of the projected field orientation that could be a sign of the loop that we observe.

The proximity of the cloud suggests that the level of contamination by dust foreground to the cloud is insignificant. Stars lying in front of the cloud will most likely exhibit very low polarization ($\ll$1 per cent) and so would not comply with the p/σ_p threshold, thus they would not affect the map.

The distribution of stars for which we have reliable polarization measurements is not uniform. Segments at higher galactic latitude and longitude are denser than at the lower part of the map. Fig. 17 shows the number of stars in the map binned across the entire observed region. The bin size corresponds to that of the field of view. The brighter regions (containing more stars per bin) are in the area with ordered plane-of-the-sky magnetic field. This non-uniformity is not due to variations in the stellar density across the observed region. It appears as a result of the p/σ_p cut. We find no correlation between this pattern and observing conditions (i.e. seeing, elevation, moon phase). For all fields with a given number of surviving stars (N_s), we calculate the mean extinction $\langle A_V \rangle$. There
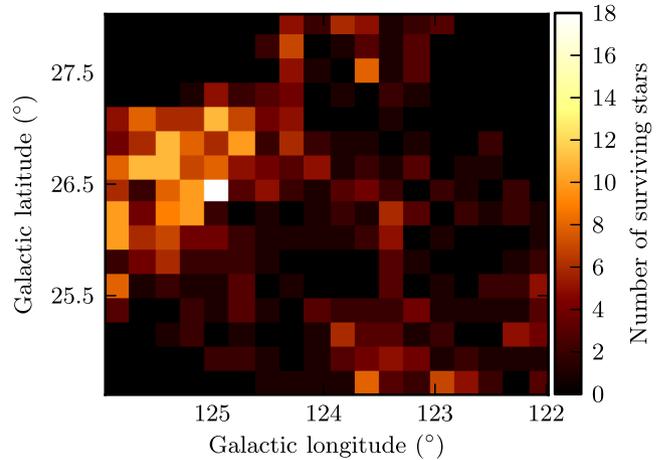
Figure 17. Number of stars in the map per field across the sky. The size of the bins corresponds to that of the field of view. The non-uniformity is a result of the p/σ_p cut.
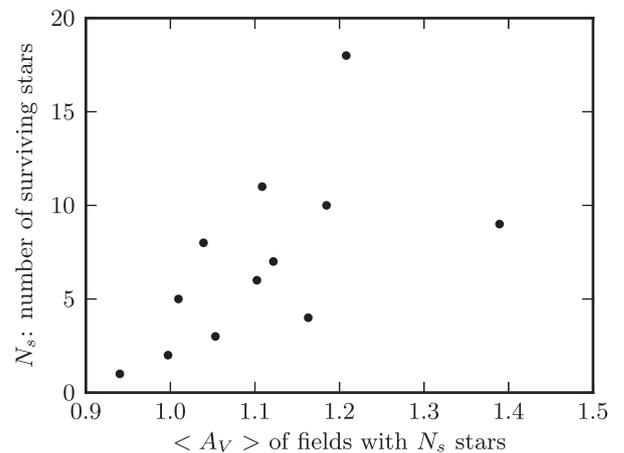
Figure 18. Number of stars (N_s) in Fig. 16 versus mean A_V in all fields with N_s.

is a clear correlation between the two, as can be seen in Fig. 18. We find that the Pearson correlation coefficient between these two sets is 0.59. We therefore conclude that this effect is most likely not the result of some systematic error, but that of the cloud properties. A possibility that could give rise to this effect is a magnetic field whose direction changes from mostly on the plane-of-the-sky in the upper-left part of the map, to having a more pronounced component along the line of sight towards the lower right.

4.1 Potentially intrinsically polarized sources

We plot the polarization segments of sources above the dashed line of Fig. 15 separately in Fig. 19 to be easily distinguished from those whose polarization is primarily affected by the magnetic field of the cloud. The length of the polarization segment of each star is proportional to its debiased p. The orientations of some segments are correlated with the general direction of the plane-of-the-sky magnetic field map of Fig. 16. This is not surprising since the p–A_V line is empirical. Therefore, our choice of setting a threshold based on that line is conservative.

We investigate the possibility that a number of the 32 sources falling above the p_d–A_V line in Fig. 15 could be quasar candidates. Multiwavelength data in this region are sparse, so cross-correlations
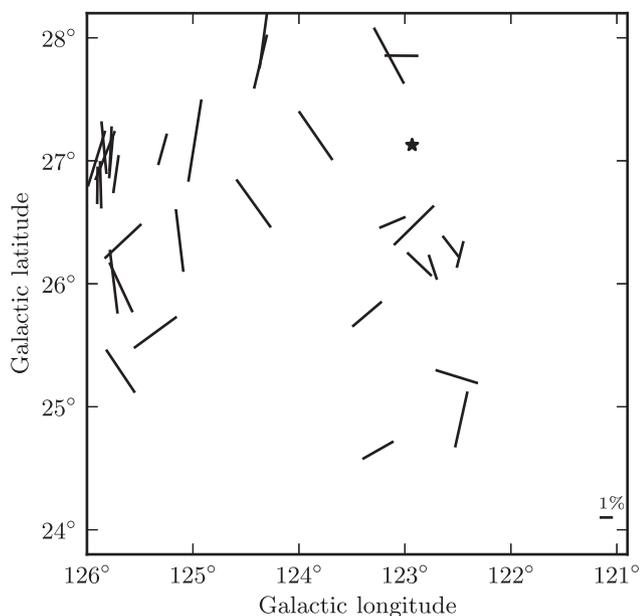
Figure 19. Polarization segments of stars above the p–A_V line shown in Fig. 15. The black star shows the position of the North Celestial Pole while the horizontal segment in the bottom right sets the scale (1 per cent).

with our sample were not particularly fertile. The low resolution of radio data renders direct identification of optical counterparts impractical. For most highly polarized sources (over the p_d–A_V line) we only managed to find data from the USNOB and 2MASS catalogues. Kouzuma & Yamaoka (2010) presented the colour properties of quasar and AGN candidates in the 2MASS catalogue. They demonstrated that candidates can be found preferentially at certain regions of colour–colour diagrams. None of our sources seem to fit into this category. It should be noted, though, that these values have not been redshift-corrected.

5 SUMMARY

We have presented optical linear polarization measurements of stars projected on the Polaris Flare field. These measurements reveal the plane-of-the-sky magnetic field structure of the cloud. The observations span about 10 deg^2 of the region and have been conducted with the RoboPol polarimeter in the R band. We presented adjustments to the automated data reduction pipeline that were necessary for the analysis of sources in the entire 13 arcmin $\times$ 13 arcmin field of view. We have investigated possible sources of systematic errors and have presented our methods for correcting for each one.

We have produced a map of 609 polarization segments showing the magnetic field structure of the cloud as projected on the plane of the sky. The median debiased p is 1.3 per cent. The projected field shows a complicated, ordered structure throughout the map. To the top-left part of the map, the field is aligned with the striations seen in dust emission. The bottom-right parts show the presence of an eddy-like feature spanning roughly 2° in diameter. Our results compare well with the *Planck* map of polarized emission of the cloud. The distribution of stars with reliable polarization measurements across the field is not uniform, with most stars lying in the top left of the region. This is most likely due to the intrinsic properties of the magnetic field structure.

REFERENCES

André Ph. et al., 2010, A&A, 518, L102
André Ph. et al., 2014, Protostars and Planets VI, Univ. Arizona Press, Tuscan, NJ, preprint (arXiv:1312.6232)
Astropy Collaboration, 2013, A&A, 558, A33
Bailey J., Hough J. H., 1982, PASP, 94, 618
Berdyugin A., Piirola V., Teerikorpi P., 2014, A&A, 561, A24
Chapman N. L., Goldsmith P. F., Pineda J. L., Clemens D. P., Li D., Krčo M., 2011, ApJ, 741, 21
Eswaraiah C., Pandey A. K., Maheswar G., Medhi B. J., Pandey J. C., Ojha D. K., Chen W. P., 2011, MNRAS, 411, 1418
Falgarone E., Panis J. F., Heithausen A., Pérault M., Stutzki J., Puget J.-L., Bensch F., 1998, A&A, 331, 669

Goldsmith P. F., Heyer M., Narayanan G., Snell R., Li D., Brunt C., 2008, ApJ, 680, 428

Heiles C., 1984, ApJS, 55, 585

Heiles C., 2000, AJ, 119, 923

Heithausen A., Stacy J. G., de Vries H. W., Mebold U., Thaddeus P., 1993, A&A, 268, 265

Hily-Blant P., Falgarone E., 2009, A&A, 500, L29

Howell S. B., 1989, PASP, 101, 616

Hunter J. D., 2007, Comput. Sci. Eng., 9, 90

Jones E., Oliphant T., Peterson P., 2001, SciPy: Open Source Scientific Tools for Python. Available at: www.scipy.org

Kenyon S. J., Gomez M., Whitney B. A., 2008, Handbook of Star Forming Regions Vol. 1: The Northern Sky. Astron. Soc. Pac., San Francisco, p. 405

King O. G. et al., 2014, MNRAS, 442, 1706

King O. G. et al., 2014, MNRAS, 445, L114

Kouzuma S., Yamaoka H., 2010, in Peterson B., Somerville R., Storchi-Bergmann T., eds, Proc. IAU Symp. 267, Co-Evolution of Central Black Holes and Galaxies. Cambridge Univ. Press, Cambridge, p. 113

Miville-Deschênes et al., 2010, A&A, 518, L104

Palmeirim P. et al., 2013, A&A, 550, A38

Pavlidou V. et al., 2014, MNRAS, 442, 1693

Planck Collaboration XIX, 2015, A&A, 576, A104

Planck Collaboration XX, 2015, A&A, 576, A105

Reig P., Blinov D., Papadakis I., Kylafis N., Tassis K., 2014, MNRAS, 445, 4235

Schlafly E. F., Finkbeiner D. P., 2011, ApJ, 737, 103

Schlafly E. F. et al., 2014, ApJ, 786, 29

Schmidt G. D., Elston R., Lupie O. L., 1992, AJ, 104, 1563

Serkowski K., Mathewson D. S., Ford V. L., 1975, ApJ, 196, 261

Simmons J. F. L., Stewart B. G., 1985, A&A, 142, 100

Stephens I. W., Looney L. W., Dowell C. D., Vaillancourt J. E., Tassis K., 2011, ApJ, 728, 99

Ulmer M. P., Baity W. A., Wheaton W. A., Peterson L. E., 1973, ApJ, 184, L117

Vaillancourt J. E., 2006, PASP, 118, 1340

Wagle G. A., Troland T. H., Ferland G. J., Abel N. P., 2015, preprint (arXiv:1504.06311)

Ward-Thompson D. et al., 2010, A&A, 518, L92

SUPPORTING INFORMATION

Additional Supporting Information may be found in the online version of this paper:

Table2.dat

(http://mnras.oxfordjournals.org/lookup/suppl/doi:10.1093/mnras/stv1301/-/DC1).

Please note: Oxford University Press are not responsible for the content or functionality of any supporting materials supplied by the authors. Any queries (other than missing material) should be directed to the corresponding author for the paper.

This paper has been typeset from a TEX/LATEX file prepared by the author.

Erratum: Optical polarization map of the Polaris Flare with RoboPol

by G. Panopoulou,[1,2]★ K. Tassis,[1,2]★ D. Blinov,[1,3] V. Pavlidou,[1,2] O. G. King,[4]
E. Paleologou,[1] A. Ramaprakash,[5] E. Angelakis,[6] M. Baloković,[4] H. K. Das,[5]
R. Feiler,[7] T. Hovatta,[8] P. Khodade,[5] S. Kiehlmann,[8] A. Kus,[7] N. Kylafis,[1,2]
I. Liodakis,[1] A. Mahabal,[4] D. Modi,[5] I. Myserlis,[6] I. Papadakis,[1,2]
I. Papamastorakis,[1,2] B. Pazderska,[7] E. Pazderski,[7] T. J. Pearson,[4] C. Rajarshi,[5]
A. C. S. Readhead,[4] P. Reig[1,2] and J. A. Zensus[6]

[1]*Department of Physics and ITCP†, University of Crete, 71003 Heraklion, Greece*
[2]*Foundation for Research and Technology – Hellas, IESL, Voutes, 7110 Heraklion, Greece*
[3]*Astronomical Institute, St Petersburg State University,Universitetsky pr. 28, Petrodvoretz, 198504 St Petersburg, Russia*
[4]*Cahill Center for Astronomy and Astrophysics, California Institute of Technology, 1200 E California Blvd, MC 249-17, Pasadena, CA 91125, USA*
[5]*Inter-University Centre for Astronomy and Astrophysics, Post Bag 4, Ganeshkhind, Pune 411 007, India*
[6]*Max-Planck-Institut für Radioastronomie, Auf dem Hügel 69, D-53121 Bonn, Germany*
[7]*Toruń Centre for Astronomy, Nicolaus Copernicus University, Faculty of Physics, Astronomy and Informatics, Grudziadzka 5, PL-87-100 Toruń, Poland*
[8]*Aalto University Metsähovi Radio Observatory, Metsähovintie 114, FI-02540 Kylmälä, Finland*

Key words: errata, addenda – polarization – stars: formation – ISM: clouds – ISM: individual objects: Polaris Flare.

We report an error in the article 'Optical polarization map of the Polaris Flare with RoboPol', published in 2015, MNRAS, 452, 715 (hereafter Panopoulou et al. 2015). The error only affects the conversion of the Electric Vector Position Angle (EVPA) from the celestial system (in which the values are correct) to the Galactic system. The formula used to convert the polarization angles from the celestial to the Galactic system, taken from Stephens et al. (2011) was found to be incomplete. In the following, we explain the formula used by these authors and its limitations, and describe the correction.

We shall consider two objects at Galactic coordinates (l, b) and (l, b'). Their coordinates in the celestial system are (α, δ) and (α', δ), so that they are equidistant from the North Celestial Pole (NCP). The EVPA measured at the position of each object from the line that connects it to the NCP and towards the East (θ) can be converted to an angle with respect to the North Galactic Pole (NGP) (measured towards increasing longitudes) by:

$$\hat{\theta}_G = \hat{O} + \hat{\theta} \qquad (1)$$

where $\hat{O}$ is the angle between lines that connect the object to the NCP and NGP (angles $\hat{o}$ and $\hat{o}'$, shown in Fig. 1), as explained by Stephens et al. (2011). $\hat{\theta}_G$ is held in the range $[0°, 180°]$ by adding or subtracting $180°$. For the triangles created by each object and the two poles in our Fig. 1, the law of sines gives:

$$\sin \hat{o} = \frac{\sin \hat{a}}{\sin A} \sin B = \sin \hat{o}' \qquad (2)$$

Stephens et al. (2011) find the angle $\hat{O}$ by:

$$\hat{O} = \sin^{-1}\left(\frac{\sin \hat{a} \sin B}{\sin A}\right). \qquad (3)$$

★E-mail: panopg@physics.uoc.gr (GP); tassis@physics.uoc.gr (KT)
† Institute for Theoretical and Computational Physics, formerly Institute for Plasma Physics.

Since the arcs A and B and the angle $\hat{a}$ are common for both triangles, the angles $\hat{o}$ and $\hat{o}'$ are incorrectly found to be equal.

This ambiguity can be alleviated if we use both the sine and cosine of the angle $\hat{O}$. We shall proceed to derive a formula for angle $\hat{o}$, which can be applied for any angle $\hat{O}$. The law of cosines for the triangle with sides A, B, C is:

$$\cos B = \cos A \cos C + \sin A \sin C \cos \hat{o} \qquad (4)$$

We can find the tangent of $\hat{o}$ by solving equation (4) for $\cos \hat{o}$ and dividing equation (2) by the result:

$$\tan \hat{o} = \frac{\sin \hat{a} \sin B}{\frac{\cos B}{\sin C} - \frac{\cos A \cos C}{\sin C}} \qquad (5)$$

We may obtain a formula which only takes into account coordinates in the galactic reference frame by substituting $\cos A$ from the law of cosines:

$$\cos A = \cos B \cos C + \sin B \sin C \cos \hat{a} \qquad (6)$$

into equation (5). Next we use the identity $\sin^2 C = 1 - \cos^2 C$ to simplify the denominator and finally we divide both the numerator and denominator by $\sin B$ to arrive at:

$$\tan \hat{o} = \frac{\sin \hat{a}}{\cot B \sin C - \cos C \cos \hat{a}} \qquad (7)$$

Before arriving at the final formula for $\hat{o}$, we make the following substitutions in equation (7):

$$\hat{a} = l_{NCP} - l, \quad B = 90° - b_{NCP}, \quad C = 90° - b.$$

Finally, the angle $\hat{o}$ is:

$$\hat{o} = \tan^{-1}\left(\frac{\sin(l_{NCP} - l)}{\tan b_{NCP} \cos b - \sin b \cos(l_{NCP} - l)}\right) \qquad (8)$$

where we use the arctangent function with two arguments to obtain the angle in the appropriate quadrant. This formula is equivalent to the one used by Appenzeller (1968). The results returned by
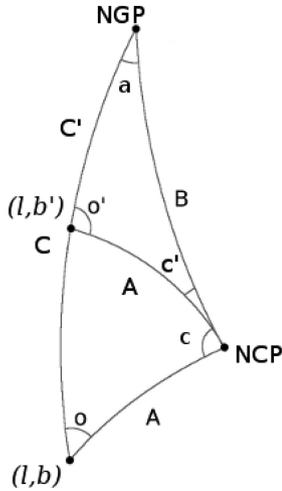
Figure 1. Triangles on the Celestial sphere connecting objects at (l, b) and (l, b') to the NGP and NCP. The angles $\hat{o}$ and $\hat{o}'$ are needed to convert polarization angles in the celestial system to angles in the galactic system. Angle $\hat{o}'$ is incorrectly calculated in Panopoulou et al. (2015).

equation (8) have been compared to those calculated by the function BEAR of the FORTRAN library SLALIB (http://ascl.net/1403.025), which uses a different, but equivalent formula and agree within less than an arcsecond.

Angles computed using equation (3) are incorrect for objects with:

$$90° - b \leq 63°, \quad 45° \leq l \leq 205° \text{ (for } b > 0°)$$

$$90° - |b| \leq 63°, \quad l \leq 20° \quad \text{or} \quad l \geq 205° \text{ (for } b \leq 0°)$$

i.e. for objects within two half-disc regions centred around the two galactic poles. This happens because for these parts of the sky, the angle returned by the arcsine function is the supplementary angle of the desired one. This affects none of the measurements in Stephens et al. (2011) as they are mainly near the Galactic plane. However, the data in Panopoulou et al. (2015) are near the NCP, which has $b_{NCP} = 27°$. Since in Panopoulou et al. (2015) we used equation (3) to find the conversion to $\hat{\theta}_G$, and make the map in Fig. 16, the orientations of segments on the top of the map (in total 77) differ by more than 5° from the correct value. Fig. 16 shows all polarization segments with the correct orientation. In the data accompanying the paper, the Galactic angles of these measurements should be corrected, and we have updated the catalogue in http://cds.u-strasbg.fr/ to contain the correct values. We also show a corrected version of Fig. 19, in which four segments are significantly altered.

The error presented above only affects a small part of the region studied. Our finding that the magnetic field exhibits ordered structure and seems to be aligned with cloud filaments is enhanced by the correction. Thus, the conclusions of Panopoulou et al. (2015) are not significantly affected by the error presented here.
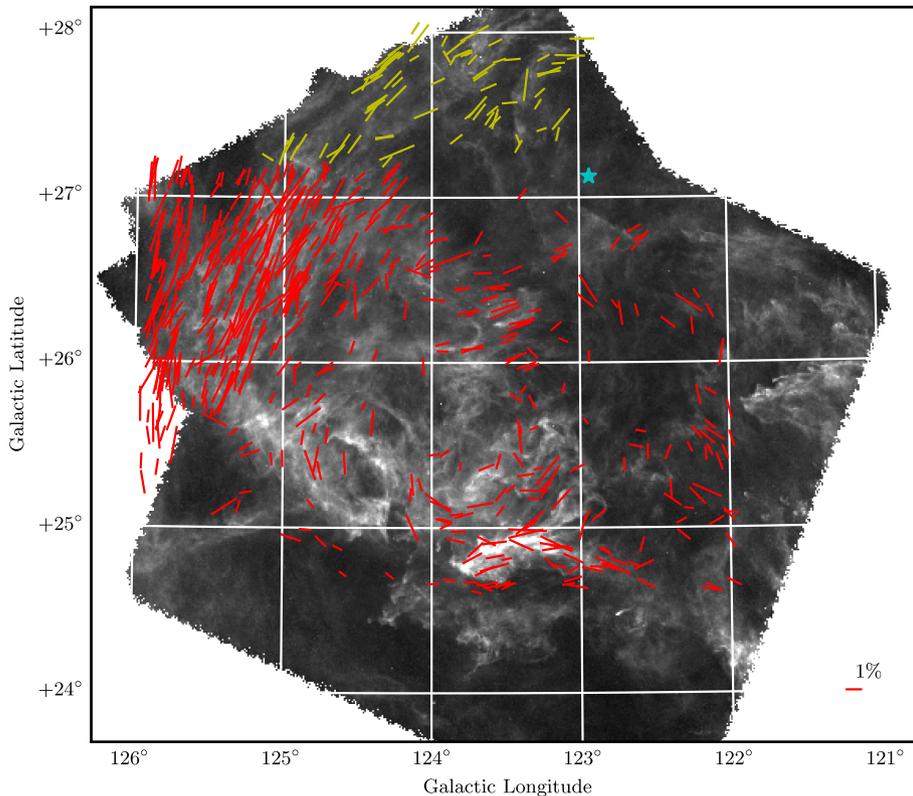
Figure 16. Corrected version of Fig. 16 in Panopoulou et al. (2015): polarization segments over plotted on top of the 250 μm dust emission image of the Polaris Flare from the online archive of the *Herschel* Gould Belt Survey. Yellow segments are measurements with Galactic angles affected by the incomplete conversion by more than 5°.
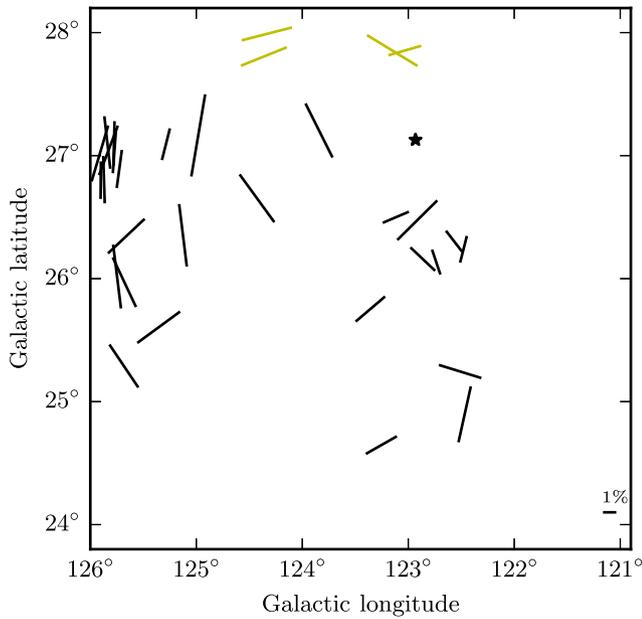
Figure 19. Corrected version of Fig. 19 in Panopoulou et al. (2015): polarization segments of possibly intrinsically polarized sources. Segments affected by the error reported here are shown in yellow.

REFERENCES

Appenzeller I., 1968, ApJ, 151, 907
Panopoulou G. V. et al., 2015, MNRAS, 452, 715
Stephens I. W., Looney L. W., Dowell C. D., Vaillancourt J. E., Tassis K., 2011, ApJ, 728, 99

SUPPORTING INFORMATION

Additional Supporting Information may be found in the online version of this article:

Table 2.
(http://www.mnras.oxfordjournals.org/lookup/suppl/doi:
10.1093/mnras/stw1785/-/DC1).

Please note: Oxford University Press is not responsible for the content or functionality of any supporting materials supplied by the authors. Any queries (other than missing material) should be directed to the corresponding author for the article.

This paper has been typeset from a TEX/LATEX file prepared by the author.

Chapter 4

Connecting field and structures in a translucent cloud

Having observed the morphology of the magnetic field in the Polaris Flare, we then used our results to infer the role of the magnetic field in the cloud. We quantified the connection of Herschel dust filaments to the plane-of-sky magnetic field through a comparison of their relative orientations. By studying the magnetic field morphology, we estimated the strength of the projected magnetic field and its importance relative to turbulent motions. Our results showed that there are regions in the cloud where the field is ordered and dynamically important compared to turbulence, thus providing a handle on the nature of the field at scales smaller than the Planck data resolution.

The magnetic field and dust filaments in the Polaris Flare

G. V. Panopoulou,[1,2]★ I. Psaradaki[1] and K. Tassis[1,2]

[1]*Department of Physics and Institute for Theoretical and Computational Physics,*[†]*University of Crete, 71003, Heraklion, Greece*
[2]*Foundation for Research and Technology – Hellas, IESL, Voutes, 71110 Heraklion, Greece*

ABSTRACT

In diffuse molecular clouds, possible precursors of star-forming clouds, the effect of the magnetic field is unclear. In this work, we compare the orientations of filamentary structures in the Polaris Flare, as seen through dust emission by *Herschel*, to the plane-of-the-sky magnetic field orientation (B_{pos}) as revealed by stellar optical polarimetry with RoboPol. Dust structures in this translucent cloud show a strong preference for alignment with B_{pos}. Of the field orientations, 70 per cent are consistent with those of the filaments (within $30°$). We explore the spatial variation of the relative orientations and find it to be uncorrelated with the dust emission intensity and correlated to the dispersion of polarization angles. Concentrating on the area around the highest column density filament, and on the region with the most uniform field, we infer the B_{pos} strength to be 24–120 μG. Assuming that the magnetic field can be decomposed into a turbulent and an ordered component, we find a turbulent-to-ordered ratio of 0.2–0.8, implying that the magnetic field is dynamically important, at least in these two areas. We discuss implications for three-dimensional field properties, as well as for the distance estimate of the cloud.

Key words: polarization – ISM: clouds – ISM: individual objects: Polaris Flare – ISM: magnetic fields – ISM: structure.

1 INTRODUCTION

The structure of interstellar clouds is highly complex, characterized by the existence of elongations, or filaments, of various scales (e.g. Myers 2009). The Gould Belt Survey conducted by the *Herschel* space observatory captured the morphologies of the nearby molecular clouds with unprecedented sensitivity and detail, allowing the study of filamentary structures to advance (e.g. André et al. 2010). A better understanding of filament properties and their relation to their environments could provide clues as to how clouds proceed to form stars.

To this end, important questions to answer are whether the magnetic field interacts with filaments and how this interaction takes place. Its role in the various stages and environments of star formation is hotly debated. In simulations of super-Alfvénic turbulence, magnetic fields are tangled due to the gas flow (e.g. Ostriker, Stone & Gammie 2001; Falceta-Gonçalves, Lazarian & Kowal 2008). In such models, filaments are formed by shock interactions (Heitsch et al. 2001; Padoan et al. 2001) and the magnetic field within them is found to lie along their spines (Heitsch et al. 2001; Ostriker et al. 2001; Falceta-Gonçalves et al. 2008). In studies of

sub/trans-Alfvénic turbulence, where the magnetic field is dynamically important, filament orientations with respect to the large-scale ordered field depend on whether gravity is important. In simulations where gravity is not taken into account (e.g. Falceta-Gonçalves et al. 2008) or structures are gravitationally unbound (Soler et al. 2013), filaments are parallel to the magnetic field. However, self-gravitating elongated structures are perpendicular to the magnetic field (Mouschovias 1976; Nakamura & Li 2008; Soler et al. 2013). Both configurations are the result of the magnetic force facilitating flows along field lines. Finally, if the magnetic field surrounding a filament has a helical configuration (Fiege & Pudritz 2002), then the relative orientation of the two as projected on to the plane of the sky can have any value, depending on projection, curvature and whether the field is mostly poloidal or toroidal (Matthews, Wilson & Fiege 2001).

The relation between cloud structure and the magnetic field was highlighted early on by observational studies (e.g. in the Pleiades; Hall 1955). On cloud scales, Li et al. (2013) found that the distribution of relative orientations of elongated clouds and the magnetic field (both projected on to the plane of the sky) is bimodal: clouds either tend to be parallel or perpendicular (in projection) to the magnetic field. In a series of papers, the *Planck* collaboration compared the magnetic field to the interstellar medium (ISM) structure across a range of hydrogen column densities (N_H). Planck Collaboration XXXII (2016a) considered the orientation of structures in the diffuse

ISM in the range of $N_H \sim 10^{20}$–10^{22} and found significant alignment with the plane-of-the-sky magnetic field (B_{pos}). Planck Collaboration XXXV (2016b) found that, in their sample of 10 nearby clouds, substructure at high column density tends to be perpendicular to the magnetic field, whereas at low column density there is a tendency for alignment.

Studies of optical and near-infrared (NIR) polarization, tracing B_{pos} in cloud envelopes, show that dense filaments within star-forming molecular clouds tend to be perpendicular to the magnetic field (Pereyra & Magalhães 2004; Alves, Franco & Girart 2008; Chapman et al. 2011; Sugitani et al. 2011). However, there are diffuse linear structures, called striations, that share a common smoothly varying orientation and are situated either in the outskirts of clouds (Goldsmith et al. 2008; Alves de Oliveira et al. 2014) or near dense filaments (Palmeirim et al. 2013). These structures show alignment with B_{pos} (van den Bergh 1956; Chapman et al. 2011; Palmeirim et al. 2013; Alves de Oliveira et al. 2014; Malinen et al. 2016). The extremely well-sampled data of Franco & Alves (2015) in Lupus I show that B_{pos} is perpendicular to the cloud's main axis but parallel to neighbouring diffuse gas. There are, however, exceptions to this trend (e.g. L1506 in Taurus; Goodman et al. 1990).

While the large-scale magnetic field has been mapped in many dense molecular clouds, little is known about the field in translucent molecular clouds. In this paper, we investigate the relation of the magnetic field to the gas in the Polaris Flare, a high-latitude diffuse cloud. This molecular cloud extends above the galactic plane and is at an estimated distance between 140 and 240 pc, although this is debated (e.g. Zagury, Boulanger & Banchet 1999; Schlafly et al. 2014). It is a translucent region ($A_V \lesssim 1$ mag; Cambrésy et al. 2001) devoid of star formation activity (André et al. 2010; Men'shchikov et al. 2010; Ward-Thompson et al. 2010), except for the existence of possibly pre-stellar core(s) in the densest part of the cloud MCLD 123.5+24.9 (MCLD123; Ward-Thompson et al. 2010; Wagle et al. 2015). Signatures of intense velocity shear have been identified in this region and have been linked to the dissipation of supersonic (but trans-Alfvénic) turbulence (Hily-Blant & Falgarone 2009, and references therein).

The dust emission in ~ 16 deg^2 of the Polaris Flare has been mapped by *Herschel* (Pilbratt et al. 2010) as part of the *Herschel* Gould Belt Survey (André et al. 2010; Miville-Deschênes et al. 2010; Men'shchikov et al. 2010; Ward-Thompson et al. 2010). The *Planck* space observatory has provided the first map of the plane-of-the-sky magnetic field in the area at a resolution of tens of arcmin (Planck Collaboration XIX 2015a; Planck Collaboration XX 2015b). In Panopoulou et al. (2015, hereafter Paper I), we presented a map of the plane-of-the-sky magnetic field in the same area, measured by stellar optical polarimetry with RoboPol. The resolution of optical polarimetry (pencil beams) and coverage of our data allow for a detailed comparison between the magnetic field and cloud structure. The goal of this work is to compare the magnetic field orientation to that of the linear structures in the Polaris Flare and to estimate the plane-of-the-sky component of the field in various regions of the cloud. In Section 2.1, we present the distribution of relative orientations of filaments and B_{pos} throughout the mapped region. We compare properties such as the relative orientations and polarization angle dispersion across the map in Section 2.2 and we present the distribution of filament widths in Section 2.3. We analyse two regions of interest separately in Section 2.4 and estimate the B_{pos} strength in these regions in Section 2.5. Finally, we discuss implications of our findings in Section 3 and summarize our results in Section 4.

2 RESULTS

2.1 Relative orientations of B_{pos} and dust filaments

We use the *Herschel*-SPIRE 250-μm map[1] in our analysis of cloud structure. Filamentary structures are evident throughout the *Herschel* image of this translucent cloud. We compare the orientations of these structures to the optical polarization data presented[2] in Paper I, shown as line segments on the 250-μm dust emission image in Fig. 1. The segment length is proportional to the (debiased) fractional linear polarization, p_d. A line showing a p_d of 2 per cent is located in the bottom-left corner and a line of 1 pc length is located in the top left. We adopt a distance of 150 pc to be consistent with the analysis of *Herschel* data in the literature (based on Heithausen 1999). The rectangles highlight regions of interest that are referred to in the following analysis. The panels on the right show enlarged versions of both regions. A preliminary inspection of the map shows that the orientation of B_{pos} revealed from optical polarimetry seems to correlate well with the apparent orientations of filaments in most of the map. This correlation can be quantified by measuring the relative orientation of the two.

An excellent tool for determining the orientation of linear structures, irrespective of their brightness, is the rolling Hough transform (RHT; Clark, Peek & Putman 2014). It was introduced in the study of diffuse H I and has also been used in analyses of molecular clouds (Koch & Rosolowsky 2015; Malinen et al. 2016). The RHT quantifies the linearity of cloud structure for every image pixel. It does so by measuring the intensity along any given direction within a disc region surrounding each pixel. The RHT returns the probability that a pixel is part of a linear structure as a function of angle. Integrating for all angles results in a visualization of linear features in the image (RHT backprojection).

We have applied the RHT to the *Herschel* 250-μm image and we present the RHT backprojection in Fig. 2. The darkest pixels in the image belong to well-defined linear structures in intensity (filaments and striations). Apart from these structures, the RHT backprojection contains some spurious features (e.g. in the bottom part of the map where dust emission is very faint or absent). These features seem correlated with the *Herschel* scanning direction. Because neither cloud structure nor magnetic field orientation coincide with this direction, the effect of these features on the distribution of relative orientations will be to randomize a very small number (if any) of values, introducing misalignment.

The polarization segments tracing the orientation of B_{pos} are overplotted on the backprojection in Fig. 2. At the position of each polarization measurement, we calculate the mean RHT angle (θ_{RHT}, defined as in Clark et al. 2014), within a circle of diameter 0.17 pc (corresponding to an angular diameter of 4 arcmin). We then compare θ_{RHT} to the orientation of each polarization segment, θ, by

---

[1] The map is part of the preliminary data available at the *Herschel* Gould Belt Survey archive.

[2] Following the publication of the catalogue of 609 measurements in Paper I, we discovered an error in the conversion from the polarization angle with respect to the North Celestial Pole to the angle with respect to the North Galactic Pole. This error affected the orientation of 77 segments in the top of the published map. We have corrected the formula used for the conversion and have updated the values of the galactic angle in the published catalogue. This updated version is used in this work and can be found at http://cds.u-strasbg.fr/. No other changes have been made to the original release.
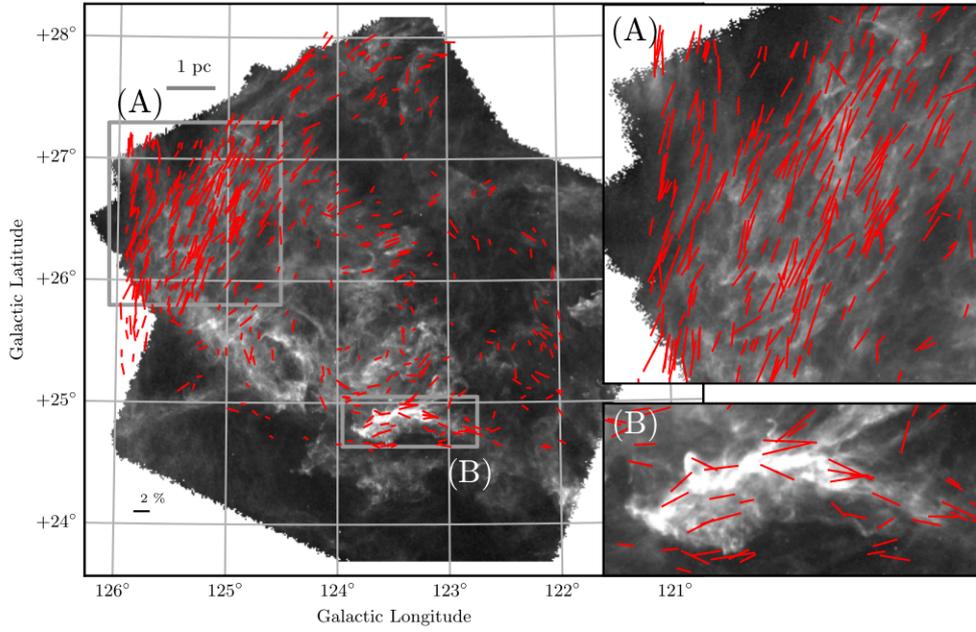
Figure 1. *Herschel* 250-μm image of the Polaris Flare (grey-scale). Segments are the optical polarization data from Paper I. Regions A (striations) and B (MCLD123), indicated by the rectangles in the full map, are shown in the top-right and bottom-right panels for detail. Scales of 1 pc and $p_d = 2$ per cent are shown in the top-left and bottom-left corners of the full map.
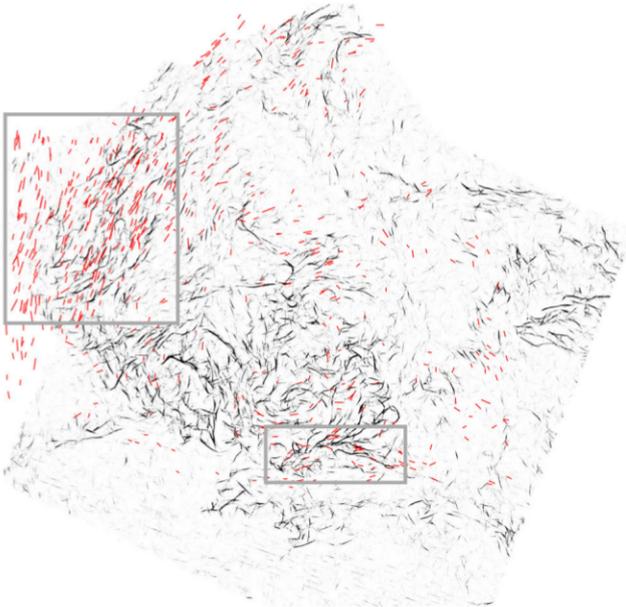
Figure 2. RHT visualization of the *Herschel* 250-μm image of the Polaris Flare (grey-scale). Dark pixels correspond to a high probability of linearity. The optical polarization segments from Paper I have been overplotted in red. Regions A and B are outlined as in Fig. 1.

taking the absolute value of their difference,[3] $|\theta - \theta_{RHT}|$. There are 39 polarization measurements that extend outside the dust emission image and are not included in the comparison to cloud structures. The distribution of the relative orientations for the 570 remaining measurements is plotted in Fig. 3. There is a strong preference in
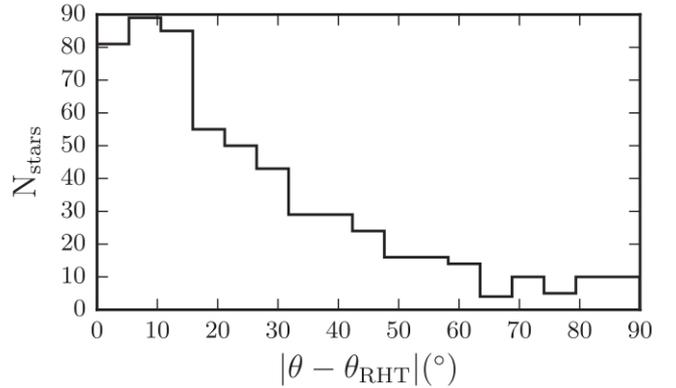
Figure 3. Distribution of the absolute difference between the angle of each polarization segment and the RHT angle in its vicinity ($|\theta - \theta_{RHT}|$). The distribution contains all 570 polarization measurements that lie in the *Herschel* image.

alignment: 70 per cent of polarization measurements are within $30°$ of the orientation of linear features in their surrounding gas. A Monte Carlo run showed that the probability of obtaining this correlation by chance is less than 10^{-6}. Only 8 per cent are within $30°$ of being perpendicular to their surrounding gas. We explored the effect of changing the parameters of the RHT, as well as the area around each star used in calculating θ_{RHT}, and found no significant variation for a large portion of the parameter space.

2.2 Variation across the field

The results presented above on the alignment of filaments and B_{pos} concerned the entire map. However, both field and cloud structure are not homogeneous across the cloud. For example, there is a low column density area of striations, marked by the rectangle as region A in Fig. 1, where B_{pos} exhibits ordered structure. Adjacent to this area, towards lower latitude and longitude, in a significant portion

---

[3] All angles are defined with respect to the North and increase towards the East, according to the International Astronomical Union (IAU) convention.

of the map, measurements are sparse and polarization angles show substantial dispersion.

The various trends existing in the measured cloud properties can be better visualized by constructing maps of average (smoothed) quantities across the sky. The maps are constructed by creating a grid (5-arcmin squares) of the field. The value at each grid centre is calculated by averaging the values of star measurements within 10 arcmin of it. The final map is smoothed using a boxcar filter of 5 arcmin width. Fig. 4 shows such maps of various quantities: (a) number of significant stellar polarization measurements ($p_d/\sigma_p \geq 2.5$); (b) *Herschel* 250-μm intensity; (c) polarization angle, θ; (d) scatter of θ; (e) $|\theta - \theta_{RHT}|$; (f) p_d. Only bins with at least five measurements were used to produce the maps (reducing this number to three did not make a qualitative difference).

The number of significant stellar polarization measurements is highest in region A, which is the bright part in the upper left of the map in panel (a). The number density (per 5-arcmin bin) in this area is more than twice that in the rest of the map. Smaller local maxima are found: (i) in region B; (ii) in the centre of the map ($123°.5, +26°.3$); (iii) above the striations at ($124°.5, +27°.5$). As noted in Paper I, this variation in the number of measurements is not due to variations in stellar density across the field, or due to systematics such as observing conditions. Panel (b) shows the *Herschel* 250-μm image smoothed with a boxcar filter of 5-arcmin width. The MCLD123 filament (region B) stands out as a maximum of intensity. By comparing the number density of significant stellar polarization measurements to the dust emission intensity (panels a and b), we find that the overall structure of the two maps is significantly different. Therefore, the variation of the density of significant polarization measurements cannot be attributed to variations in the column density.

The average polarization angles in panel (c) are calculated as the circular mean,

$$\bar{\theta} = \frac{1}{2} \arctan \left[\frac{\sum_{i=1}^{N} \sin(2\theta_i)}{\sum_{i=1}^{N} \cos(2\theta_i)} \right], \tag{1}$$

where N is the number of measurements in each bin. The average polarization angle defines a number of domains of different orientation throughout the field, separated by abrupt angle changes. The thin dark curves at the edges of some domains are an artefact of the smoothing; they do not represent measurements of 90°. $\bar{\theta}$ seems to rotate clockwise from 160° (bright yellow) in region A, to 40° (blue) below the centre of the map.

The scatter of polarization angles std(2θ) in panel (d) is measured using the circular standard deviation:

$$\text{std}(2\theta) = \sqrt{-2 \ln \left[\sqrt{\left(\frac{1}{N} \sum_{i=1}^{N} \sin 2\theta_i \right)^2 + \left(\frac{1}{N} \sum_{i=1}^{N} \cos 2\theta_i \right)^2} \right]}. \tag{2}$$

The values obtained by this equation do not represent the dispersion that would characterize a normal distribution of angles. They only serve for comparison between the various areas of the map. The bright regions in panel (d) (large standard deviations) correspond to regions with very few measurements, as can be seen by comparing with panel (a). Region A and an area with std(2θ) < 30° in the centre of the map stand out as the areas with lowest dispersion.

The relative orientation of B_{pos} and the filamentary structures in the cloud, shown in panel (e), are very similar to the std(2θ) map. Regions characterized by a large polarization angle dispersion appear to coincide with regions where filaments are perpendicular

to B_{pos}. The preference in alignment throughout the map, seen in Fig. 3, is evident, as regions with $|\theta - \theta_{RHT}| \lesssim 20°$ (dark) occupy most of the map area.

The highest values of p_d (panel f) are in the region of the striations. The *Planck* polarized intensity peak coincides with the brightest part of this map at ($126°, +27°$) (see figure A.1 in Planck Collaboration XX 2015b). The second, but lower, local maximum in p_d is in region B. The spatial variation of p_d resembles that of N_{stars}. This correlation is evident in Fig. 5 (top left), where the average value of N_{stars} is plotted for each (equally populated with pixels) p_d bin. This correlation is natural, as the polarization measurements were selected in Paper I to satisfy $p_d/\sigma_p \geq 2.5$. Because the observational errors σ_p are uniform across the field (Paper I), it is more likely that a larger number of significant measurements will be obtained in regions of higher p_d.

Additional support for the fact that the variation in the number of significant polarization measurements is uncorrelated with the column density is given by the plot in the top-right panel of Fig. 5, where the visual extinction A_V (from the map of Cambrésy et al. 2001) is plotted against p_d (from panel f of Fig. 4). One possibility that explains the observed variation of N_{stars} is that the three-dimensional (3D) orientation of the magnetic field varies significantly throughout the sky. If this were true, then we would expect more significant polarization to be detected in regions where the field is mostly on the plane of the sky. In these regions, p_d should be higher and this is consistent with the correlation of p_d and N_{stars} that we find. Also, if the field strength is more significant than turbulent gas motions, which tend to randomize its orientation (see Section 2.5), regions where B_{pos} is stronger (high p_d, N_{stars}) should have a small angle scatter. This is indeed the case, as can be seen in the bottom-right panel of Fig. 5. However, a significant contribution to this trend is likely to be coming from the larger measurement error of lower-significance measurements (near the cut of $p_d/\sigma_p \geq 2.5$).

If the assumption of a strong magnetic field holds, then diffuse, non-self-gravitating filaments such as the ones in this cloud are expected to be mostly parallel to the 3D field orientation. So, if the field lies mostly on the plane of the sky, the alignment of the projected field and filaments will be easily detected. However, if the field is mostly along the line of sight, then filaments and field can be observed as having any relative orientation. A hint of such a trend may exist in the bottom-left panel of Fig. 5. Planck Collaboration XXXII (2016a) find this exact trend (their fig. 13) and attribute it to the same effect: the projection of the 3D field on the sky. The anticorrelation of p_d with std(θ) is also observed (fig. 21 of Planck Collaboration XIX 2015a).

Planck Collaboration XXXII (2016a) also find that the degree of alignment decreases with column density in the range $N_H = [10^{20}, 10^{22}]$ cm^{-2}. In contrast to this, it is evident even visually that panels (b) and (e) in Fig. 4 are uncorrelated – we see no sign of such a trend. It is possible that the range of column densities in the Polaris Flare is significantly different than that in Planck Collaboration XXXII (2016a). To investigate whether this is the case, we convert the range of A_V in the Polaris Flare to N_H using the standard relation of Bohlin, Savage & Drake (1978): $N_H = 1.9 \times 10^{21} A_V$ (cm^{-2} mag^{-1}). From the A_V map of Cambrésy et al. (2001), values in the cloud vary within $A_V = [0.2, 1.2]$ mag $\Rightarrow N_H = [0.4, 2.3] \times 10^{21}$ cm^{-2}. Because the Cambrésy et al. (2001) data have a low resolution (8 arcmin), this range might be underestimated. Indeed, the cores in MCLD123 have $N_H \sim 10^{22}$ cm^{-2}. Therefore, the range of N_H in the cloud is comparable to that of Planck Collaboration XXXII (2016a), who infer that the anticorrelation of alignment with column density is most likely due to the existence of
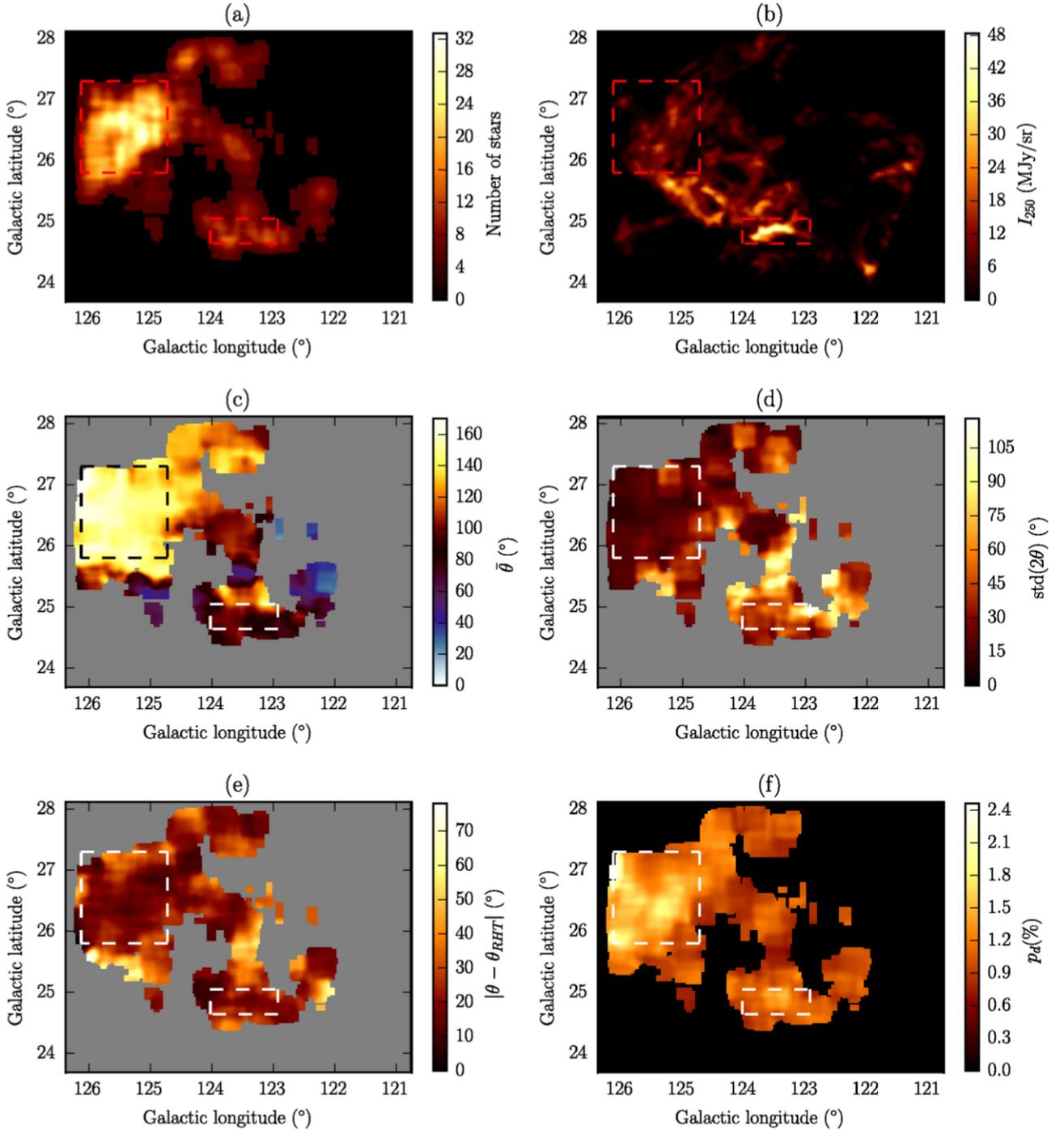
Figure 4. Quantities smoothed on a 5×5 arcmin^2 grid: (a) number of stellar polarization measurements; (b) *Herschel* 250-μm intensity; (c) polarization angle; (d) polarization angle scatter; (e) relative orientation of B_{pos} and filaments; (f) fractional linear polarization. Rectangles outline regions A and B.

molecular cloud structures that are perpendicular to the magnetic field. The only available explanation for this observation is that matter in magnetically dominated self-gravitating clouds collapses preferentially along field lines, producing structures that are elongated and perpendicular to the field. If we accept this reasoning, then it should not come as a surprise that we do not find such a trend in the gravitationally unbound Polaris Flare.

In summary, the above correlations seem to indicate the presence of a strong magnetic field in the cloud, which might change orientation from being mostly parallel to the plane-of-the-sky in region A to being more inclined in other areas.

2.3 Filament widths

An important morphological characteristic of filaments is their width. We use the Filament Trait-Evaluated Reconstruction (FᴉʟᴛᴇR) method[4] (Panopoulou et al. 2014) to construct the width distribution of filaments in the *Herschel* image. FᴉʟᴛᴇR takes as input the skeleton of an image and finds the width of the elongated structures. For this purpose, a Gaussian is fit to the radial profile at every point along the filament axis, and the resulting FWHM is deconvolved by the

---

[4] The code is available at https://bitbucket.org/ginpan/filter.
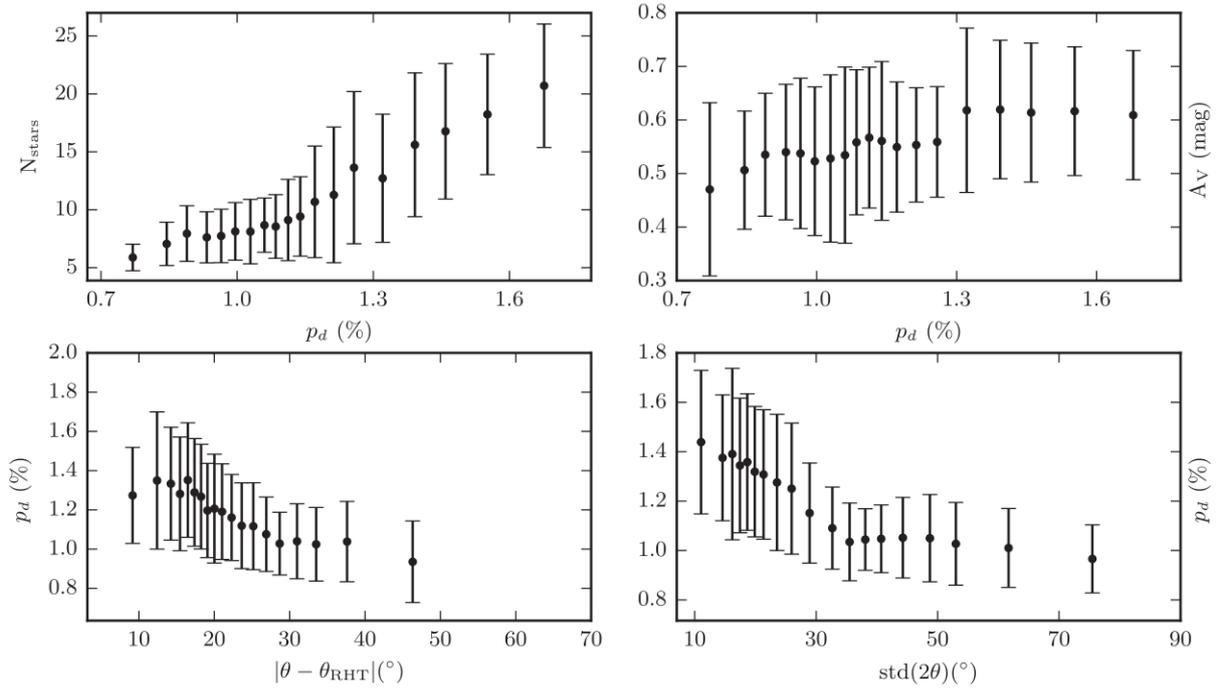
Figure 5. Binned pixel-to-pixel comparison of maps from Fig. 4: top left, N_{stars} versus p_d; top right, extinction A_V versus p_d; bottom left, p_d versus $|\theta - \theta_{RHT}|$; bottom right, p_d versus std(θ). Error bars show the $\pm 1\sigma$ from the mean in each bin. Bins contain the same number of pixels.
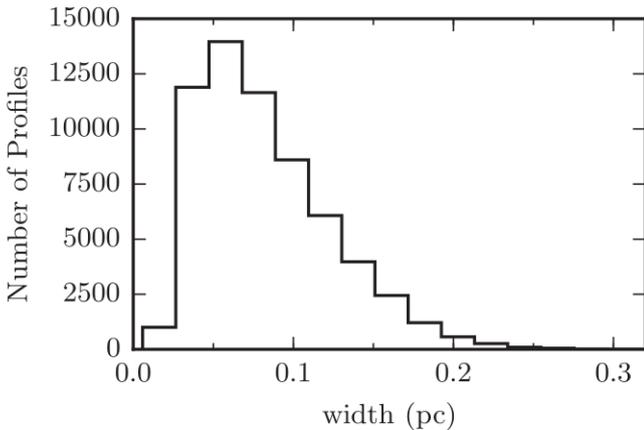
Figure 6. Distribution of widths along filaments in the *Herschel* image.
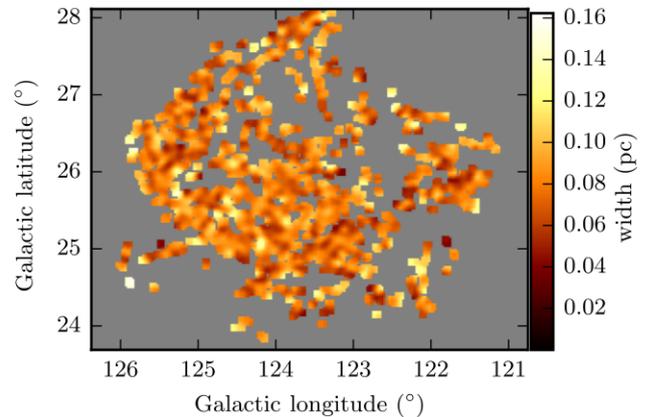
Figure 7. Map of filament widths found with FILTER, smoothed with a 5-arcmin boxcar filter.

beam size. The skeleton is produced by DISPERSE (Sousbie 2011), which is a topological code that can extract the filamentary structures of an image. It is designed to connect local maxima (cores). This property renders the construction of a representative skeleton difficult, because a significant part of the Polaris Flare does not contain bright cores. As seen in Fig. 2, the RHT produces a visualization of filamentary structures irrespective of brightness. This enables us to apply DISPERSE to the RHT backprojection image and to obtain a representative skeleton of the *Herschel* image to use as input to FILTER.

The distribution of filament widths in the *Herschel* image is shown in Fig. 6. The distribution has a peak at 0.06 pc and a spread of $\sigma_w = 0.04$, twice as much as the typical error in the width determination (σ_{fit}) in our implementation of the code. The intrinsic spread of the distribution is $\sigma_{int} = (\sigma_w^2 - \sigma_{fit}^2)^{1/2} = 0.035$ pc. Although lower than the characteristic width of 0.1 pc (e.g. Arzouma-

nian et al. 2011; Koch & Rosolowsky 2015), the peak value found here falls within the spread of the distributions from these works.

We investigate whether there are trends in the distribution of widths across the cloud, by constructing a smoothed map of the widths found by FILTER (Fig. 7). We use a boxcar filter of the same size as the maps in Fig. 4 (5 arcmin, or 0.2 pc) to allow for a better visual comparison. The map shows fluctuations in the width of filaments that do not appear to have any large-scale systematic trend. This remains the case for maps with smaller smoothing kernels. However, when comparing the distribution of widths within region A (Fig. 8, left, dotted red line) to that of the rest of the map (solid black line), we find that the former is slightly shifted towards lower values. A Kolmogorov–Smirnov (KS) test rejects the hypothesis that the two originate from the same parent distribution at the 0.001 level. In constructing the distributions, we discard structures with lengths less than 0.2 pc, as these have aspect ratios that are too small
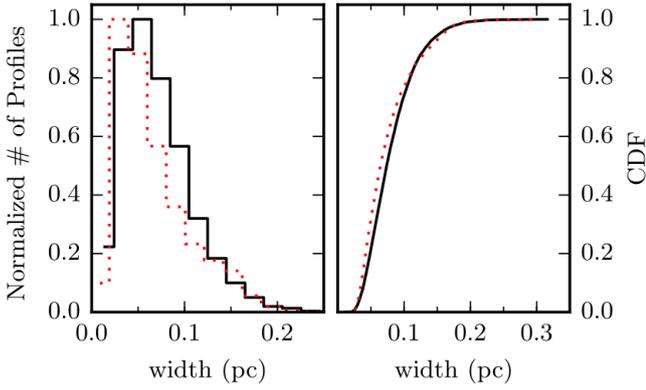
Figure 8. Left: normalized distribution of widths found with FILTER in the entire map (solid black) and in region A (dotted red) for all structures longer than 0.2 pc. Right: CDF of the same distributions.

to be considered filamentary. There is an indication that the shift towards lower widths becomes more pronounced as we raise this threshold to 0.4 pc.

2.4 Analysis of regions A (striations) and B (MCLD123)

Having explored the various observed properties of the cloud and their variation across the map, we now focus on the two regions of interest defined in Fig. 1.

2.4.1 Region A (striations)

Region A contains striking features both in dust emission (see the appendix of Miville-Deschênes et al. 2010) and in polarization (Fig. 1). Both B$_{pos}$ and striation orientations throughout the area are ordered. This is apparent in the distribution of polarization angles shown in panel (a) of Fig. 9. The distribution of θ resembles a normal distribution with a mean at $-20°$ and a standard deviation of $\delta\theta_{obs} = 11°$. The mean observational error (panel b) is $7°.6$, while the 80th percentile of the distribution is $10°$. Therefore, a significant contribution to the observed spread is due to the measurement error.

In addition to this uniformity, the mean directions of the field and dust structures appear to be aligned and this occurs to a greater extent than in the rest of the map. This is supported by the comparison of the normalized cumulative distribution functions (CDFs) of $|\theta - \theta_{RHT}|$ shown in Fig. 9, panel (c). Inside the region (dashed red line) 75 per cent of the differences $|\theta - \theta_{RHT}|$ lie in the range $[0°, 30°]$, whereas outside (solid black) only 63 per cent are in the same range.

Another characteristic of region A is that it exhibits a higher fractional linear polarization than the rest of the map, as seen in panel (f) of Fig. 4. We compare the distribution of p_d in region A (filled red) and in the rest of the map (black empty) in panel (d) of Fig. 9. It is clear that p_d in the region extends to higher values than out of the area, and that the mean p_d (dashed line, out; dotted line, in) is lower outside the region.

2.4.2 Region B (MCLD123)

Region B shows a different picture than region A. In this area, which is the densest part of the cloud, the plane-of-the-sky field seems to bend along the MCLD123 filament. The left panel of Fig. 10 shows the distribution of θ for this region while the right panel shows the distribution of relative orientations, $|\theta - \theta_{RHT}|$, for region B (filled red) and the rest of the map (empty black). The mean of the
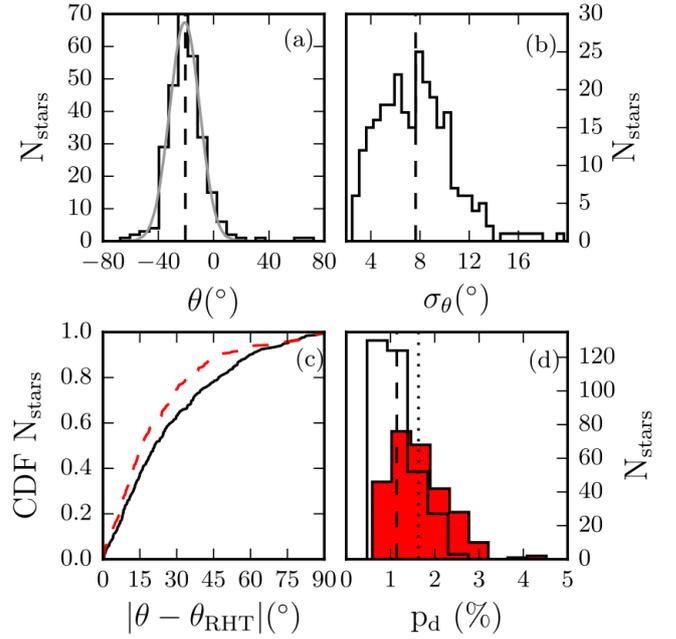
Figure 9. (a) Polarization angle distribution in region A (black solid), Gaussian fit (grey), average (dashed). (b) Distribution of polarization angle measurement errors in region A (solid) and mean (dashed). (c) Normalized CDFs of relative orientations of polarization measurements and dust striations in region A (dashed red) and the rest of the map (solid black). (d) Distributions of p_d in region A (filled red) and the rest of the map (empty black); dashed and dotted lines are their average values.
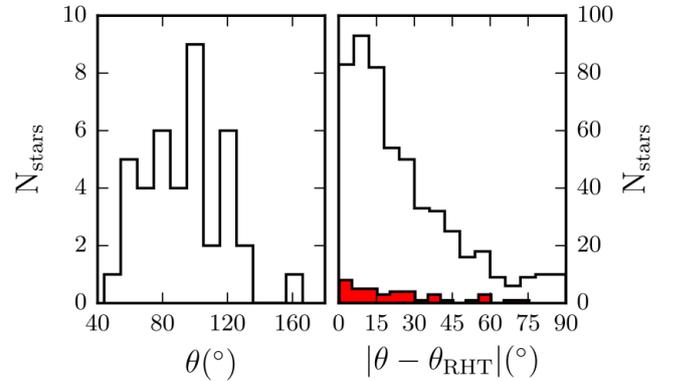
Figure 10. Left: distribution of polarization angles in region B. Right: distribution of $|\theta - \theta_{RHT}|$ for region B (filled red) and the rest of the map (empty black).

distribution of θ is $90°$, and the standard deviation is $25°$. The spread is partly due to the large-scale curvature of B$_{pos}$ in the vicinity and on the MCLD123 filament. The values of $|\theta - \theta_{RHT}|$ show a slight preference for alignment, although they extend to angles consistent with orthogonality.

2.5 Magnetic field strength and comparison to turbulence

The role of the magnetic field in the two regions discussed above can be investigated further by estimating the strength of the plane-of-the-sky magnetic field and by comparing the magnetic energy to that of turbulent motions.

Polarization measurements can be used to estimate the strength of $B_{\rm pos}$ under the assumption that the polarization angle dispersion ($\delta\theta$) is caused by the action of hydromagnetic waves perpendicular to the (mean) magnetic field (Davis 1951; Chandrasekhar & Fermi 1953). Based on the idea that a strong field will resist distortion and therefore $\delta\theta$ will be small, Davis (1951) and Chandrasekhar & Fermi (1953) derive

$$B_{\rm pos} \approx \sqrt{4\pi\rho}\,\frac{\delta v}{\delta\theta}, \tag{3}$$

where ρ is the volume mass density of the gas and δv is the velocity dispersion perpendicular to the observed field (along the line of sight). The last quantity, $\delta\theta$, can be expressed as the ratio of the (root-mean-squared) turbulent component of the magnetic field ($\langle B_{\rm t}^2 \rangle^{1/2}$) to the ordered component (B_0)(Hildebrand et al. 2009):

$$\delta\theta \approx \frac{\langle B_{\rm t}^2 \rangle^{1/2}}{B_0}. \tag{4}$$

2.5.1 Turbulent-to-ordered field ratio

Following Hildebrand et al. (2009), an estimate of the relative strength of B_0 with respect to $\langle B_{\rm t}^2 \rangle^{1/2}$ can be obtained by calculating the dispersion function of the polarization angles, defined as

$$\langle \Delta\theta^2(l) \rangle_{\rm tot} = \frac{1}{N(l)} \sum_{i=1}^{N(l)} \Delta\theta_i^2(l), \tag{5}$$

where the angle differences of all (unique) pairs of polarization measurements, $\Delta\theta_i(l)$, are binned according to the angular distance l in bins containing $N(l)$ pairs. The angle difference of the ith pair is simply the difference between the polarization angle measured at the position x_i and that at $x_i + l$: $\Delta\theta_i(l) = \theta(x_i) - \theta(x_i + l)$. We constrain $\Delta\theta_i(l) \in [0°, 90°]$. The dispersion function, corrected for the scatter induced by measurement errors ($\sigma_{\rm M}$) is expected to follow

$$\langle \Delta\theta^2(l) \rangle_{\rm tot} - \sigma_{\rm M}^2 \simeq m^2 l^2 + b^2(1 - e^{-l^2/2\delta^2}), \tag{6}$$

as shown by Houde et al. (2009) – their equation (44) adapted for optical polarimetry data by Franco, Alves & Girart (2010). In equation (6), δ is the correlation length of $B_{\rm t}$, b and m are constants of proportionality and $\sigma_{\rm M}^2(l)$ is found according to

$$\sigma_{\rm M}^2(l) = \frac{1}{N(l)} \sum_{i=1}^{N(l)} \sigma_{\Delta\theta_i(l)}^2, \tag{7}$$

where $\sigma_{\Delta\theta_i(l)}$ results from error propagation. Equation (6) is expected to hold for distances smaller than the typical scale (d) for large-scale variations in B_0. The parameter b is related to the ratio of the rms $B_{\rm t}$ to B_0 by

$$b^2 = \frac{2}{\mathcal{N}} \frac{\langle B_{\rm t}^2 \rangle}{B_0^2}, \tag{8}$$

where $\mathcal{N}$ is the number of turbulent cells along the line of sight,

$$\mathcal{N} \simeq \frac{s_{\rm los}}{\sqrt{2\pi}\delta}, \tag{9}$$

and $s_{\rm los}$ is the line-of-sight dimension of the cloud.

We implement the method of Hildebrand et al. (2009) and Houde et al. (2009) – hereafter the H09 method – in regions A and B. We calculate the dispersion function $\langle \Delta\theta^2(l) \rangle_{\rm tot}$, as explained above, we correct it to obtain the left side of equation (6) and we fit the function

on the right side of equation (6) to these values with respect to l^2. The fit takes into account the error of $\langle \Delta\theta^2(l) \rangle_{\rm tot}$. In Fig. 11, we plot $\langle \Delta\theta^2(l) \rangle_{\rm tot} - \sigma_{\rm M}^2$ with distance l, for each region (black solid lines). The black dots in Fig. 11 show the values used for the fit. The fits $p(l) = m^2 l^2 + b^2(1 - e^{-l^2/2\delta^2})$ are shown with red dashed lines. The distances are shown on a logarithmic scale (the bins used for fitting were linear). The bin size in region B (1.5 arcmin) was chosen so that there were more than 10 points per bin (in the fitting range). The bin size (1.7 arcmin) for region A was the minimum that produced a positive value of $\langle \Delta\theta^2(l) \rangle_{\rm tot} - \sigma_{\rm M}^2$ for the first bin. A choice of bin size larger by up to 38 per cent in region A, and 33 per cent in region B, produces values of b and δ within the error of the fit. The fits were done considering only distances smaller than the scale at which $B_{\rm pos}$ varies ($l < d$). In region A, we performed the fits up to $l \approx 20$ arcmin. In region B, we fit the data up to $l \approx 13$ arcmin. The choice of d is that which permits the maximum number of bins to be used in the fit while providing a fit that traces the exponential cut-off as well as possible. In region A, both b and δ remain within the error of the fit for a choice of d in the range 8–25 arcmin. The same holds for region B in the range 9–13 arcmin.

The results of the fits are shown in the top left of the panels in Fig. 11. The correlation length of $B_{\rm t}$ is not well constrained, as it is only in the first bin of region A that the effect of the exponential decay in equation (8) is apparent. The values for δ obtained for both regions are consistent within the errors of the fits. Inserting the values for b and δ from the fits into equation (8) we obtain estimates for the ratio $\langle B_{\rm t}^2 \rangle^{1/2}/B_0$: 0.2–0.5 for region A and 0.3–0.8 for region B. The line-of-sight depth of each region used for these estimates is presented and discussed in the next section.

Within our adopted uncertainties, the ratios in both regions are less than 1. This indicates that the magnetic field is much stronger than the turbulent component in region A and, at most, comparable to the turbulent component in region B. Moreover, equation (3) can be written as

$$\frac{\langle B_{\rm t}^2 \rangle^{1/2}}{B_0} \simeq \frac{\delta v}{v_{\rm A}} \tag{10}$$

(Hildebrand et al. 2009), where $v_{\rm A} = B_0/\sqrt{4\pi\rho}$ is the Alfvén speed and δv is the velocity dispersion perpendicular to the mean field. From this we can conclude that turbulent motions are most likely sub-Alfvénic in region A and could be sub- to trans-Alfvénic in region B. This is consistent with the conclusion of Hily-Blant & Falgarone (2007) that the magnetic field is dynamically important in region B. Hily-Blant & Falgarone (2007) found that motions in MCLD123 are trans-Alfvénic, using the dispersion of position angles of diffuse ^{12}CO filaments.

2.5.2 Strength of the ordered component

Having inferred the value of $\delta\theta$ from the H09 method, we now move on to find the values of the remaining quantities that enter into equation (3) and we use them to obtain an estimate for $B_{\rm pos}$ in both regions. Table 1 presents the values used in obtaining these estimates.

The gas mass density is equal to $\rho = \mu m_{\rm H} n_{\rm H}$, where $m_{\rm H}$ is the mass of the hydrogen atom, $\mu = 1.36$ is a factor that accounts for the fraction of helium and $n_{\rm H}$ is the total hydrogen number density. The total $n_{\rm H}$ must be used and not $n_{\rm H_2}$ because even though the cloud is molecular, the fraction of gas that is in atomic form might be important ($N_{\rm H_I} \sim N_{\rm H_2}$; Hily-Blant & Falgarone 2007). To estimate the density in region B, we assume that MCLD123 has a cylindrical geometry. This implies a line-of-sight dimension
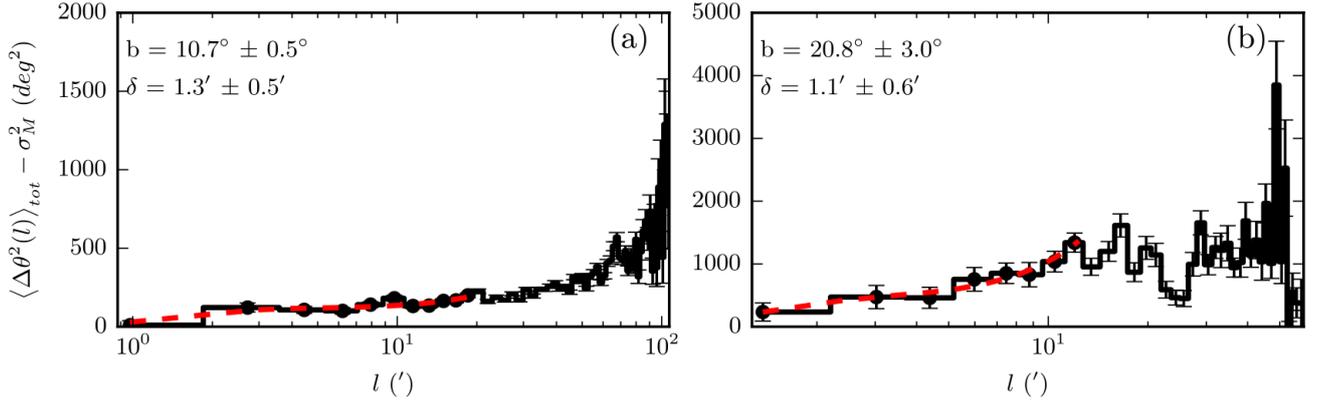
Figure 11. The dispersion function (corrected for measurement errors) versus angular distance, l, for regions A (left) and B (right). The red dashed line shows the best-fitting function of the form $\langle \Delta\theta^2(l) \rangle_{\mathrm{tot}} - \sigma_{\mathrm{M}}^2 = m^2 l^2 + b^2(1 - e^{-l^2/2\delta^2})$. The black dots show the data points that were used in the fits. The fit results for b and δ are shown in the top left.

Table 1. Values used for estimation of B_{pos} in regions A and B: ΔV, FWHM of CO ($J = 1$–0) line; A_{V}, average visual extinction (Cambrésy et al. 2001); N_{H}, hydrogen column density; s_{los}, line-of-sight dimension; n_{H}, hydrogen number density; $\delta\theta^{\mathrm{H09}}$, polarization angle dispersion from the H09 method (equation 4); $\delta\theta$, polarization angle dispersion from Section 2.4.1 (corrected for measurement error according to equation 11); $\langle B_{\mathrm{t}}^2 \rangle^{1/2}/B_0$, turbulent-to-ordered field ratio from the H09 method; $B_{\mathrm{pos}}^{\mathrm{H09}}$, plane-of-sky magnetic field using $\delta\theta^{\mathrm{H09}}$ and equation (3); $B_{\mathrm{pos}}^{\mathrm{mDCF}}$, plane-of-sky magnetic field using $\delta\theta$ and the modified equation (3) as explained in the text.

Region	ΔV (km s^{-1})	A_{V} (mag)	N_{H} 10^{20} (cm^{-2})	s_{los} (pc)	n_{H} (cm^{-3})	$\delta\theta^{\mathrm{H09}}$ ($^\circ$)	$\delta\theta$ ($^\circ$)	$\sqrt{\langle B_{\mathrm{t}}^2 \rangle}/B_0$	$B_{\mathrm{pos}}^{\mathrm{H09}}$ (μG)	$B_{\mathrm{pos}}^{\mathrm{mDCF}}$ (μG)
A	3.1	0.6	12	0.4–1.3	300–1000	10°–29°	8	0.2–0.5	24–120	43–81
B	2.6	0.7	24	0.25–0.5	1500–3100	17°–44°		0.3–0.8	30–111	

of ∼0.25–0.5 pc, where the lower bound is twice the observed extent of the dense part of the filament and the upper bound is found to include the more diffuse parts. The average N_{H_2} from the map of André et al. (2010) is 8×10^{20} cm^{-2}, corresponding to $N_{\mathrm{H}} \sim 2.4 \times 10^{21}$ cm^{-2}. Dividing by the assumed line-of-sight dimension gives $n_{\mathrm{H}} \simeq 1500$–3100 cm^{-3} (see also Grossmann et al. 1990).

We can obtain a loose constraint on the mean density of region A by arguing that it is likely to be less than that of region B (as the latter contains cores). An upper bound would therefore be $n_{\mathrm{H}}^{\mathrm{A}} < n_{\mathrm{H}}^{\mathrm{B}}$. A lower limit on the density can be estimated by considering existing measurements of n_{H} from ultraviolet data of stars in diffuse sightlines. A set of measurements from various works has been collected by Goldsmith (2013) who shows that most sightlines with $N_{\mathrm{H}} \gtrsim 10^{21}$ cm^{-2} $\Rightarrow N_{\mathrm{H}_2} \gtrsim 3 \times 10^{20}$ cm^{-2} have measured densities: $300 \gtrsim n_{\mathrm{H}} \gtrsim 60$ cm^{-3} (assuming $N_{\mathrm{H}1} \simeq N_{\mathrm{H}_2}$). The column density in region A is estimated[5] by $N_{\mathrm{H}}^{\mathrm{A}} \simeq N_{\mathrm{H}}^{\mathrm{B}} I_{250}^{\mathrm{A}}/I_{250}^{\mathrm{B}} \simeq 1.2 \times 10^{21}$ cm^{-2}, where we have assumed that the temperature distribution is quasi-uniform throughout the cloud (Men'shchikov et al. 2010; Schneider et al. 2013) so that intensity (I_{250}) variations in the *Herschel* image are mostly caused by N_{H} fluctuations. Because the Polaris Flare is a molecular cloud, we reason that $n_{\mathrm{H}}^{\mathrm{A}} > 300$ cm^{-3} (the upper limit from the aforementioned sightlines) is an appropriate approximation. The line-of-sight dimension of region A is then ($s_{\mathrm{los}} = n_{\mathrm{H}}^{\mathrm{A}}/N_{\mathrm{H}}^{\mathrm{A}}$) $1.3 \gtrsim s_{\mathrm{los}} \gtrsim 0.2$ pc. The upper limit is approximately one-third of

the size of the region as projected on the sky, while the lower limit is similar to the assumed s_{los} in region B. We expect that the true s_{los} lies mostly near the lower limit of this range because, as a result of the translucent nature of the cloud, the line-of-sight dimension should not be very large. Studies of cirrus clouds in general find a high likelihood of them being sheet-like (e.g. Gillmon & Shull 2006). Along with the fact that regions A and B have similar mean A_{V} (Table 1), this implies that s_{los} in the two regions should not vary by orders of magnitude.

To estimate the velocity dispersion δv, we use the ^{12}CO ($J = 1$–0) data from the survey of Dame, Hartmann & Thaddeus (2001).[6] The data, first presented by Heithausen et al. (1993), cover 134 deg^2 including the *Herschel*-mapped area. The angular resolution is 8.7 arcmin and the spectral resolution is 0.65 km s^{-1}. We fit a Gaussian to the mean spectrum of each region and relate its FWHM (ΔV) to the velocity dispersion (δv) with $\delta v = \Delta V/(2\sqrt{2 \ln 2})$. Complications can arise when ^{12}CO ($J = 1$–0) is used to estimate the velocity dispersion if the line is optically thick. However, Hily-Blant & Falgarone (2007) found that the ^{12}CO ($J = 1$–0) line is optically thin in diffuse gas within the MCLD123 filament with column density derived from the scaling of CO to ^{13}CO velocity-integrated line temperatures: $N_{\mathrm{H}_2} \sim 10^{20}$ cm^{-2}. Because the mean column density in region A is $N_{\mathrm{H}_2} \approx 4 \times 10^{20}$ cm^{-2} ($N_{\mathrm{H}1} \approx N_{\mathrm{H}_2}$) this indicates that the line might also be optically thin within region A. The line is most likely optically thick in the densest parts of region B; however, these occupy a very small fraction of the area considered.

---

[5] This is consistent with the value obtained by converting the mean A_{V} to N_{H} according to Bohlin et al. (1978): $N_{\mathrm{H}} = 1.9 \times 10^{21} A_{\mathrm{V}}$ (cm^{-2} mag^{-1}) for $R_{\mathrm{V}} = 3.1$ (e.g. Savage & Mathis 1979).

[6] Survey online archive can be found at https://www.cfa.harvard.edu/rtdc/CO/IndividualSurveys/.

The results that follow from equation (3) are presented in Table 1. We show the entire range of values, given the possible variation in the estimated quantities. The range arises from two factors: the error on δ and the estimate of s_{los}, which enters both in the estimation of the density ρ and in the dispersion of polarization angles from the H09 method. The B_{pos} estimates between regions A and B are very similar.

Hily-Blant & Falgarone (2007) obtained an estimate of $B \simeq 15\ \mu G$ for a smaller part of region B, using the angle dispersion of filaments seen in ^{12}CO. This value is 50 per cent that of the lowest bound of our estimate.

2.5.3 B_{pos} with alternative estimate of $\delta\theta$

We can obtain an alternative estimate of B_{pos} by using the observed angular dispersion $\delta\theta_{obs}$ found in Section 2.4.1 from the Gaussian fit to the distribution of polarization angles (see, for example, section 4.2.3 of Barnes et al. 2015). Ostriker et al. (2001) applied the method of Davis (1951) and Chandrasekhar & Fermi (1953) to numerical simulations of MHD turbulence using this type of angle dispersion calculation and found that the method provides a good estimate of B_{pos} when $\delta\theta \lesssim 25°$. They introduced a factor f in equation (3) to correct for line-of-sight averaging: $B_{pos} = f\sqrt{4\pi\rho}\ \delta v/\delta\theta$ and proposed $f \approx 0.5$.

We use this modification of equation (3) with $\delta\theta_{obs}$ to obtain another estimate of B_{pos} in region A. Because the errors in polarization angle (σ_θ) add to the intrinsic angle dispersion of the cloud, $\delta\theta$, we correct for this bias by (e.g. Crutcher et al. 2004; Girart, Rao & Marrone 2006):

$$\delta\theta^2 = \delta\theta_{obs}^2 - \bar{\sigma}_\theta^2, \tag{11}$$

where $\bar{\sigma}_\theta$ is the mean polarization angle error.

The values for the magnetic field strength are shown in the last column of Table 1. They lie within the range of values found using the angle dispersion from H09 and the original equation (3).

3 DISCUSSION

3.1 Properties of the three-dimensional magnetic field

The projected magnetic field of the cloud presents a very inhomogeneous structure. There are regions where it is uniform and others where the measured orientations appear random, or significant measurements are entirely absent. These characteristics may provide hints on the nature of the 3D field. Let us consider region A, which has the largest density of significant polarization measurements. As discussed in Paper I, this is not due to variation in stellar density, observing conditions or other systematics. Therefore, region A must be characterized by higher polarization efficiency – in the terminology of Andersson, Lazarian & Vaillancourt (2015), intrinsic polarization per unit column density. We can further investigate this observation by considering that p_d is related to the following factors (Lee & Draine 1985):

$$p_d = p_0 R F \cos^2\gamma. \tag{12}$$

Here, γ is the inclination angle (the angle between the magnetic field and the plane of the sky), p_0 reflects the polarizing capability of the dust grains due to their geometric and chemical characteristics and R is the Rayleigh reduction factor (Greenberg 1968), which quantifies the degree of alignment of the grains with the magnetic field. F accounts for the variation of the field orientation along the line of

sight and is equal to $F = (3/2)[\langle\cos^2\chi\rangle - (1/3)]$, where χ is the angle between the direction of the field at any point along the line of sight and the mean field direction. The angular brackets denote an average along the line of sight. The increased p_d of region A could therefore be the result of any of these factors (or some combination of them). In other words, region A could have the following:

(i) increased alignment efficiency (e.g. more background radiation, a larger amount of asymmetric dust grains, larger grain sizes), that is, higher factors p_0 and/or R;

(ii) more uniform magnetic field along the line of sight, that is, higher F;

(iii) increased B_{pos} (inclination of B is larger with respect to the line of sight), that is, higher $\cos\gamma$.

Several pieces of evidence challenge the validity of case (i). First, if the radiation illuminating region A were very different in intensity or direction, then the dust temperature of the area would have to be qualitatively different (higher) than in other regions of the cloud. As mentioned in Section 2.5, the results from Men'shchikov et al. (2010) imply that temperature and density variations are subtle across the field. Indeed, the temperature probability distribution function presented by Schneider et al. (2013) is narrow. Also, the most likely candidate for providing illumination to the cloud, because of its likely proximity, is Polaris (the star). By studying optical and 100-μm light from MCLD123, Zagury et al. (1999) concluded that the star cannot be the primary source of dust heating. Additionally, larger amounts of (aligned) grains would imply larger column densities (or A_V) than the rest of the cloud, which is not a characteristic of region A. To the best of our knowledge, there is no evidence for significant variation of grain size within the same cloud between regions of such similar A_V.

We now investigate whether the observed difference in p_d between region A and other parts of the cloud could arise from differences in the properties of the magnetic field along the line of sight. We can obtain an upper limit on the influence of the factor F on p_d by keeping all other factors in equation (12) constant and taking the ratio of two regions (e.g. A and B):

$$\frac{p_A}{p_B} \approx \frac{\langle\cos^2\chi_A\rangle - (1/3)}{\langle\cos^2\chi_B\rangle - (1/3)}. \tag{13}$$

Here, the average p_d in regions A and B are equal to $p_A = 1.63$, $p_B = 1.3$ and $\langle\cos^2\chi_i\rangle$ ($i = A, B$) is an average over all lines of sight in region i. For region A, the angle dispersion is small ($\delta\theta \sim 10°$; Section 2.4), so we can make the approximation $\langle\cos^2\chi_A\rangle \approx \cos^2 10°$ (to better than 10 per cent). We check what values of $\langle\cos^2\chi_B\rangle$ produce the observed ratio of p_A/p_B (within 30 per cent) by drawing $\mathcal{N} = 1–9$ angles (the number of turbulent cells in region B) from a normal distribution with $\sigma = 10°–50°$. After repeating the process 100 times, we find that the most likely σ that can reproduce the observed p_A/p_B are in the range $10°–25°$, similar to the observed angle dispersion on the plane of the sky (Section 2.5). Therefore, it is possible that region A has a more ordered field along the line of sight compared to other regions.

Finally, if the 3D orientation of the magnetic field is mostly in the plane of the sky in region A and less so in other parts of the cloud, this could also explain the increased measurement density in this region. We can estimate the change in angle that is needed to obtain the difference in p_d between regions A and B, from equation (12). Taking all factors equal between the two regions except the inclination angle, the ratio of p_d is $p_d^A/p_d^B = 1.63/1.3 = \cos^2\gamma_A/\cos^2\gamma_B$. This ratio could arise either from a pair of large γ_A, γ_B with a small difference or from small angles having a large difference. This

Table 2. Distance estimates to the cloud from different references.

Reference	d (pc)	Method
Heithausen & Thaddeus (1990)	$\leq$240	Stellar extinction, nearby clouds
Zagury et al. (1999)	125 ± 25	Association to stars
Brunt et al. (2003)	205 ± 62	Size–linewidth relation
Schlafly et al. (2014)	390 ± 34	Stellar extinction

ambiguity can be avoided by considering the expected polarization angle dispersions for different inclinations of the magnetic field, studied with MHD simulations by Falceta-Gonçalves et al. (2008). In their work, these authors found that in the range $0°$–$60°$ the predicted polarization angle dispersions are below $35°$ for their model with a strong magnetic field (Alfvén Mach number 0.7). Because the angle dispersions in the two regions are significantly lower than this value, it is safe to assume that $0° < \gamma_A, \gamma_B < 60°$. For this range, we find that the observed ratio of p_d can be explained by inclination differences most likely in the range $\gamma_B - \gamma_A = 6°$–$30°$. In order to explain the difference in p_d between region A and the lowest mean-p_d region in the map (Fig. 4, panel f, approximately at the centre of the map) which has a $p_d \sim 0.7$ per cent, the difference in inclination angle needs to be $20°$–$50°$.

With the existing set of measurements, we are not able to conclude whether the variations in polarization fraction are mostly due to change in inclination or due to differences in the uniformity of the field along the line of sight. However, we have provided bounds on the areas of the parameter space in which these differences are likely to occur.

3.2 Cloud distance

In the literature, there is no definitive consensus on the cloud's distance. The existing estimates are shown in Table 2 along with the method that was used to obtain each one.

Heithausen & Thaddeus (1990) base their distance estimate on reddening estimates of stars in the field from Keenan & Babcock (1941), who found reddened stars from distances as close as 100 pc and found that all stars farther than 300 pc were reddened. Knowing that Polaris (the star) showed dust-induced polarization, and that the then existing distance estimates to the star were 109–240 pc, they placed the cloud at a distance $d < 240$ pc. This distance fits with the smooth merging of the cloud at lower latitudes with the Cepheus Flare, at 250 pc.

Zagury et al. (1999) compared *IRAS* 100-μm emission with optical images of MCLD123 and found that the brightness ratios are consistent with Polaris (the star) being the illuminating source of the cloud in the optical. They placed the cloud at a distance 6–25 pc in front of the star ($105 < d < 125$ pc from the Sun) so that its contribution in dust heating would be minimal compared to the interstellar radiation field.

Brunt et al. (2003) used principal component analysis (PCA) of spectral imaging data to infer distances based on the universality of the size–linewidth relation for molecular clouds. Their estimate is consistent with both the above estimates.

Schlafly et al. (2014) used accurate photometry measurements of the Panoramic Survey Telescope and Rapid Response System 1 (Pan-STARRS1) and calculated distances to most known molecular clouds. Their estimate for the distance of the Polaris Flare (390 pc),
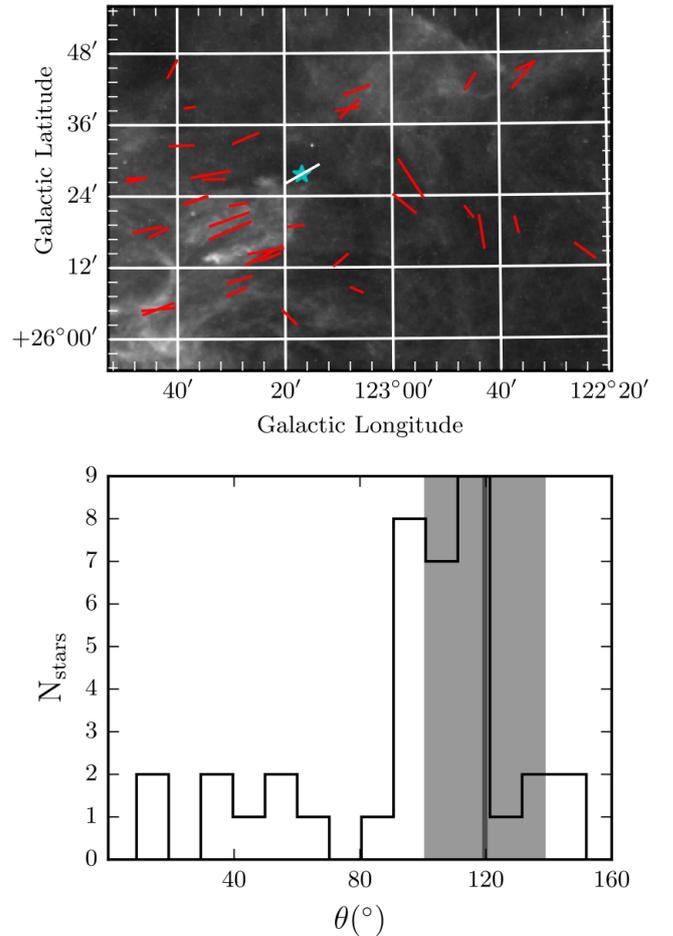
Figure 12. Top: polarization angle of the star Polaris (Heiles 2000), white segment, compared to our data, red segments. The p_d of Polaris is 0.1 per cent, but has been enhanced 10 times. Its position is marked with a star. Bottom: distribution of θ in the area shown in the top panel. The dark grey line shows the θ of Polaris while the grey band is the 1σ error. Bin size is $10°$.

was obtained for lines of sight in the outskirts of the cloud (outside our observed field).

In Fig. 12 (top), we zoom in on the region surrounding the North Star and overplot the polarization data (red) and the measurement of the North Star (white) from the Heiles (2000) catalogue on the *Herschel* image. The lengths of the segments are proportional to their p_d, and the length of the Heiles measurement has been enhanced 10 times. The position of the North Star is marked with a blue star. The star happens to be projected on an area of very little dust emission, hence the low p_d. Magnetic field orientations in the area show a strong peak around $110°$, with a few measurements (which happen to fall towards the right and bottom of the area) clustering around $40°$. This can be seen in the distribution of angles in the area shown in Fig. 12 (bottom). The polarization angle of the North Star (Heiles 2000) is shown with the dark grey vertical line and the light grey band shows the 1σ error. The stars that are nearest to Polaris, in projection, belong to the peak at $100°$. The fact that the orientation of the North Star's polarization is consistent with this peak is intriguing. It could add to the evidence supporting that Polaris is behind the Flare, constraining its distance to the Zagury et al. (1999) estimate. However, because the orientation of stellar polarization shifts by a substantial amount ($60°$) in $\sim$20 arcmin,

denser sampling of the area is needed in order to ascertain this indication.

4 SUMMARY

We have combined RoboPol optical polarization measurements and *Herschel* dust emission data to infer the magnetic field properties of the Polaris Flare. We have found that linear dust structures (filaments and striations) are preferentially aligned with the projected magnetic field. This alignment is more prominent in regions where the fractional linear polarization is highest (and the number of significant polarization measurements is largest). This correlation supports the idea that variations in the alignment are partly caused by the projection of the 3D magnetic field. We investigated the possibility of important spatial variations in the filament widths and found only a slight indication of such an effect. Using the Davis (1951), Chandrasekhar & Fermi (1953) and Hildebrand et al. (2009) methods, we estimated the strength of the plane-of-the-sky field and the ratio of turbulent-to-ordered field components in two regions of the cloud: one containing diffuse striations, and the other harbouring the highest column density filament. Our results indicate that the magnetic field is dynamically important in both regions. Combining our results, we find that differences of $6°–30°$ in the magnetic field inclination between two cloud regions can explain the observed polarization fraction differences. This difference can also be explained by a difference in the line-of-sight dispersion of the field of $10°–25°$. Finally, we find that the polarization angles of the North Star (Heiles 2000) and of RoboPol data in the surrounding area favour the scenario of the cloud being in front of the star.

REFERENCES

Alves F. O., Franco G. A. P., Girart J. M., 2008, A&A, 486, L13
Alves de Oliveira C. et al., 2014, A&A, 568, A98
Andersson B.-G., Lazarian A., Vaillancourt J. E., 2015, ARA&A, 53, 501
André P. et al., 2010, A&A, 518, L102
André P., Di Francesco J., Ward-Thompson D., Inutsuka S.-I., Pudritz R. E., Pineda J. E., 2014, in Beuther H., Klessen R. S., Dullemond C. P., Henning T., eds, Protostars and Planets VI. University of Arizona Press, Tucson, p. 27
Arzoumanian D. et al., 2011, A&A, 529, L6
Barnes P. et al., 2015, MNRAS, 453, 2622
Bensch F., Leuenhagen U., Stutzki J., Schieder R., 2003, ApJ, 591, 1013
Bohlin R. C., Savage B. D., Drake J. F., 1978, ApJ, 224, 132
Brunt C. M., Heyer M. H., Vázquez-Semadeni E., Pichardo B., 2003, ApJ, 595, 824
Cambrésy L., Boulanger F., Lagache G., Stepnik B., 2001, A&A, 375, 999
Chandrasekhar S., Fermi E., 1953, ApJ, 118, 113
Chapman N. L., Goldsmith P. F., Pineda J. L., Clemens D. P., Li D., Krčo M., 2011, ApJ, 741, 21
Clark S. E., Peek J. E. G., Putman M. E., 2014, ApJ, 789, 82
Crutcher R. M., Nutter D. J., Ward-Thompson D., Kirk J. M., 2004, ApJ, 600, 279
Dame T. M., Hartmann D., Thaddeus P., 2001, ApJ, 547, 792
Davis L., Jr, 1951, Phys. Rev., 81, 890
Falceta-Gonçalves D., Lazarian A., Kowal G., 2008, ApJ, 679, 537
Fiege J. D., Pudritz R. E., 2000, ApJ, 544, 830
Franco G. A. P., Alves F. O., 2015, ApJ, 807, 5
Franco G. A. P., Alves F. O., Girart J. M., 2010, ApJ, 723, 146
Gillmon K., Shull J. M., 2006, ApJ, 636, 908
Girart J. M., Rao R., Marrone D. P., 2006, Sci, 313, 812
Goldsmith P. F., 2013, ApJ, 774, 134
Goldsmith P. F. Heyer M., Narayanan G., Snell R., Li D., Brunt C., 2008, ApJ, 680, 428
Goodman A. A., Bastien P., Menard F., Myers P. C., 1990, ApJ, 359, 363
Gorbikov E., Brosch N., 2014, MNRAS, 443, 725
Greenberg J. M., 1968, in Middlehurst B. M., Aller L. H., eds, Nebulae and Interstellar Matter, Vol. 7. University of Chicago Press, Chicago, p. 221
Grossmann V., Heithausen A., Meyerdierks H., Mebold U., 1990, A&A, 240, 400
Hall J. S., 1955, in Swings P., ed., Liege Symposium. Institut d'Astrophysique, Cointe-Liege, p. 543
Heiles C., 2000, AJ, 119, 923
Heithausen A., 1999, A&A, 349, L53
Heithausen A., Thaddeus P., 1990, ApJ, 353, L49
Heithausen A., Stacy J. G., de Vries H. W., Mebold U., Thaddeus P., 1993, A&A, 268, 265
Heitsch F., Zweibel E. G., Mac Low M.-M., Li P., Norman M. L., 2001, ApJ, 561, 800
Hildebrand R. H., Kirby L., Dotson J. L., Houde M., Vaillancourt J. E., 2009, ApJ, 696, 567
Hily-Blant P., Falgarone E., 2007, A&A, 469, 173
Hily-Blant P., Falgarone E., 2009, A&A, 500, L29
Houde M., Vaillancourt J. E., Hildebrand R. H., Chitsazzadeh S., Kirby L., 2009, ApJ, 706, 1504
Keenan P. C., Babcock H. W., 1941, ApJ, 93, 64
Koch E. W., Rosolowsky E. W., 2015, MNRAS, 452, 3435
Lee H. M., Draine B. T., 1985, ApJ, 290, 211
Li H-B., Fang M., Henning T., Kainulainen J., 2013, MNRAS, 436, 3707
Malinen J. et al., 2016, MNRAS, 460, 1934
Matthews B. C., Wilson C. D., Fiege J. D., 2001, ApJ, 562, 400
Men'shchikov A. et al., 2010, A&A, 518, L103
Miville-Deschênes M.-A. et al., 2010, A&A, 518, L104
Mouschovias T. C., 1976, ApJ, 206, 753
Myers P. C., 2009, ApJ, 700, 1609
Nakamura F., Li Z-Y., 2008, ApJ, 687, 354
Ostriker E. C., Stone J. M., Gammie C. F., 2001, ApJ, 546, 980
Padoan P., Goodman A. A., Draine B. T., Juvela M., Nordland Å. R., Rögnvaldsson O. E., 2001, ApJ, 559, 1005
Palmeirim P. et al., 2013, A&A, 550, A38
Panopoulou G. V., Tassis K., Goldsmith P. F., Heyer M., 2014, MNRAS, 444, 2507
Panopoulou G. V. et al., 2015, MNRAS, 452, 715 (Paper I)
Pereyra A., Magalhães A. M., 2004, ApJ, 603, 584
Pilbratt G. L. et al., 2010, A&A, 518, L1
Planck Collaboration XIX, 2015a, A&A, 576, 104
Planck Collaboration XX, 2015b, A&A, 576, 105
Planck Collaboration XXXV, 2016b, A&A, 586, A138
Planck Collaboration XXXII, 2016a, A&A, 586, A135
Savage B. D., Mathis J. S., 1979, ARA&A, 17, 73

Schlafly E. F. et al., 2014, ApJ, 786, 29

Schlegel D. J., Finkbeiner D. P., Davis M., 1998, ApJ, 500, 525

Schneider N. et al., 2013, ApJ, 766, L17

Soler J. D., Hennebelle P., Martin P. G., Miville-Deschênes M.-A., Netterfield C. B., Fissel L. M., 2013, ApJ, 774, 128

Sousbie T., 2011, MNRAS, 414, 350

Sugitani K. et al., 2011, ApJ, 734, 63

van den Bergh S., 1956, Zeitschrift für Astrophysik, 40, 249

Wagle G. A., Troland T. H., Ferland G. J., Abel N. P., 2015, ApJ, 809, 17

Ward-Thompson D. et al., 2010, A&A, 518, L92

Zagury F., Boulanger F., Banchet V., 1999, A&A, 352, 645

This paper has been typeset from a TEX/LATEX file prepared by the author.

Chapter 5

Concluding remarks

State-of-the-art observations of cloud and magnetic field structure provide an important test for star formation theories. We have exploited such observations to measure observed properties of molecular clouds. Using Herschel dust emission images, we have shown that the filamentary morphology in molecular clouds is more complex than the proposed picture of a 'characteristic' filament width. In future works we shall concentrate in developing alternative and innovative tools for quantifying cloud structure, that can capture the full complexity that is observed.

The most recent observational results in dense, star-forming molecular clouds highlight the importance of the magnetic field in shaping structures and determining the evolution of clouds. Using optical polarimetry, we have shown that in translucent molecular clouds this is also the case. Motions in the Polaris Flare (measured from molecular line emission) are sub-alfvénic, consistent with the picture of strongly magnetized molecular clouds. Also consistent with this view is the observed alignment of filamentary dust emission structures with the magnetic field (as projected on the plane of the sky).

Our results add to a body of evidence supporting that star formation is controlled by magnetic fields from scales of entire molecular complexes down to the sizes of individual cores [Mouschovias and Ciolek, 1999].

Bibliography

F. O. Alves, G. A. P. Franco, and J. M. Girart. Optical polarimetry toward the Pipe nebula: revealing the importance of the magnetic field. *Astronomy & Astrophysics*, 486:L13–L16, Aug. 2008. doi: 10.1051/0004-6361:200810091.

B.-G. Andersson, A. Lazarian, and J. E. Vaillancourt. Interstellar Dust Grain Alignment. *Annual Review of Astronomy and Astrophysics*, 53:501–539, Aug. 2015. doi: 10.1146/annurev-astro-082214-122414.

P. André, A. Men'shchikov, S. Bontemps, V. Könyves, F. Motte, N. Schneider, P. Didelon, V. Minier, P. Saraceno, D. Ward-Thompson, and et al. From filamentary clouds to prestellar cores to the stellar IMF: Initial highlights from the Herschel Gould Belt Survey. *Astronomy and Astrophysics*, 518:L102, July 2010. doi: 10.1051/0004-6361/201014666.

P. André, J. Di Francesco, D. Ward-Thompson, S.-I. Inutsuka, R. E. Pudritz, and J. E. Pineda. From Filamentary Networks to Dense Cores in Molecular Clouds: Toward a New Paradigm for Star Formation. *Protostars and Planets VI*, pages 27–51, 2014. doi: 10.2458/azu_uapress_9780816531240-ch002.

D. Arzoumanian, P. André, P. Didelon, V. Könyves, N. Schneider, A. Men'shchikov, T. Sousbie, A. Zavagno, S. Bontemps, J. di Francesco, and et al. Characterizing interstellar filaments with Herschel in IC 5146. *Astronomy and Astrophysics*, 529:L6, May 2011. doi: 10.1051/0004-6361/201116596.

D. Arzoumanian, P. André, N. Peretto, and V. Könyves. Formation and evolution of interstellar filaments. Hints from velocity dispersion measurements. *Astronomy & Astrophysics*, 553:A119, May 2013. doi: 10.1051/0004-6361/201220822.

S. Auddy, S. Basu, and T. Kudoh. A Magnetic Ribbon Model for Star-forming Filaments. *The Astrophysical Journal*, 831:46, Nov. 2016. doi: 10.3847/0004-637X/831/1/46.

E. E. Barnard. On a nebulous groundwork in the constellation Taurus. *The Astrophysical Journal*, 25, Apr. 1907. doi: 10.1086/141434.

H. Beuther, H. Linz, J. Tackenberg, T. Henning, O. Krause, S. Ragan, M. Nielbock, R. Launhardt, S. Bihr, A. Schmiedeke, R. Smith, and T. Sakai. Fragmentation and dynamical collapse of the starless high-mass star-forming region IRDC 18310-4. *Astronomy & Astrophysics*, 553:A115, May 2013. doi: 10.1051/0004-6361/201220475.

L. Blitz and J. P. Williams. Molecular Clouds. In C. J. Lada and N. D. Kylafis, editors, *NATO Advanced Science Institutes (ASI) Series C*, volume 540 of *NATO Advanced Science Institutes (ASI) Series C*, page 3, 1999.

W. B. Bonnor. Boyle's Law and gravitational instability. *Monthly Notices of the Royal Astronomical Society*, 116:351, 1956. doi: 10.1093/mnras/116.3.351.

G. Busquet, Q. Zhang, A. Palau, H. B. Liu, Á. Sánchez-Monge, R. Estalella, P. T. P. Ho, I. de Gregorio-Monsalvo, T. Pillai, F. Wyrowski, and et al. Unveiling a Network of Parallel Filaments in the Infrared Dark Cloud G14.225-0.506. *The Astrophysical Journal Letters*, 764:L26, Feb. 2013. doi: 10.1088/2041-8205/764/2/L26.

P. Caselli, C. M. Walmsley, R. Terzieva, and E. Herbst. The Ionization Fraction in Dense Cloud Cores. *The Astrophysical Journal*, 499:234–249, May 1998. doi: 10.1086/305624.

S. Chandrasekhar and E. Fermi. Problems of Gravitational Stability in the Presence of a Magnetic Field. *The Astrophysical Journal*, 118:116, July 1953. doi: 10.1086/145732.

N. L. Chapman, P. F. Goldsmith, J. L. Pineda, D. P. Clemens, D. Li, and M. Krčo. The Magnetic Field in Taurus Probed by Infrared Polarization. *The Astrophysical Journal*, 741:21, Nov. 2011. doi: 10.1088/0004-637X/741/1/21.

C.-Y. Chen and E. C. Ostriker. Anisotropic Formation of Magnetized Cores in Turbulent Clouds. *The Astrophysical Journal*, 810:126, Sept. 2015. doi: 10.1088/0004-637X/810/2/126.

S. D. Clarke, A. P. Whitworth, and D. A. Hubber. Perturbation growth in accreting filaments. *Monthly Notices of the Royal Astronomical Society*, 458:319–324, May 2016. doi: 10.1093/mnras/stw407.

R. M. Crutcher, B. Wandelt, C. Heiles, E. Falgarone, and T. H. Troland. Magnetic Fields in Interstellar Clouds from Zeeman Observations: Inference of Total Field Strengths by Bayesian Analysis. *The Astrophysical Journal*, 725:466–479, Dec. 2010. doi: 10.1088/0004-637X/725/1/466.

R. Ebert. Über die Verdichtung von H I-Gebieten. Mit 5 Textabbildungen. *Zeitschrift fuer Astrophysik*, 37:217, 1955.

B. G. Elmegreen and J. Scalo. Interstellar Turbulence I: Observations and Processes. *Annual Review of Astronomy and Astrophysics*, 42:211–273, Sept. 2004. doi: 10.1146/annurev.astro.41.011802.094859.

D. Falceta-Gonçalves, A. Lazarian, and G. Kowal. Studies of Regular and Random Magnetic Fields in the ISM: Statistics of Polarization Vectors and the Chandrasekhar-Fermi Technique. *The Astrophysical Journal*, 679:537-551, May 2008. doi: 10.1086/587479.

C. Federrath. On the universality of interstellar filaments: theory meets simulations and observations. *Monthly Notices of the Royal Astronomical Society*, 457:375–388, Mar. 2016. doi: 10.1093/mnras/stv2880.

O. Fehér, L. V. Tóth, D. Ward-Thompson, J. Kirk, A. Kraus, V.-M. Pelkonen, S. Pintér, and S. Zahorecz. Structure and stability in TMC-1: Analysis of NH_3 molecular line and Herschel continuum data. *Astronomy & Astrophysics*, 590:A75, May 2016. doi: 10.1051/0004-6361/201424385.

M. Fernández-López, H. G. Arce, L. Looney, L. G. Mundy, S. Storm, P. J. Teuben, K. Lee, D. Segura-Cox, A. Isella, J. J. Tobin, and et al. CARMA Large Area Star Formation Survey: Observational Analysis of Filaments in the Serpens South Molecular Cloud. *The Astrophysical Journal Letters*, 790:L19, Aug. 2014. doi: 10.1088/2041-8205/790/2/L19.

J. D. Fiege and R. E. Pudritz. Helical fields and filamentary molecular clouds - I. *Monthly Notices of the Royal Astronomical Society*, 311:85–104, Jan. 2000. doi: 10.1046/j.1365-8711.2000.03066.x.

F. O. Franco, G. A. P. & Alves. Tracing the Magnetic Field Morphology of the Lupus I Molecular Cloud. *The Astrophysical Journal*, 807:5, July 2015. doi: 10.1088/0004-637X/807/1/5.

G. F. Gahm, K. Lehtinen, P. Carlqvist, J. Harju, M. Juvela, and K. Mattila. The threaded molecular clumps of Chamaeleon III. *Astronomy & Astrophysics*, 389:577–588, July 2002. doi: 10.1051/0004-6361:20020452.

J. M. Girart, R. Rao, and D. P. Marrone. Magnetic Fields in the Formation of Sun-Like Stars. *Science*, 313:812–814, Aug. 2006. doi: 10.1126/science.1129093.

J. R. Goicoechea, J. Pety, M. Gerin, P. Hily-Blant, and J. Le Bourlot. The ionization fraction gradient across the Horsehead edge: an archetype for molecular clouds. *Astronomy & Astrophysics*, 498:771–783, May 2009. doi: 10.1051/0004-6361/200811496.

P. Goldreich and S. Sridhar. Toward a theory of interstellar turbulence. 2: Strong alfvenic turbulence. *The Astrophysical Journal*, 438:763–775, Jan. 1995. doi: 10.1086/175121.

P. F. Goldsmith. Molecular Depletion and Thermal Balance in Dark Cloud Cores. *The Astrophysical Journal*, 557:736–746, Aug. 2001. doi: 10.1086/322255.

P. F. Goldsmith, M. Heyer, G. Narayanan, R. Snell, D. Li, and C. Brunt. Large-Scale Structure of the Molecular Gas in Taurus Revealed by High Linear Dynamic Range Spectral Line Mapping. *The Astrophysical Journal*, 680:428–445, June 2008. doi: 10.1086/587166.

G. C. Gómez and E. Vázquez-Semadeni. Filaments in Simulations of Molecular Cloud Formation. *The Astrophysical Journal*, 791:124, Aug. 2014. doi: 10.1088/0004-637X/791/2/124.

A. A. Goodman, J. A. Barranco, D. J. Wilner, and M. H. Heyer. Coherence in Dense Cores. II. The Transition to Coherence. *The Astrophysical Journal*, 504:223, Sept. 1998. doi: 10.1086/306045.

A. Hacar and M. Tafalla. Dense core formation by fragmentation of velocity-coherent filaments in L1517. *Astronomy & Astrophysics*, 533:A34, Sept. 2011. doi: 10.1051/0004-6361/201117039.

A. Hacar, M. Tafalla, J. Kauffmann, and A. Kovács. Cores, filaments, and bundles: hierarchical core formation in the L1495/B213 Taurus region. *Astronomy and Astrophysics*, 554:A55, June 2013. doi: 10.1051/0004-6361/201220090.

A. Hacar, J. Alves, A. Burkert, and P. Goldsmith. Opacity broadening and interpretation of suprathermal CO linewidths: Macroscopic turbulence and tangled molecular clouds. *Astronomy & Astrophysics*, 591:A104, June 2016a. doi: 10.1051/0004-6361/201527319.

A. Hacar, J. Kainulainen, M. Tafalla, H. Beuther, and J. Alves. The Musca cloud: A 6 pc-long velocity-coherent, sonic filament. *Astronomy & Astrophysics*, 587:A97, Mar. 2016b. doi: 10.1051/0004-6361/201526015.

J. S. Hall. Observations of the Polarized Light from Stars. *Science*, 109:166–167, Feb. 1949. doi: 10.1126/science.109.2825.166.

P. Hennebelle. On the origin of non-self-gravitating filaments in the ISM. *Astronomy & Astrophysics*, 556:A153, Aug. 2013. doi: 10.1051/0004-6361/201321292.

M. Heyer, H. Gong, E. Ostriker, and C. Brunt. Magnetically Aligned Velocity Anisotropy in the Taurus Molecular Cloud. *The Astrophysical Journal*, 680:420-427, June 2008. doi: 10.1086/587510.

M. Heyer, P. F. Goldsmith, U. A. Yıldız, R. L. Snell, E. Falgarone, and J. L. Pineda. Striations in the Taurus molecular cloud: Kelvin-Helmholtz instability or MHD waves? *Monthly Notices of the Royal Astronomical Society*, 461:3918–3926, Oct. 2016. doi: 10.1093/mnras/stw1567.

R. H. Hildebrand, L. Kirby, J. L. Dotson, M. Houde, and J. E. Vaillancourt. Dispersion of Magnetic Fields in Molecular Clouds. I. *The Astrophysical Journal*, 696:567–573, May 2009. doi: 10.1088/0004-637X/696/1/567.

W. A. Hiltner. On the Presence of Polarization in the Continuous Radiation of Stars. II. *The Astrophysical Journal*, 109:471, May 1949. doi: 10.1086/145151.

M. Houde, C. L. H. Hull, R. L. Plambeck, J. E. Vaillancourt, and R. H. Hildebrand. Dispersion of Magnetic Fields in Molecular Clouds. IV. Analysis of Interferometry Data. *The Astrophysical Journal*, 820:38, Mar. 2016. doi: 10.3847/0004-637X/820/1/38.

S.-I. Inutsuka and S. M. Miyama. Self-similar solutions and the stability of collapsing isothermal filaments. *The Astrophysical Journal*, 388:392–399, Apr. 1992. doi: 10.1086/171162.

M. Juvela, I. Ristorcelli, L. Pagani, Y. Doi, V.-M. Pelkonen, D. J. Marshall, J.-P. Bernard, E. Falgarone, J. Malinen, G. Marton, and et al. Galactic cold cores. III. General cloud properties. *Astronomy & Astrophysics*, 541:A12, May 2012. doi: 10.1051/0004-6361/201118640.

J. Kainulainen, A. Hacar, J. Alves, H. Beuther, H. Bouy, and M. Tafalla. Gravitational fragmentation caught in the act: the filamentary Musca molecular cloud. *Astronomy & Astrophysics*, 586:A27, Feb. 2016a. doi: 10.1051/0004-6361/201526017.

J. Kainulainen, A. M. Stutz, T. Stanke, J. Abreu-Vicente, H. Beuther, T. Henning, K. G. Johnston, and T. Megeath. Resolving the fragmentation of high line-mass filaments with ALMA: the integral shaped filament in Orion A. *ArXiv e-prints*, Mar. 2016b.

T. Kawachi and T. Hanawa. Gravitational Collapse of Filamentary Clouds. *Publications of the Astronomical Society of Japan*, 50:577–586, Dec. 1998. doi: 10.1093/pasj/50.6.577.

R. C. Kennicutt and N. J. Evans. Star Formation in the Milky Way and Nearby Galaxies. *Annual Review of Astronomy and Astrophysics*, 50:531–608, Sept. 2012. doi: 10.1146/annurev-astro-081811-125610.

V. Könyves, P. André, A. Men'shchikov, P. Palmeirim, D. Arzoumanian, N. Schneider, A. Roy, P. Didelon, A. Maury, Y. Shimajiri, and et al. A census of dense cores in the Aquila cloud complex: SPIRE/PACS observations from the Herschel Gould Belt survey. *Astronomy & Astrophysics*, 584: A91, Dec. 2015. doi: 10.1051/0004-6361/201525861.

M. W. Kunz and T. C. Mouschovias. The initial core mass function due to ambipolar diffusion in molecular clouds. *Monthly Notices of the Royal Astronomical Society*, 399:L94–L98, Oct. 2009. doi: 10.1111/j.1745-3933.2009.00731.x.

K. I. Lee, M. Fernández-López, S. Storm, L. W. Looney, L. G. Mundy, D. Segura-Cox, P. Teuben, E. Rosolowsky, H. G. Arce, E. C. Ostriker, and et al. CARMA Large Area Star Formation Survey: Structure and Kinematics of Dense Gas in Serpens Main. *The Astrophysical Journal*, 797:76, Dec. 2014. doi: 10.1088/0004-637X/797/2/76.

D. Li and P. F. Goldsmith. Is the Taurus B213 Region a True Filament?: Observations of Multiple Cyanoacetylene Transitions. *The Astrophysical Journal*, 756:12, Sept. 2012. doi: 10.1088/0004-637X/756/1/12.

H.-B. Li, R. Blundell, A. Hedden, J. Kawamura, S. Paine, and E. Tong. Evidence for dynamically important magnetic fields in molecular clouds. *Monthly Notices of the Royal Astronomical Society*, 411:2067–2075, Mar. 2011. doi: 10.1111/j.1365-2966.2010.17839.x.

H. S. Liszt, R. W. Wilson, A. A. Penzias, K. B. Jefferts, P. G. Wannier, and P. M. Solomon. CO and CS in the Orion Nebula. *The Astrophysical Journal*, 190:557–564, June 1974. doi: 10.1086/152910.

J. Malinen, L. Montier, J. Montillaud, M. Juvela, I. Ristorcelli, S. E. Clark, O. Berné, J.-P. Bernard, V.-M. Pelkonen, and D. C. Collins. Matching dust emission structures and magnetic field in high-latitude cloud L1642: comparing Herschel and Planck maps. *Monthly Notices of the Royal Astronomical Society*, 460:1934–1945, Aug. 2016. doi: 10.1093/mnras/stw1061.

A. Men'shchikov, P. André, P. Didelon, V. Könyves, N. Schneider, F. Motte, S. Bontemps, D. Arzoumanian, M. Attard, A. Abergel, and et al. Filamentary structures and compact objects in the Aquila and Polaris clouds observed by Herschel. *Astronomy and Astrophysics*, 518:L103, July 2010. doi: 10.1051/0004-6361/201014668.

M.-A. Miville-Deschênes, P. G. Martin, A. Abergel, J.-P. Bernard, F. Boulanger, G. Lagache, L. D. Anderson, P. André, H. Arab, J.-P. Baluteau, and et al. Herschel-SPIRE observations of the Polaris flare: Structure of the diffuse interstellar medium at the sub-parsec scale. *Astronomy & Astrophysics*, 518:L104, July 2010. doi: 10.1051/0004-6361/201014678.

T. C. Mouschovias. Nonhomologous contraction and equilibria of self-gravitating, magnetic interstellar clouds embedded in an intercloud medium: Star formation. II - Results. *The Astrophysical Journal*, 207:141–158, July 1976. doi: 10.1086/154478.

T. C. Mouschovias and G. E. Ciolek. Magnetic Fields and Star Formation: A Theory Reaching Adulthood. In C. J. Lada and N. D. Kylafis, editors, *NATO Advanced Science Institutes (ASI) Series C*, volume 540 of *NATO Advanced Science Institutes (ASI) Series C*, page 305, 1999.

T. C. Mouschovias and E. V. Paleologou. The angular momentum problem and magnetic braking - an exact time-dependent solution. *The Astrophysical Journal*, 230:204–222, May 1979. doi: 10.1086/157077.

P. C. Myers. Physical Conditions in Nearby Molecular Clouds. In C. J. Lada and N. D. Kylafis, editors, *NATO Advanced Science Institutes (ASI) Series C*, volume 540 of *NATO Advanced Science Institutes (ASI) Series C*, page 67, 1999.

M. Nagasawa. Gravitational Instability of the Isothermal Gas Cylinder with an Axial magnetic Field. *Progress of Theoretical Physics*, 77:635–652, Mar. 1987. doi: 10.1143/PTP.77.635.

F. Nakamura and Z.-Y. Li. Magnetically Regulated Star Formation in Three Dimensions: The Case of the Taurus Molecular Cloud Complex. *The Astrophysical Journal*, 687:354-375, Nov. 2008. doi: 10.1086/591641.

E. Ntormousi, P. Hennebelle, P. André, and J. Masson. The effect of ambipolar diffusion on low-density molecular ISM filaments. *Astronomy & Astrophysics*, 589:A24, May 2016. doi: 10.1051/0004-6361/201527400.

J. Ostriker. The Equilibrium of Polytropic and Isothermal Cylinders. *The Astrophysical Journal*, 140:1056, Oct. 1964. doi: 10.1086/148005.

E. V. Paleologou and T. C. Mouschovias. The magnetic flux problem and ambipolar diffusion during star formation - One-dimensional collapse. I - Formulation of the problem and method of solution. *The Astrophysical Journal*, 275:838–857, Dec. 1983. doi: 10.1086/161578.

P. Palmeirim, P. André, J. Kirk, D. Ward-Thompson, D. Arzoumanian, V. Könyves, P. Didelon, N. Schneider, M. Benedettini, S. Bontemps, and et al. Herschel view of the Taurus B211/3 filament and striations: evidence of filamentary growth? *Astronomy and Astrophysics*, 550:A38, Feb. 2013. doi: 10.1051/0004-6361/201220500.

G. V. Panopoulou, K. Tassis, P. F. Goldsmith, and M. H. Heyer. ^{13}CO filaments in the Taurus molecular cloud. *Monthly Notices of the Royal Astronomical Society*, 444:2507–2524, Nov. 2014. doi: 10.1093/mnras/stu1601.

E. N. Parker. The Dynamical State of the Interstellar Gas and Field. *The Astrophysical Journal*, 145:811, Sept. 1966. doi: 10.1086/148828.

G. L. Pilbratt, J. R. Riedinger, T. Passvogel, G. Crone, D. Doyle, U. Gageur, A. M. Heras, C. Jewell, L. Metcalfe, S. Ott, and M. Schmidt. Herschel Space Observatory. An ESA facility for far-infrared and submillimetre astronomy. *Astronomy and Astrophysics*, 518:L1, July 2010. doi: 10.1051/0004-6361/201014759.

Planck Collaboration, P. A. R. Ade, N. Aghanim, D. Alina, M. I. R. Alves, C. Armitage-Caplan, M. Arnaud, D. Arzoumanian, M. Ashdown, F. Atrio-Barandela, and et al. Planck intermediate results. XIX. An overview of the polarized thermal emission from Galactic dust. *Astronomy & Astrophysics*, 576:A104, Apr. 2015. doi: 10.1051/0004-6361/201424082.

Planck Collaboration, R. Adam, P. A. R. Ade, N. Aghanim, M. I. R. Alves, M. Arnaud, D. Arzoumanian, M. Ashdown, J. Aumont, C. Baccigalupi, and et al. Planck intermediate results. XXXII. The relative orientation between the magnetic field and structures traced by interstellar dust. *Astronomy & Astrophysics*, 586:A135, Feb. 2016a. doi: 10.1051/0004-6361/201425044.

Planck Collaboration, P. A. R. Ade, N. Aghanim, M. I. R. Alves, M. Arnaud, D. Arzoumanian, M. Ashdown, J. Aumont, and et al. Planck intermediate results. XXXV. Probing the role of the magnetic field in the formation of structure in molecular clouds. *Astronomy & Astrophysics*, 586: A138, Feb. 2016b. doi: 10.1051/0004-6361/201525896.

Planck Collaboration, N. Aghanim, M. I. R. Alves, D. Arzoumanian, J. Aumont, C. Baccigalupi, and et al. Planck intermediate results. XLIV. Structure of the Galactic magnetic field from dust polarization maps of the southern Galactic cap. *Astronomy & Astrophysics*, 596:A105, Dec. 2016c. doi: 10.1051/0004-6361/201628636.

K. Qiu, Q. Zhang, K. M. Menten, H. B. Liu, Y.-W. Tang, and J. M. Girart. Submillimeter Array Observations of Magnetic Fields in G240.31+0.07: An Hourglass in a Massive Cluster-forming Core. *The Astrophysical Journal Letters*, 794:L18, Oct. 2014. doi: 10.1088/2041-8205/794/1/L18.

S. Recchi, A. Hacar, and A. Palestini. Nonisothermal filaments in equilibrium. *Astronomy & Astrophysics*, 558:A27, Oct. 2013. doi: 10.1051/0004-6361/201321565.

A. Roy, P. André, D. Arzoumanian, N. Peretto, P. Palmeirim, V. Könyves, N. Schneider, M. Benedettini, J. Di Francesco, D. Elia, T. Hill, and et al. Possible link between the power spectrum of interstellar filaments and the origin of the prestellar core mass function. *Astronomy & Astrophysics*, 584:A111, Dec. 2015. doi: 10.1051/0004-6361/201526431.

R. J. Smith, S. C. O. Glover, and R. S. Klessen. On the nature of star-forming filaments - I. Filament morphologies. *Monthly Notices of the Royal Astronomical Society*, 445:2900–2917, Dec. 2014. doi: 10.1093/mnras/stu1915.

T. P. Snow and B. J. McCall. Diffuse Atomic and Molecular Clouds. *Annual Review of Astronomy and Astrophysics*, 44:367–414, Sept. 2006. doi: 10.1146/annurev.astro.43.072103.150624.

J. D. Soler, P. Hennebelle, P. G. Martin, M.-A. Miville-Deschênes, C. B. Netterfield, and L. M. Fissel. An Imprint of Molecular Cloud Magnetization in the Morphology of the Dust Polarized Emission. *The Astrophysical Journal*, 774:128, Sept. 2013. doi: 10.1088/0004-637X/774/2/128.

J. D. Soler, F. Alves, F. Boulanger, A. Bracco, E. Falgarone, G. A. P. Franco, V. Guillet, P. Hennebelle, F. Levrier, P. G. Martin, and M.-A. Miville-Deschênes. Magnetic field morphology in nearby molecular clouds as revealed by starlight and submillimetre polarization. *Astronomy & Astrophysics*, 596: A93, Dec. 2016. doi: 10.1051/0004-6361/201628996.

J. S. Stodólkiewicz. On the Gravitational Instability of Some Magneto-Hydrodynamical Systems of Astrophysical Interest. Part III. *Acta Astron.*, 13:30–54, 1963.

K. Tassis, C. D. Dowell, R. H. Hildebrand, L. Kirby, and J. E. Vaillancourt. Statistical Assessment of Shapes and Magnetic Field Orientations in Molecular Clouds through Polarization Observations. *Monthly Notices of the Royal Astronomical Society*, 399:1681–1693, Nov. 2009. doi: 10.1111/j. 1365-2966.2009.15420.x.

K. Tomisaka. Magnetohydrostatic Equilibrium Structure and Mass of Filamentary Isothermal Cloud Threaded by Lateral Magnetic Field. *The Astrophysical Journal*, 785:24, Apr. 2014. doi: 10.1088/ 0004-637X/785/1/24.

A. Tritsis and K. Tassis. Striations in molecular clouds: streamers or MHD waves? *Monthly Notices of the Royal Astronomical Society*, 462:3602–3615, Nov. 2016. doi: 10.1093/mnras/stw1881.

S. Van Loo, E. Keto, and Q. Zhang. Core and Filament Formation in Magnetized, Self-gravitating Isothermal Layers. *The Astrophysical Journal*, 789:37, July 2014. doi: 10.1088/0004-637X/789/1/37.

D. Whittet. *Dust in the Galactic Environment, 2nd Edition*. Series in Astronomy and Astrophysics. Taylor & Francis, 2002. ISBN 9780750306249.